QUANTITATIVE ASSESSMENT OF MAGNETIC PROPERTIES WITHIN WHITE MATTER FIBERS USING MRI

A Dissertation

Presented to the Faculty of the Graduate School

of Cornell University

In Partial Fulfillment of the Requirements for the Degree of

Doctor of Philosophy

by

Cynthia Wisnieff

AUGUST 2014

QUANTITATIVE ASSESSMENT OF MAGNETIC PROPERTIES WITHIN WHITE MATTER FIBERS USING MRI

Cynthia Wisnieff, Ph. D.

Cornell University 2014

Quantitative magnetic resonance imaging techniques such as quantitative susceptibility mapping (QSM) have great potential to provide tissue specific and longitudinally applicable biomarkers of disease. Such markers can potentially aid in not only the study of disease progression, but may also one day help inform the treatment of disease. Quantitative magnetic susceptibility mapping (QSM) is a non-trivial and powerful technique that directly measures the magnetization of tissue. The magnetization of tissue in the body is directly related to its composition and structure. The challenge in this work is that both the content and organization of tissue result in orientation dependent relaxation and magnetization, the complexity of which provides an opportunity to assess tissue microstructure and content from magnetic resonance field measurements. In this work, we will evaluate the reconstruction of magnetic susceptibility and relaxation tensors from MR field measurements and assess the contribution of major tissue components, such as iron and myelin, to measured tensor properties. This builds the theoretical and experimental ground work in translating measurements of tissue magnetization for applications in vivo.

BIOGRAPHICAL SKETCH

Through her undergraduate education Cynthia Wisnieff has pursued the study of engineering with particular interest in understanding the development of technologies with the purpose of impacting the lives of others through health care. Cynthia completed her undergraduate education at Tufts University with a double major in electrical and biomedical engineering in 2009. The pursuit of a doctoral degree at Cornell has been a great opportunity to continue to learn and contribute to the study of medical imaging combining both skills in engineering and the science of biophysical mechanisms of interest in neurodegenerative disease. Cynthia is looking forward to continuing to positively impact the lives of others through medicine as she continues her education in medical school.

ACKNOWLEDGEMENTS

At Cornell I have had the extraordinary opportunity to work with talented scientists and physicians. I am truly grateful for the immense privilege I have enjoyed in studying magnetic resonance imaging in Dr. Wang's lab. In this work I have been able to continue to learn about engineering and find my passion for medicine through my work. I am thankful for all of the guidance and advice I have had from my advisors and collaborators.

The guidance and steadfast support from Dr. Wang through my work has been indispensable in completing this thesis for which I am truly grateful. I am grateful for Dr. Doerschuk's cheerful encouragement and advice throughout my time at Cornell. Dr. Gauthier's expertise and guidance has helped me to bridge my research in both engineering and healthcare technologies with medicine, which will continue to guide me for years to come.

Pascal Spincemaille and Thanh Nguyen have been ever present throughout my work at Cornell answering my many questions and discussing innumerable ideas some of which are in this thesis, for this I am truly grateful. Similarly Tian Liu and Dong Zhou have been indispensable resources in both MR physics and abstract mathematics that have helped me learn so much over my time in the lab. I have been fortunate to work with so many talented graduate students including Mitch Cooper, Bo Xu, Keigo Kawaji, Alexey Dimov, Sarah Eskries-Winkler, Kofi Deh and Jingwei Zheng.

Thank you to my family and friends for your constant support and

encouragement without which this thesis would not exist.

This research has been supported in part by: NIH grants R01EB013443, R01NS072370, R43NS076092, S10RR025145 and T35EB006732. National Multiple Sclerosis Society (RG4866-A-2).

TABLE OF CONTENTS

LIST OF FIGURES

LIST OF TABLES

LIST OF ABBREVIATIONS

FA	Fractional anisotropy
ISMRM	International Society of Magnetic Resonance in Medicine
MRI	Magnetic resonance imaging
MSA	Magnetic susceptibility anisotropy
MS	Multiple sclerosis
NAWM	Normal appearing white matter
QSM	Quantitative susceptibility mapping
RF	Radio frequency
STI	Susceptibility tensor imaging
TE	Echo time
TR	Repetition time
WM	White matter

LIST OF SYMBOLS

B_0	Applied field
D	Scalar dipole kernel in k-space
δ	Field
γ	Gyromagnetic ratio
M	Magnetization
χ	Magnetic susceptibility
$\bar{\lambda}$	Mean tensor susceptibility
λ_i	Eigenvalue
V_i	Eigenvector
ω_0	Larmor frequency

CHAPTER 1

1 CONTRIBUTIONS AND OBJECTIVES

The focus of this work is on the assessment of the magnetic properties of the central nervous system; specifically the magnetic susceptibility anisotropy and relaxation properties of white matter. In this work the reconstruction of magnetic susceptibility tensor properties of white matter are explored building from a theoretical assessment of the susceptibility tensor problem to the assessment of acquired in vivo data in measuring tensor properties of white matter. The structure, anisotropy and confidence of tensor reconstructions were assessed with experimental phantoms containing known microstructural properties and subsequently examined in vivo. The contributions of major magnetic components of white matter to the measured magnetic susceptibility were assessed in autopsied multiple sclerosis lesions where the presence of iron is a potential biomarker of the inflammatory process in the pathogenesis of multiple sclerosis lesions. With this work we gain insight into magnetic resonance (MR) properties of tissue related to tissue microstructure and molecular order and further assess MR properties directly related to tissue content.

CHAPTER 2

2 INTRODUCTION AND BACKGROUND

The fundamental principles of the magnetic resonance of protons are necessary to discuss the generation, measurement and analysis of the signal produced in magnetic resonance imaging (MRI) of tissue. These principles will link the content and structure of tissue to MRI signal generation.

2.1 Principles of MR Physics

Magnetic resonance imaging is uses the prerecession of nuclei within a static magnetic field as a radio frequency (RF) sensor to probe the local magnetic properties of tissue. A hydrogen nucleus possesses a magnetic moment,$\vec{\mu}$, that will process about the applied field, the total magnetic moment observed constitutes the observed magnetization, $\overrightarrow{\mathbf{M}}$, of the tissue. Resonance occurs at the Larmor frequency of the nucleus under investigation for a spin1/2 nucleus like hydrogen this is γ=42.58MHz/T (1), the resonance frequency is thus $\omega_0 = \gamma B_0$, where the applied field is, $\vec{B}_0$. Under an applied field the asymmetry in the distribution of parallel and antiparallel spins imparts a total net magnetization that provides that difference in energy necessary to generate an RF signal with an applied RF pulse.

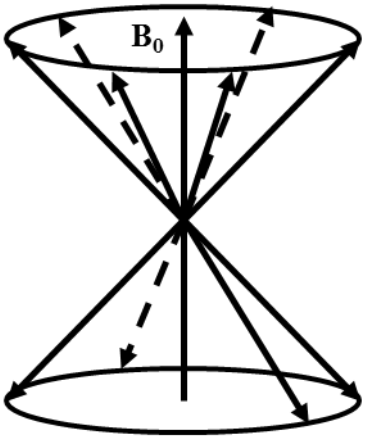

Figure 2.1 Distribution of nuclear magnetic moments observed along the applied static field

The manipulation of the excitation pulse and subsequent relaxation of this signal is largely due to the local magnetic environment. The local magnetic field is a result of the local magnetization of tissue within the body, which also provides the basis of contrast in magnetic resonance imaging and the basis of quantitative magnetic susceptibility mapping (QSM).

2.2 Principles of Magnetic Resonance Imaging

Following excitation of the tissue the next phase of an MRI experiment is the measurement of the time dependent behavior of the magnetization of the tissue, which is quantitatively described by the Bloch equation(1):

$$\frac{d\vec{\mathbf{M}}}{dt} = \gamma\vec{\mathbf{M}} \times \vec{\mathbf{B}} - \frac{M_x\vec{x}+M_y\vec{y}}{T_2} - \frac{(M_z-M_z^0)\vec{z}}{T_1}, \qquad [2.1]$$

Where T_1 and T_2 are time constants for the decay of the magnetization, M_z^0 is the equilibrium magnetization along the z axis of the system and M_x, M_y and M_z are the components of $\vec{\mathbf{M}}$ along the x, y and z axes of the system respectively. Of particular

interest are the properties of the free induction decay of hydrogen nuclei following an RF excitation, which are derived from the Bloch equation(2).

$$S(v, \mathrm{TE}) = e^{-\mathrm{TE}\,R2} \int d^3\mathbf{r}\rho(\mathbf{r})e^{-i\omega_0\delta_b(\mathbf{r})\mathrm{TE}}, \quad [2.2]$$

Where, $S(v, \mathrm{TE})$is the measured signal at time TE over the voxel v, $\rho(\mathbf{r})$is the proton density over spatial position vector **r** and $\delta_b(\mathbf{r})$ is the local field relative to B_0 . The local field is dependent on the magnetization of the tissue(3):

$$\delta_b(\mathbf{r}) = \frac{3\cos^2-1}{|\mathrm{r}|^3} * \chi(\mathbf{r})\widehat{\boldsymbol{b}}. \quad \textbf{[2.3]}$$

Where $\chi(\mathbf{r})$ is the distribution of magnetic susceptibility over the subject and $\widehat{\boldsymbol{b}}$ is the normalized field vector, $\widehat{\boldsymbol{b}} = \boldsymbol{B}_0/|B_0|$.

2.3 White Matter Tissue Properties

White matter is an essential component of the central nervous system that connects distant regions of the brain and body(4). Functional white matter is characterized as a highly organized structure from a molecular to a macroscopic scale, mm.

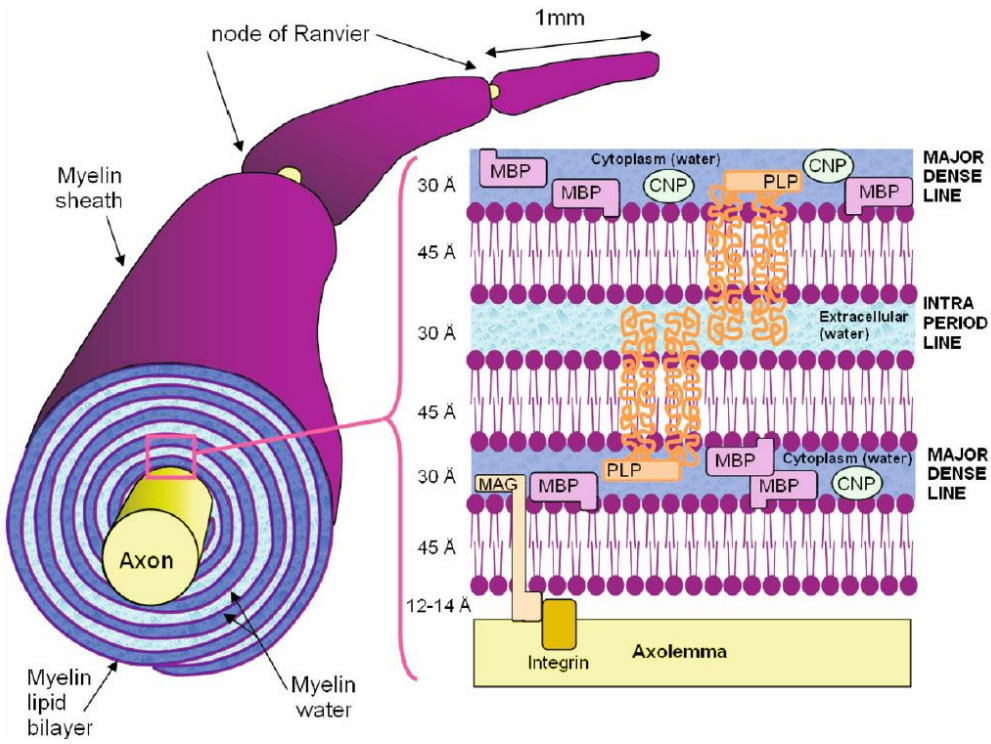

Figure 2.2: The composition and organization of the axon and molecular organization of the myelin sheath(5).

The regularly ordered myelin bilayer results in anisotropic magnetic susceptibility properties that have been of recent interest in the assessment of this tissue property with MRI(6). Destruction of this regularly ordered structure, as in the case of neuro-degenerative diseases results in progressive and permanent functional an cognitive deficits(4). MRI has the potential to quantitatively assess these properties of the tissue through analysis of the field that if formed from voxels containing these structures.

2.4 Properties of Tensor Fields

Orientation dependent properties of tensors represent high dimensional data that requires careful consideration in order to interpret properties of the tensor related to

the material properties of interest. In the study of white matter properties the orientation, mean and anisotropy of the voxel is of interest in measuring the fiber architecture and composition. Unlike scalar or vector maps interpretation of tensor fields is non-intuitive and requires defining the properties of interest of the tensor.

In the study of magnetic susceptibility tensor imaging (STI) and relaxation tensor imaging from R2* the orientation of the tensor is derived from the eigenvectors of the tensor from singular value decomposition. This reveals the eigenvalues of the tensor which are used in the derivation of tensor anisotropy and calculation of the mean tensor. The anisotropy of the tensor can have several definition depending on the specific aspect of the tensor that is of interest; such as the fractional anisotropy,

$$FA = \sqrt{\frac{3}{2}}\sqrt{\frac{\sum(\bar{\lambda}-\lambda_i)^2}{\sum(\lambda_i^2)}}, \qquad [1.1]$$

where *i*=1,2,3, (7), or the linear anisotropy, $LA = (\lambda_1 - \lambda_3)/\bar{\lambda}$. The mean tensor is defined as the normalized sum of the trace of the tensor, $\bar{\lambda} = \frac{\lambda_1+\lambda_2+\lambda_3}{3}$which is one tensor invariant; does not change with orientation of the tensor(7).

CHAPTER 3

3 MAGNETIC SUSCEPTIBILITY ANISOTROPY: CYLINDRICAL SYMMETRY FROM MACROSCOPICALLY ORDERED ANISOTROPIC MOLECULES AND ACCURACY OF MRI MEASUREMENTS USING FEW ORIENTATIONS

White matter is an essential component of the central nervous system and is of major concern in neurodegenerative diseases such as multiple sclerosis (MS). Recent MRI studies have explored the unique anisotropic magnetic properties of white matter using susceptibility tensor imaging. However, these measurements are inhibited in practice by the large number of different head orientations needed to accurately reconstruct the susceptibility tensor. Adding reasonable constraints reduces the number of model parameters and can help condition the tensor reconstruction from a small number of orientations. The macroscopic magnetic susceptibility is decomposed as a sum of molecular magnetic polarizabilities, demonstrating that macroscopic order in molecular arrangement is essential to the existence of and symmetry in susceptibility anisotropy and cylindrical symmetry is a natural outcome of an ordered molecular arrangement. Noise propagation in the susceptibility tensor reconstruction is analyzed through its condition number, showing that the tensor reconstruction is highly susceptible to the distribution of acquired subject orientations and to the tensor symmetry properties, with a substantial over- or under-estimation of susceptibility anisotropy in fiber directions not favorably oriented with respect to the acquired orientations. It was found that a careful acquisition of three non-coplanar orientations and the use of cylindrical symmetry guided by diffusion tensor imaging allowed

reasonable estimation of magnetic susceptibility anisotropy in certain major white matter tracts in the human brain.

3.1 Motivation and Background

The white matter of the brain is organized in long fibers that trace throughout the central and peripheral nervous system (8). Myelin sheaths of axons, which are composed of concentric phospholipid bilayers, are intrinsically tied to this fiber structure (8,9). The phase of the MRI signal (10,11) and T2* relaxation (12,13) of the white matter have been found to depend on the orientation of the fibers with respect to the main magnetic field. These effects can be attributed to the existence of an orientation-dependent magnetization or magnetic susceptibility anisotropy (MSA) of the macroscopic white matter tract. It is well known that macroscopically well-organized materials with anisotropic electron configurations, such as polymers (14), minerals (15) and liquid crystals (16), can give rise to anisotropic magnetic susceptibility properties. Like these materials, the highly structured and organized nature of the myelin sheath of the white matter leads to its anisotropic magnetic behavior (6,17-19). This intrinsic anisotropic nature of phospholipid membranes has been previously observed in NMR *in vitro* within a model system (20). Few other structures in the brain present the same level of macroscopic organization as the white matter, without which the magnetic anisotropy may not be observable in MRI.

To assess the orientation-dependent magnetization of materials like white matter, susceptibility tensor imaging (STI) can be estimated from MRI data acquired at 12 or more subject orientations (17,21), which unfortunately are not acceptable in

clinical practice. Furthermore, unlike studying the MSA of rocks using multiple acquisitions of the sample over a free range of orientations (22), the limited range of orientations with human subjects may lead to substantial noise propagation in the observed MSA. Constraining the system with reasonable prior information and assumptions can help condition the problem and reduce error propagation. Specifically, reducing the number of model parameters will reduce the number of required orientations to recover the susceptibility tensor. For example, a cylindrically symmetric susceptibility tensor (CSST) will reduce the number of parameters for the susceptibility tensor to two from three in the orthonormal tensor frame (23). Exploiting symmetry in tensors has been explored in other applications as well including characterization of diffusivities in the spinal cord (24) and the orientation of minerals in rocks (15). The parallel and perpendicular axes of the white matter fiber tract derived from diffusion tensor imaging (DTI) can be used to define this orthonormal frame on a voxel-by-voxel basis (Fig. 3.1). As a result, the original 6-parameter STI problem is reduced to a 2-parameter CSST problem (25).

The purpose of this work is to systematically explore the symmetry of susceptibility anisotropy in the white matter of the human brain and investigate the performance of MSA estimation using the CSST and three subject orientations. This work employs theoretical calculation, numerical simulations, phantoms and human *in vivo* data. The macroscopic susceptibility anisotropy is connected with molecular magnetic polarization anisotropies through their arrangement in space, demonstrating that macroscopic order of molecule arrangement is essential to the existence of and the

symmetry in susceptibility anisotropy observed in MRI. Error propagation in the CSST estimation is analyzed according to the symmetry characteristics of the tissue susceptibility tensor and the possible sets of subject orientations acquired in MRI, showing that DTI guided estimation of cylindrical MSA in major white matter tracts of the brain can be reasonable with as few as three non-coplanar orientations.

3.1.1 *Origins of magnetic susceptibility anisotropy observed in MRI from the macroscopic arrangement of molecules with Magnetic polarizability anisotropy*

In general, macroscopic tissue magnetization, **M**, can be described as its susceptibility χ times the applied magnetic field, **H**, $\mathbf{M} = \chi\mathbf{H} \cong \chi\mathbf{B_0} / \mu_0$, $\mathbf{B_0}$ is the main magnetic field of the MR scanner and μ_0 is the magnetic permeability of free space (26). χ can be a general 3x3 matrix or tensor to account for the possible orientation dependent relationship between the magnetization and the applied field (27). The magnetization is the sum of the magnetic moments of molecules in a unit volume, which is related to the applied magnetic field by the molecular polarizability

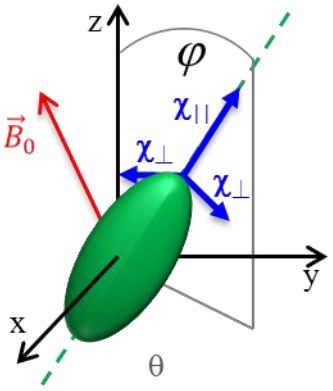

Figure 3.1 The tensor frame is defined by the axes along $\chi_{\parallel}$ and $\chi_{\perp}$. The subject frame is defined by x, y and z axes. These two frames are related by a rotation around an axis along the cross product of z and $\chi_{\parallel}$ axes with a rotation angle ϕ equal to the angle between of z and $\chi_{\parallel}$ axes. For the purpose of describing the fiber orientation defined by the $\chi_{\parallel}$ axis, we also characterize the $\chi_{\parallel}$ axis using its polar angle ϕ and azimuthal angle θ as viewed in the subject frame xyz.

tensor $\boldsymbol{\beta}_a$: $\mathbf{M} = 1/\mu_0 \sum_a \boldsymbol{\beta}_a \mathbf{B}_0$, where the summation index a is over all molecules in a unit volume. Therefore the susceptibility within a voxel is the sum of magnetic polarizabilities of all molecules,

$$\boldsymbol{\chi} = n \sum_a \boldsymbol{\beta}_a \qquad [3.1]$$

where *n* is a factor accounting for the density of molecules within a voxel. The orientation of a molecule can be represented by its rotation matrix, $\mathbf{R}_a$, and its magnetic polarizability tensor can be described in terms of its eigenvalues in a molecular specific frame where the tensor is diagonal:

$$\boldsymbol{\beta}_a = \mathbf{R}_a \boldsymbol{\beta} \mathbf{R}_a^T \qquad \boldsymbol{\beta} = \begin{bmatrix} \beta_1 & 0 & 0 \\ 0 & \beta_2 & 0 \\ 0 & 0 & \beta_3 \end{bmatrix} \qquad [3.2]$$

Biological tissues may contain both isotropic and anisotropic sources of magnetic susceptibility (20,28). One major source of susceptibility consists of paramagnetic ions due to unpaired electrons (26) including iron deposition (29) and MRI contrast agents (30). These paramagnetic ions are known to be isotropic ($\boldsymbol{\beta}_a = \beta \mathbf{I}$ = constant times identity matrix) with their magnetic moments independent of molecular orientation and have been widely examined using scalar susceptibility mapping techniques (31-35), and according to Eqs.1&2 in this section, they will not contribute to the macroscopic susceptibility anisotropy.

3.1.2 The Susceptibility Tensor of a Voxel with Molecules of Various Organizations

Another major type of susceptibility source is diamagnetism from most biological molecules, which are mostly anisotropic in spatial structure. They can contribute to the macroscopic susceptibility anisotropy observable in MRI through the summation over all molecules in a macroscopic unit volume. When anisotropic molecules are oriented uniformly over all possible angles, i.e., there is no macroscopic order in the molecular alignment, the average over many molecules in a volume with molecular density n eliminates anisotropy, rendering the macroscopic susceptibility isotropic

In this section we will apply Schur's second lemma from group theory to express the expectation value of the magnetic polarizability tensor. To begin, we define irreducible and reducible representations; in this paper we are interested in matrix representations of the rotation groups. If a representation can be written in a block diagonal form, such that its action can be defined on its individual subspaces, it is said to be reducible otherwise the representation is irreducible (36). For example a rotation about the z-axis can be expressed in 2 or 3 dimensions, the 2D representation (2x2 matrices) is irreducible, whereas the 3D representation (3x3 matrices, which are block diagonal with the 2D matrix as one block and 1 as the other block) is reducible. Schur's second lemma states: if the matrices **R** are irreducible representations of a group and if a matrix **A** commutes with **R**, $\mathbf{RA} = \mathbf{AR}$, for all **R** in the group then **A** is scalar, $\mathbf{A} = \text{constant} \cdot \mathbf{I}$ (36).

As stated in Eq. 3.1 the susceptibility of a voxel is the sum of magnetic polarizabilities within a unit volume. Considering a specific organization of molecules, we introduce the expected mean value of the magnetic polarizability tensor as:

$$\langle \boldsymbol{\beta} \rangle = \int_a \mathbf{R}_a \boldsymbol{\beta} \mathbf{R}_a^T da \qquad [3.3]$$

where $\mathbf{R}_a$ is a 3-dimenional rotation described by Eq. 3.10, and the integration is over the possible angles. The explicit matrix form of the rotation $\mathbf{R}_a$ is the representation of the 3D rotation group. In the form described by Eq. 3.10, all unconstrained 3D rotations form an irreducible representation. The mean polarizability $\langle \boldsymbol{\beta} \rangle$ commutes with all 3D rotations $\mathbf{R}_a$. By Schur's second lemma, $\langle \boldsymbol{\beta} \rangle$ is a scalar in 3D space, and its value can be determined from its trace, which is invariant under rotations. As such the resulting susceptibility tensor is:

$$\boldsymbol{\chi}_{iso} = n \begin{bmatrix} (\beta_1 + \beta_2 + \beta_3)/3 & 0 & 0 \\ 0 & (\beta_1 + \beta_2 + \beta_3)/3 & 0 \\ 0 & 0 & (\beta_1 + \beta_2 + \beta_3)/3 \end{bmatrix} \qquad [3.4]$$

where n is a factor to account for the density the molecules within the voxel. Therefore, it follows directly from Schur's lemma that freely oriented molecules will result in an isotropic susceptibility tensor($\boldsymbol{\chi} = \chi \mathbf{I}$ = constant times identity matrix). This result can also be shown numerically.

Now we consider fixing one of the components of the magnetic polarizability

along the z-axis of the voxel. This only allows the molecular axes corresponding to β_1 and β_2 to rotate about the β_3 axis freely; β_3 remains along the z axis of the voxel as in Fig 2a.The group under consideration is the 2D rotation group about the z-axis. The matrix representation $\mathbf{R}_Z(\alpha)$, for the rotation about the z axis by an angle, α, is reducible in 3 dimensions, while the block in the x-y plane is irreducible. Correspondingly, we introduce a 3D mean polarizabilty tensor as:

$$\langle \boldsymbol{\beta} \rangle = \frac{1}{2\pi} \int_{\alpha} \mathbf{R}_Z(\alpha) \boldsymbol{\beta} \mathbf{R}_Z^T(\alpha) d\alpha \qquad [3.5]$$

and we can apply Schur's lemma similarly to the 2D block. From this we can obtain one expression for a cylindrically symmetric susceptibility tensor:

$$\boldsymbol{\chi}_{CS1} = n \begin{bmatrix} (\beta_1 + \beta_2)/2 & 0 & 0 \\ 0 & (\beta_1 + \beta_2)/2 & 0 \\ 0 & 0 & \beta_3 \end{bmatrix} \qquad [3.6]$$

This is one possible configuration that could describe the anisotropy of white matter that restricts the β_3 axis of the tensor to lie along the fiber direction, but allows the other components to orient freely in transverse plane, Fig. 3.2a.

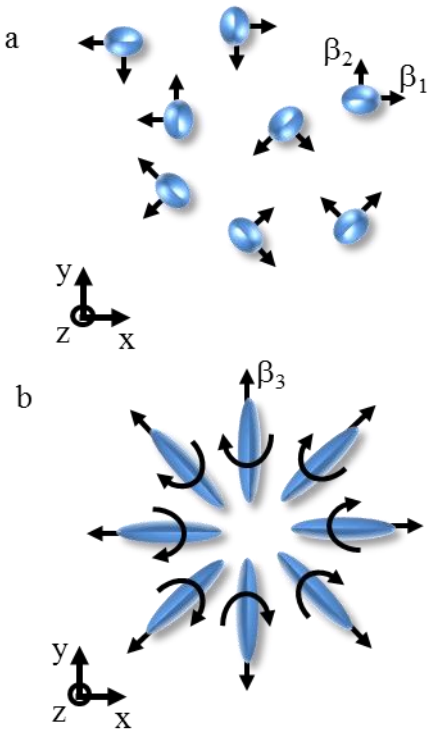

Figure 3.2: a, shows the configuration of molecules examined for the first cylindrically symmetric case. b, shows the more realistic configuration of molecules that describes the organization of lipids that exists in myelin.

This organization shows susceptibility that is cylindrically symmetric with molecules that have any arbitrary anisotropy. This configuration may not be entirely realistic for white matter as it restricts one component to lie along the fiber direction, while it is known that the phospholipids of the myelin sheath can undergo diffusion within the membrane as the molecules are not chemically bound (37,38).

We can obtain more realistic cylindrical symmetry in the organization of molecules by imposing that the β_3 axis of the tensor must lie in the x-y plane, but the

β_1 and β_2 axes are oriented evenly in the plane perpendicular to the β_3 axis. This allows the molecules to have the freedom to rotate about the β_3 axis in the transverse plane to account for their freedom of movement, Fig. 3.2b. To do this we decompose the 3-dimensional rotation matrix into its Euler angles using the zxz-convention such that (39) : $\mathbf{R}_a = \mathbf{R}_Z(\phi_a)\mathbf{R}_X(\pi/2)\mathbf{R}_Z(\psi_a)$, where $\mathbf{R}_Z$ and $\mathbf{R}_X$ are rotations about the z axis and x axis respectively at angles ϕ_a, π/2 and ψ_a. Here ϕ_a and ψ_a take all possible angles. Correspondingly, we introduce the mean polarizability tensor as:

$$\langle \boldsymbol{\beta} \rangle = \frac{1}{4\pi^2} \int_{\phi_a} \int_{\psi_a} \mathbf{R}_Z(\phi_a)\mathbf{R}_X(\pi/2)\mathbf{R}_Z(\psi_a)\boldsymbol{\beta}(\mathbf{R}_Z(\phi_a)\mathbf{R}_X(\pi/2)\mathbf{R}_Z(\psi_a))^T d\psi_a d\phi_a \quad [3.7]$$

Similar to Eq. 3.5, we can apply Schur's lemma to the two 2D rotations, $\mathbf{R}_Z(\phi_a)$ and $\mathbf{R}_Z(\psi_a)$. The resulting susceptibility tensor is:

$$\boldsymbol{\chi}_{CS2} = n\begin{bmatrix} (\beta_1+\beta_2+2\beta_3)/4 & 0 & 0 \\ 0 & (\beta_1+\beta_2+2\beta_3)/4 & 0 \\ 0 & 0 & (\beta_1+\beta_2)/2 \end{bmatrix} \quad [3.8]$$

This organization also shows cylindrical symmetry in the susceptibility tensor with arbitrary anisotropy in the molecules within the voxel. Both equations 3.6 and 3.8 produce a cylindrically symmetric tensor, similar to the white matter tensor model presented by Li et al. (17) without assuming that the lipid molecules themselves are cylindrically symmetric.

$$\boldsymbol{\chi}_{iso} = n\begin{bmatrix} (\beta_1+\beta_2+\beta_3)/3 & 0 & 0 \\ 0 & (\beta_1+\beta_2+\beta_3)/3 & 0 \\ 0 & 0 & (\beta_1+\beta_2+\beta_3)/3 \end{bmatrix} \quad [3.9]$$

For molecular magnetic anisotropy to be observable at the resolution of MRI, macroscopic order of the molecular orientation is needed. An example is the order within white matter fiber tracts, where the lipid molecules in myelin are arranged in a radial pattern perpendicular to the fiber direction (9), resulting in anisotropy in the macroscopic magnetic susceptibility (17). One possible model of myelin consists of constraining the β_3 component to lie along the fiber axis, while the other axes are uniformly distributed in the plane orthogonal to the β_3 (or fiber) axis, Fig. 3.2a. The resulting macroscopic anisotropic susceptibility, $\boldsymbol{\chi}_{CS1}$ is given by (Eq. 3.6),

$$\boldsymbol{\chi}_{CS1} = n\begin{bmatrix} (\beta_1+\beta_2)/2 & 0 & 0 \\ 0 & (\beta_1+\beta_2)/2 & 0 \\ 0 & 0 & \beta_3 \end{bmatrix} \quad [3.10]$$

Fixing one of the molecular axes to lie along the axis of the white matter fiber may not be entirely realistic as the molecules are free to diffuse in the membrane since they are not chemically bound (37,38). More realistic configurations would allow the molecule to rotate about an axis that lies perpendicular to the fiber direction. The cylindrical symmetry of myelin may be represented by constraining the β_3 component to lie in the transverse plane, while the other axes of the molecule are uniformly distributed in the plane orthogonal to the β_3 axis, Fig. 3.2b. Resulting in a macroscopic anisotropic

susceptibility, χ_{CS2} given by (Eq. 3.8)

$$\chi_{CS2} = n\begin{bmatrix} (\beta_1+\beta_2+2\beta_3)/4 & 0 & 0 \\ 0 & (\beta_1+\beta_2+2\beta_3)/4 & 0 \\ 0 & 0 & (\beta_1+\beta_2)/2 \end{bmatrix} \quad [3.11]$$

Eqs.4&5 indicate that when the molecules are ordered in space along a line or within a plane, the resulting macroscopic susceptibility tensor is always cylindrically symmetric for molecular magnetic polarizabilities with any anisotropy.

Data from a model of dysmyelination in shiverer mice brains showed near complete loss of anisotropy in magnetic susceptibility suggesting that myelin is largely responsible for the observed susceptibility anisotropy (40).

3.1.3 Estimating Cylindrical Symmetric Susceptibility Tensor (CSST) from MRI

The MRI signal phase permits determination of the magnetic field generated by a tensor source according to Maxwell's equations in k-space (6):

$$\Delta(\mathbf{k}) = \frac{\hat{\mathbf{b}}\cdot\left(\mathbf{X}\cdot\hat{\mathbf{b}}\right)}{3} - \hat{\mathbf{b}}\cdot\mathbf{k}\frac{\mathbf{k}\cdot\left(\mathbf{X}\cdot\hat{\mathbf{b}}\right)}{k^2} \quad [3.12]$$

where **X** is the second rank tensor of the magnetic susceptibility in the Fourier domain, Δ is the relative field change, also in the Fourier domain, normalized by the main field strength, $\hat{\mathbf{b}} = \mathbf{B_0}/\|\mathbf{B_0}\|$ is the orientation of the main field, and **k** is the Fourier space vector. In general susceptibility tensor imaging (STI), the inverse problem of finding

the magnetic susceptibility tensor from the MRI field measurements is solved by imaging the subject at multiple $\hat{\mathbf{b}}$ directions, which can be achieved by reorienting the subject in the magnet. Let the subject frame be the orthogonal coordinate system coincident with the natural axes defined by the subject, such as the superior-inferior (SI), anterior-posterior (AP) and left-right (LR) axes of the head of a volunteer when positioned supine and head first in the scanner. Within the subject frame, the solution for Eq.12 can be formulated as:

$$\mathbf{X}(\mathbf{k}) = \arg\min_{\mathbf{X}(\mathbf{k})} \sum_p \left| w_p(\mathbf{r}) \left[FT^{-1}(\Delta_p(\mathbf{k})) - FT^{-1}\left(\frac{\hat{\mathbf{b}}_p \cdot \left(\mathbf{X} \cdot \hat{\mathbf{b}}_p\right)}{3} - \hat{\mathbf{b}}_p \cdot \mathbf{k} \frac{\mathbf{k} \cdot \left(\mathbf{X} \cdot \hat{\mathbf{b}}_p\right)}{k^2} \right) \right] \right|^2 \qquad [3.13]$$

where p is the index of the acquired orientation and w_p is a weighting factor to minimize the propagation of noise (approximated as Gaussian) in the measured field (3). In general, the inverse problem of Eq.3.12 is poorly conditioned and upwards of 11 orientations has been reported to generate STI (17,21). The cylindrical symmetry described in Eq.3.6 or 3.8 with the cylindrical axis estimated from diffusion tensor imaging (DTI) can be used to reduce the number of unknowns in Eq.3.12, therefore improving the condition of inversion and reducing the number of orientations needed (23,25). Important questions that remain to be addressed are to examine the improvement in the condition of the problem from assuming symmetry and to investigate the accuracy in the estimated CSST that can be achieved with a limited number of orientations.

The experimental part of this work endeavors to answer the latter of these

questions. We begin by introducing the following notation for the tensor frame. Let the tensor frame for a given voxel be the orthonormal basis in which the susceptibility tensor at that voxel is strictly diagonal. For the CSST, the cylindrical symmetry can be imposed in this tensor frame by making two diagonal elements identical and the other diagonal element correspond to the myelin cylindrical axis as estimated from DTI data:

$$\boldsymbol{\chi}_T = \begin{bmatrix} \chi_\perp & 0 & 0 \\ 0 & \chi_\perp & 0 \\ 0 & 0 & \chi_\parallel \end{bmatrix} \qquad [3.14]$$

The susceptibility tensor in the subject frame, in image space, is then given by $\boldsymbol{\chi} = \mathbf{R}^{\mathbf{T}} \boldsymbol{\chi}_T \mathbf{R}$, where $\mathbf{R}$ is the rotation matrix that relates the subject frame to the tensor frame. For the CSST, the expression for the forward problem in Eq. 3.12 is updated as:

$$\Delta(\mathbf{k}) = \frac{\hat{\mathbf{b}} \cdot \left(FT(\mathbf{R}^{\mathrm{T}} \boldsymbol{\chi}_T \mathbf{R}) \cdot \hat{\mathbf{b}} \right)}{3} - \hat{\mathbf{b}} \cdot \mathbf{k} \frac{\mathbf{k} \cdot \left(FT(\mathbf{R}^{\mathrm{T}} \boldsymbol{\chi}_T \mathbf{R}) \cdot \hat{\mathbf{b}} \right)}{k^2} \qquad [3.15]$$

The principal diffusion direction derived from DTI is here assumed to coincide with the direction of the parallel component of the susceptibility tensor. The rotation matrix is defined by the Euler principal rotation vector formula according to the axis and angle of rotation between any two coordinate systems (41):

$$\mathbf{R} = \begin{bmatrix} V_x^2(1-\cos(\phi)) + \cos(\phi) & V_x V_y(1-\cos(\phi)) + V_z \sin(\phi) & V_x V_z(1-\cos(\phi)) - V_y \sin(\phi) \\ V_y V_x(1-\cos(\phi)) - V_z \sin(\phi) & V_y^2(1-\cos(\phi)) + \cos(\phi) & V_y V_z(1-\cos(\phi)) + V_x \sin(\phi) \\ V_z V_x(1-\cos(\phi)) + V_y \sin(\phi) & V_z V_y(1-\cos(\phi)) - V_x \sin(\phi) & V_z^2(1-\cos(\phi)) + \cos(\phi) \end{bmatrix} \qquad [3.16]$$

where $\hat{\mathbf{V}} = [V_x\ V_y\ V_z]$ and ϕ are the axis unit vector and angle of rotation. The angle of rotation, ϕ, is the angle between the principal axes in the tensor and subject frames; for example the angle between the **z** axis in the subject frame and the **z**' axis in the tensor frame.

3.1.4 Condition Number for Estimating the Susceptibility Tensor With and Without Constraints

In examining linear systems of the form, **Ax** = **b,** it is useful to have an indicator of the stability of the solution of a system from perturbations in the input data. Using numerical methods to find a solution for a linear system **Ax** =**b**, where **A** is Hermitian, it can be shown that under perturbations on a non-trivial **b**, $\boldsymbol{\delta}\mathbf{b}$, the error, $\boldsymbol{\delta}\mathbf{x}$, in the estimate of the solution, $\hat{\mathbf{x}} = \mathbf{x} + \boldsymbol{\delta}\mathbf{x}$, is bound by(42):

$$\frac{\|\boldsymbol{\delta}\mathbf{x}\|_2}{\|\mathbf{x}\|_2} \le \frac{\|\boldsymbol{\delta}\mathbf{b}\|_2}{\|\mathbf{b}\|_2}\left\{\frac{2\kappa(\mathbf{A})}{\cos(\omega)} + \tan(\omega)\kappa^2(\mathbf{A})\right\} + O\left(\left(\frac{\|\boldsymbol{\delta}\mathbf{b}\|_2}{\|\mathbf{b}\|_2}\right)^2\right) \qquad [3.17]$$

where κ(**A**) is the condition of a linear system **A** and $\sin(\omega) = \|\mathbf{A}\hat{\mathbf{x}} - \mathbf{b}\|_2 / \|\mathbf{b}\|_2$. In this case if the condition number is finite the error in the solution is bound by the condition number; if the condition number is infinite the error is unbounded and as such this system would be ill-posed. For a system of the form **Ax** = **b**, with **A** Hermitian, the condition number of **A** is an indicator of the error propagation that can be expected from small perturbations. The condition number with respect to the 2 norm is defined

as the ratio of the maximum to minimum eigenvalues of the system, $\kappa(\mathbf{A}) = \|\mathbf{A}\|_2 / \|\mathbf{A}^{-1}\|_2 = \lambda_{max}/\lambda_{min}$ (42). In estimating the STI and CSST, the original system matrix **A** is not Hermitian and the condition number of $\mathbf{A}^H\mathbf{A}$ is computed instead, where ^{H} indicates the Hermitian transpose. In matrix form the STI and CSST systems can be written as block diagonal matrices for which it is possible to calculate the eigenvalues similar to COSMOS, (43).

For STI, Eq. 3.12 in matrix form is written as $\Delta_p(\mathbf{k}) = \sum_{i,j=1,i\le j}^{3} D_{p,ij}(\mathbf{k}) X_{ij}(\mathbf{k})$

,where Δ_p, is the measured difference field for each orientation *p* and $D_{p,ij}$ is a block diagonal matrix whose blocks are px6 matrices for every point in k-space, whose coefficients are given by the STI system described by Liu, (6), where the p^{th} row has the form:

$$D_{p,ij}(\mathbf{k}) = \begin{cases} \frac{b_{p,i}b_{p,j}}{3} - \left(\hat{\mathbf{b}}_p \cdot \mathbf{k}\right)\frac{k_i b_{p,j}}{\mathbf{k}^2} & i = j \\ \frac{2b_{p,i}b_{p,j}}{3} - \left(\hat{\mathbf{b}}_p \cdot \mathbf{k}\right)\frac{\left(k_i b_{p,j} + k_j b_{p,i}\right)}{\mathbf{k}^2} & i \neq j \end{cases} \qquad [3.18]$$

for every point, $\mathbf{k}$, in k-space, where k_i is the i^{th} component of this vector, $\hat{\mathbf{b}}_p = \mathbf{B}_{0p} / \|\mathbf{B}_{0p}\|$ is the applied field vector for orientation *p*, $b_{p,i}$ is the i^{th} component of this vector, each combination ij takes values ij = [11, 12, 13, 22, 23, 33]. After adopting the compact notation for these coefficients, $D_{p,ij}(\mathbf{k}) = [D_{p,11}(\mathbf{k}) \quad D_{p,12}(\mathbf{k}) \quad \cdots \quad D_{p,33}(\mathbf{k})]$, the system $[D^H D]_{ij,lm}$ can be seen to be block diagonal with 6x6 blocks having coefficients:

$$[D^H D]_{ij,lm} = \sum_p D_{p,ij}(\mathbf{k}) D_{p,lm}(\mathbf{k}) \qquad [3.19]$$

where *ij* and *lm* take values: [11, 12, 13, 22, 23, 33]. The eigenvalues of the overall system are determined by the eigenvalues of these 6x6 blocks and the condition of the system is the ratio of the maximum to minimum eigenvalue. In order for this block to have full rank the number of orientations must be greater than or equal to 6.

With symmetry constraints Eq. 3.18 can be written in the form:

$\Delta_p(\mathbf{k}) = \sum_{i,j=1,i\le j}^{3} D_{p,ij}(\mathbf{k}) FT((\mathbf{R}(\mathbf{r})^T \boldsymbol{\chi}_T(\mathbf{r}) \mathbf{R}(\mathbf{r}))_{ij})$, where the constraint in image space for the CSST introduces the complication where it is difficult to decouple the susceptibility coefficients from the forward problem for the CSST without forming a convolution in k-space. For the purposes of analysis, the condition number of the case where the rotation matrix is the identity matrix is examined such that the tensor is the same in subject and tensor frame. With this assumption the convolution in k-space reduces to convolution with a delta function. For this case the CSST in matrix form is written as $\Delta_p = \mathbf{D}\mathbf{M}\mathbf{X}_T$, where **M** is a block diagonal matrix mapping function that allows us to write the parallel and perpendicular components in the tensor frame to the six components in the subject frame, whose blocks are:

$$\mathbf{R}_m = \begin{bmatrix} 1 & 0 \\ 0 & 0 \\ 0 & 0 \\ 1 & 0 \\ 0 & 0 \\ 0 & 1 \end{bmatrix} \qquad [3.20]$$

The system D**M** can be shown to be block diagonal with px2 blocks of the form:

$$[\mathbf{DM}]_{p,1} = D_{p,11}(\mathbf{k}) + D_{p,22}(\mathbf{k}) \qquad [3.21]$$

$$[\mathbf{DM}]_{p,2} = D_{p,33}(\mathbf{k}) \quad [B.5]$$

Similar to the unconstrained case the system $\mathbf{M}^{H}\mathbf{D}^{H}\mathbf{DM}$, is a block diagonal system with 2x2 blocks of the form:

$$\begin{bmatrix} \sum_{p}\left(D_{p,11}(\mathbf{k}) + D_{p,22}(\mathbf{k})\right)^2 & \sum_{p}\left(\left(D_{p,11}(\mathbf{k}) + D_{p,22}(\mathbf{k})\right)\left(D_{p,33}(\mathbf{k})\right)\right) \\ \sum_{p}\left(\left(D_{p,11}(\mathbf{k}) + D_{p,22}(\mathbf{k})\right)\left(D_{p,33}(\mathbf{k})\right)\right) & \sum_{p}\left(D_{p,33}(\mathbf{k})\right)^2 \end{bmatrix} \qquad [3.22]$$

The coefficients of these square block matrices can be easily calculated to evaluate the eigenvalues and condition of this system.

3.2 Methods

3.2.1 Estimation of the Condition Number for the 3-CSST

A detailed discussion of the condition number and how it is calculated in this work is presented in here. To investigate the condition number of the CSST we examine the case where the rotation is an identity matrix simplifying the convolution in k-space. In this case the parallel component of the cylindrically symmetric tensor lies along the z axis over the entire field of view in both the subject and tensor frames; there is no assumed distribution of tensor coefficients only the orientation of the tensor is necessary to estimate the condition of the CSST system. Coefficients for the blocks of the system were generated according to Eq.3.22 and eigenvalues were calculated

numerically using Matlab. The condition numbers of the 560 sets of 3 orientations used in the simulated phantom, Fig. 3.3, were examined. Since matrix components were explicitly constructed, to simplify eigenvalue calculations a smaller matrix size of 32x32x32 in k-space was used to reduce calculation time and memory requirements.

3.2.2 Numerical Simulation: Sensitivity of 3-CSST to Acquisition Orientations

A numerical simulation consisting of three spherically shaped regions of interest (ROIs): two contained isotropic susceptibility (regions A and B in Fig. 3.3a), while the third (region C in Fig. 3.3a) contained susceptibility anisotropy similar to that observed in human white matter *in vivo* (17). The values for $\chi_{\perp}$ and $\chi_{\parallel}$ were chosen as -0.03 and -0.01 parts per million (ppm), respectively. The simulated data consisted of 16 orientations evenly distributed over a unit sphere. A range of tensor reconstructions were investigated. First, CSST and STI reconstructions using all 16 orientations were performed. Second, a CSST reconstruction was performed for each set of 3 orientations chosen from the total set of 16 orientations (560 combinations) to investigate the variability in results from the limited number of orientations. Reconstructions are referred to as *N*-STI or *N*-CSST, with *N* indicating the number of orientations used in the reconstruction. A signal-to-noise ratio (SNR) of 100 was chosen to approximate the noise observed in human studies; initial simulations in preparation for this work with this numerical phantom showed that relatively high SNR was required for accurate estimation of the tensor components in the simulations. The field map was generated according to the forward model in Eq.3.12. It was

assumed that the principal diffusion tensor eigenvector of the phantom was known (taken to be the simulated one) as diffusion data was not simulated.

The magnetic susceptibility anisotropy (MSA) for a susceptibility tensor with cylindrical symmetry was defined as the difference between parallel and perpendicular principal components of the tensor,

$$\mathrm{MSA} = \chi_{\parallel} - \chi_{\perp} \qquad [3.23]$$

In the unconstrained 16-STI reconstruction, parallel and perpendicular components are not well defined; the second eigenvalue may or may not clearly resemble either the maximum or minimum eigenvalue, which is needed for cylindrical symmetry in general. In this work for comparison among STI and CSST reconstructions, the MSA from STI was defined as,

$$\mathrm{MSA} = \lambda_1 - (\lambda_2 + \lambda_3)/2 \qquad [3.24]$$

where the tensor eigenvalues λ_i are ordered from large to small. This difference was chosen since it is expected that the parallel component of the tensor is more paramagnetic as observed in previous studies of white matter (17,21). A histogram of the mean MSA of the fibers oriented along the x-axis (C in Fig. 3.3a) from all possible 3-CSST reconstructions was obtained to examine possible bias caused by the limited number of orientations. The orientations that were within ±50° from the x-axis of the simulation were considered to be within the range of human feasible orientations.

3.2.3 Numerical Simulation: Realistic Fiber Orientations and MSA Estimation

To investigate the error in the susceptibility tensor reconstructed from a limited number of orientations, a numerical simulation was performed using the brain anatomy of a volunteer in this study. An automatic segmentation algorithm, FAST (44), was used to segment a T2 weighted image obtained in this volunteer into white matter, grey matter and cerebrospinal fluid (CSF). Specific grey matter regions were identified by hand from this initial segmentation. The white matter (WM) was set to have a homogeneous susceptibility tensor (in the voxel specific tensor frame) that was cylindrically symmetric, $\chi_{\parallel}$ = -0.01ppm and $\chi_{\perp}$ = - 0.03 ppm. The grey matter and CSF regions were set to have isotropic magnetic susceptibility described by scalars as follows: CSF, 0 ppm; globus pallidus (GP), 0.19 ppm; putamen (PU), 0.09 ppm; thalamus (T), 0.07 ppm; red nucleus (RN), 0.07 ppm; substantia nigra (SN), 0.09 ppm; dentate nucleus (DN), 0.09 ppm; caudate nucleus (CN), 0.09 ppm; and cortex (C) 0.05 ppm, similar to values observed *in vivo* (45). The orientation of the tensor for each voxel was defined by the principal diffusion eigenvector, obtained from a DTI acquisition in the same subject and registered to the anatomical image. The susceptibility tensor in the subject frame, defined by the anatomical image, was calculated using the relation $\boldsymbol{\chi} = \mathbf{R}^{\mathrm{T}} \boldsymbol{\chi}_{T} \mathbf{R}$, and the field inhomogeneity due to this susceptibility distribution was simulated using the forward problem Eq.3.12. Noisy phase data for this simulation was generated in the same fashion as the above numerical simulation.

The sensitivity of the anisotropy estimation to various acquisition orientations

was investigated in this simulated data set. Three types of tensor reconstructions were generated as follows: 1) using the same three orientations as acquired on the Subject 1, 2) using the 12 orientations acquired on the Subject 1 and 3) using twelve orientations evenly distributed over a sphere; these acquisition schemes are referred to as human 3, human 12 and uniform 12 respectively. The anisotropies generated from these reconstructions were evaluated against the known anisotropy in the simulation. An error map was generated by plotting the average error for every encountered fiber direction. To depict the orientations represented in this numerical brain, a 3D histogram was displayed as a 2D intensity map.

3.2.4 Experimental Anisotropic Phantom

The anisotropic phantom consisted of a bundle of parallel carbon fibers (12K carbon fiber tow, Aerospace Composites), a known source of cylindrically symmetric susceptibility anisotropy (14) approximately 3cm in length and 3mm in diameter immersed in a 1% agarose gel background in a cylindrical container (10cm diameter, 6cm height). The direction of the fibers used for the CSST reconstruction was obtained by determining the axis of the bundle from the magnitude image. Two water balloons were added as isotropic references containing 2.5 and 5mM of Magnevist, which corresponded to susceptibilities of 0.8ppm and 1.6ppm, respectively. Multi-echo gradient data was acquired in twelve distinct orientations uniformly distributed over the unit sphere.

For this phantom, three types of tensor reconstructions were performed on the acquired data: the CSST and STI reconstructions using all twelve orientations and the

3-CSST for each of the 220 combinations of three orientations out of the available twelve. The relationship between the molar susceptibility of gadolinium is well known; since there is no inherent anisotropy within the gadolinium solutions, their magnetic susceptibility tensors should be defined by a single scalar susceptibility. Accordingly, anisotropy within the eigenvalues of the gadolinium phantom was used as a measure of error in the estimated susceptibility tensor. The MSA from each concentration of gadolinium across the reconstructions was compared for consistency of the estimated anisotropy. A histogram of the MSA of the 220 3-CSST reconstructions was constructed to examine bias in the anisotropy from these reconstructions. The mean magnetic susceptibility, or MMS, defined as

$$MMS = (\lambda_1 + \lambda_2 + \lambda_3)/3 \quad [3.25]$$

was calculated for each of the balloons. The prepared concentration of Gadolinium was converted to ppm using the molar susceptibility of 326 L/mol (3). A regression analysis against the prepared gadolinium susceptibility was performed to examine errors in the reconstructions of isotropic materials.

3.2.5 Human Subject Study

Human studies were performed with approval from our institutional review board. In four healthy volunteers (3 male, 1 female, age 28±2.9 years), the 3-CSST was calculated from 3 acquisitions with isotropic 1.5x1.5x1.5mm^3 resolution in the supine position, including neutral, left- and right-leaning orientations. One volunteer, Subject 1, consented and was able to perform an additional 9 orientations using a

combination of neutral, left-, right-, forward- and backward-leaning orientations in supine and prone positions. On this volunteer, all twelve orientations were used to reconstruct the tensor with and without symmetry constraints (12-CSST and 12-STI), and all possible 3-CSST reconstructions were performed for each set of 3 orientations within the available set of twelve (220 combinations). On all susceptibility tensor reconstructions, the MSA and MMS were measured in predefined ROIs in four major white matter tracts, including the splenium, body and genu of the corpus callosum (SCC, BCC and GCC, respectively), and optic radiations (OR). Summary statistics were calculated across all volunteers and reported as mean ± standard deviation unless otherwise stated. Histograms were generated over all 3-CSST reconstructions in Subject 1 in the white matter ROIs. For human subjects, the analysis of the results focused on major white matter tracts, where the principal fiber direction was assumed to be uniform with few crossing fibers. The principal eigenvectors for the estimated DTI and STI reconstructions in Subject 1 correspond to the principal eigenvalue, signed maximum value, in the eigenvalue decomposition. The absolute value of the dot product of these vectors, $|V_{1STI} \cdot V_{1DTI}|$, is used here to indicate the degree of alignment between them, with 1 indicating aligned and 0 orthogonal vectors. Alignment in ROIs identified in the brain, SCC, BCC, GCC, OR and centrum semiovale (CS) were compared with a one-way ANOVA.

3.2.6 Data Acquisition

All experiments were performed on a 3T clinical MR scanner (General Electric Excite HD; GE Healthcare, Waukesha, WI, USA). An 8-channel head coil was used

for the phantom study. A sample holder was constructed from a Styrofoam ball to reproducibly reorient the sample evenly over a sphere. A total of 12 acquisitions were obtained at an isotropic resolution of $1mm^3$. These orientations were acquired with a multi echo gradient echo (MEGRE) sequence with a total of 8 echoes and echo time (TE) spacing of 3.4ms and repetition time (TR) of 71.6ms, flip angle of 15°, bandwidth of 62.5kHz, acquisition matrix of 130x130x116, field of view (FOV) of 13cm, and a slice thickness of 1mm. In the phantom, DTI information was not reliable due to the lack of observed restricted diffusion signal in both the isotropic and anisotropic sources.

The MEGRE sequence was also used for the volunteer studies, but with the larger transmit/receive head coil to allow for a greater degree of rotation. Imaging parameters were as follows: 11 echoes with TE spacing of 2.64ms, TR of 46.94ms and $1.5x1.5x1.5mm^3$ resolution. The 9 additional orientations were acquired on Subject 1 to allow a 12-STI reconstruction. A 2D echo planar imaging (EPI) dual spin echo DTI sequence was used to acquire diffusion tensor data on each of the volunteers with a resolution of $2x2x2.4mm^3$, with parameters: 33 directions, b value of $1000s/mm^2$, 22cm FOV, acquisition matrix of 110x110, 2.4mm slice thickness, 17sec TR, 85.3ms TE and bandwidth per pixel of 1953.12Hz.

3.2.7 Data Processing

Phase information was calculated from the complex MRI signal. Phase data were first temporally unwrapped across echoes. Next, the resulting multi-echo phase data were linearly fit to estimate the field inhomogeneity relative to the $\mathbf{B}_0$ field

(3,46). Subsequent spatial unwrapping of this field map was performed with a region growing algorithm (47). The background field was removed using the projection onto dipole fields method (48). All tensor calculations were performed in MATLAB using a conjugate gradient solver. Spatial warping of the diffusion data was corrected and registered to the gradient echo data using FUGUE and FLIRT (49). The registration between the orientations and the subject frame was used to determine the $\hat{\mathbf{b}}$ vector in each of the orientations. Estimated MMS was calculated from the reconstructed susceptibility components. Since the MSA is insensitive to the choice of reference, no such reference was determined in phantom and human data.

3.3 Results

3.3.1 Estimation of the Condition Number for the 3-CSST

The 560 sets of 3 orientations in the simulated phantom showed the following condition min/median/max numbers: $9.4\text{x}10^{3}$/ $3.2\text{x}10^{5}$/ $3.1\text{x}10^{11}$, after excluding one infinite condition number for the set of 3 orientations that were aligned close to a single plane. Twenty of these 560 sets contained human feasible orientations, having the min/median/max condition numbers of $2.0\text{x}10^{4}$/ $7.1\text{x}10^{5}$/ $1.8\text{x}10^{8}$. Preliminary experiments with larger matrix sizes did not significantly affect the calculated condition number of this system.

3.3.2 Numerical Phantom Simulation

Both 16-CSST (MSA:20±1.2 parts per billion, ppb) and 16-STI

(MSA:19±1.6ppb) gave reconstructed MSA in close agreement with the truth; giving -0.5% and -5.5% error, respectively. 96% of all simulated 3-CSST reconstructions estimated the MSA of the fiber within 10% of the true MSA; the 3-CSST of human orientations was in this 10% error group with an average of -2.4% error. There was a tail in the distribution biased towards higher MSA. An outlier at the end of the tail had sampled $\hat{\mathbf{b}}$ directions (represented in the inlaid plot of Fig. 3.3b) that were largely perpendicular to the $\chi_{\parallel}$ direction (along the x axis).

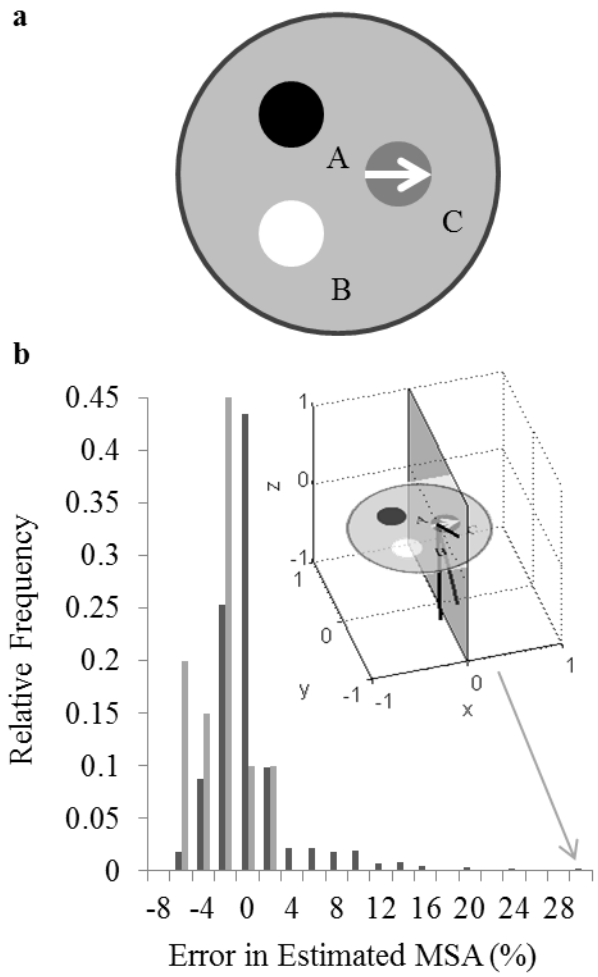

Figure 3: a, shows a slice through the simulated phantom displaying the configuration

of the isotropic sources, A and B, and anisotropic susceptibility source C with its orientation along the x axis (white arrow). b, Error in mean anisotropy detected in the simulated fiber over all combinations of possible 3-CSST reconstructions. Light gray bars indicate human feasible acquisitions and dark gray bars indicate all possible combinations of three orientations. The three black lines on the y-z plane in the inlaid figure indicate the three $\hat{b}$ directions for the outlier 3-CSST MSA result of 29.6% error (gray arrow).

3.3.3 Numerical Brain Simulation

The true MSA map and reconstructed MSA maps are shown in the top row of Fig.3.4. The distribution of fiber orientations in the simulation and the observed error in the reconstructed MSA with respect to fiber orientation are shown in the bottom row of Fig.3.4.

The MSA as measured by the 3-CSST had erroneous hyper- and hypo-intense bands (over- and under-estimation) in the regions of the body of corpus callosum and the centrum semiovale (BCC and CS, respectively; white and black arrows/circles in the top/bottom of Fig. 3.4). The intensity of these error bands was reduced when the reconstruction was based on the set of 12 human feasible orientations and was significantly diminished with a uniformly distributed set of 12 orientations. The MSA error varied substantially with fiber orientations.

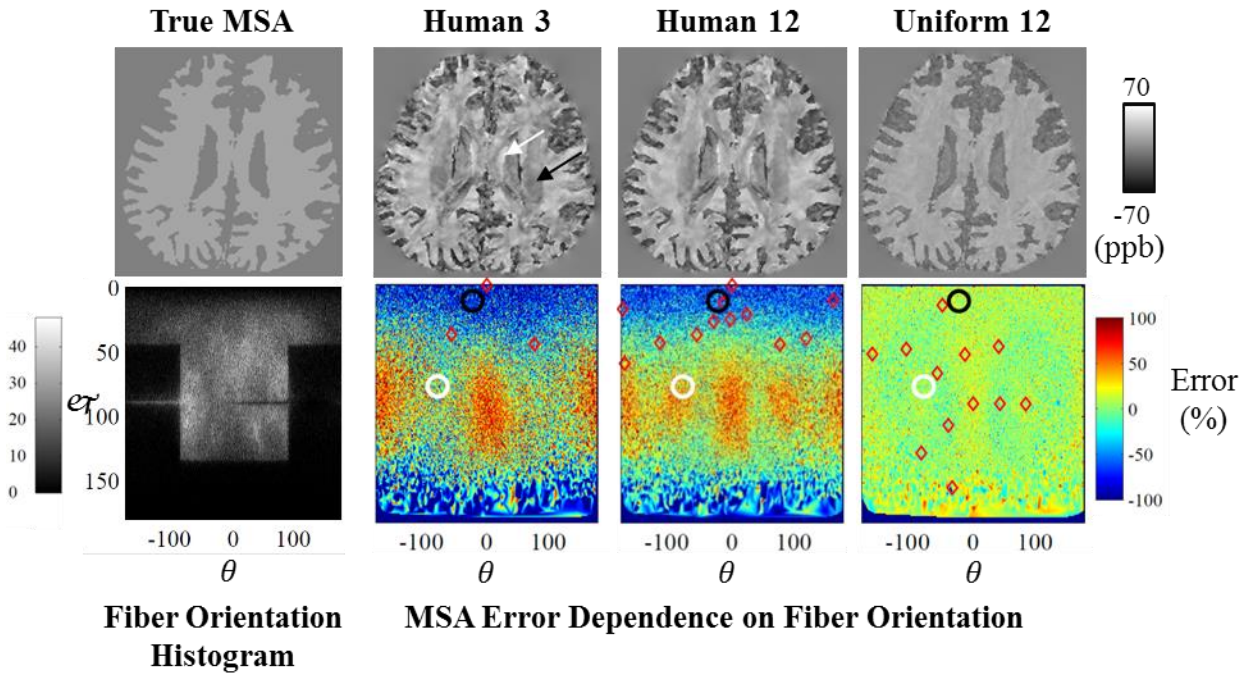

Figure 3.3: Estimation of white matter MSA using realistic fiber orientations with various CSST reconstructed MSA (top row) and associated errors (bottom row). The lower left corner shows a histogram of the fiber orientations estimated from experimental human data (the black region corresponds to few samples). Red diamonds in the error maps represent the $\hat{b}$ directions in each of the corresponding MSA maps in the top row. The white and black circles in the error maps correspond to the regions indicated by the white and black arrows in the MSA maps respectively.

3.3.4 Experimental Anisotropic Phantom

The image quality of the 12-CSST and 12-STI reconstructions were similar, and both were superior to that of the 3-CSST (Fig.3.5a), consistent with observations in the simulated phantom; data not shown. The MSA estimated by the 12-CSST (740 ppb) was not significantly different from that estimated by the 12-STI (770 ppb, p=0.56). The mean MSA of the 3-CSST reconstructions was 650 ppb, 12% lower than the 12-CSST/12-STI estimates. In the 3-CSST with orientations restricted to a human feasible range, the MSA was further skewed towards the lower end of the distribution (Fig.3.5b). All estimated MSAs for the carbon fiber were within the range of values

reported in the literature (50).

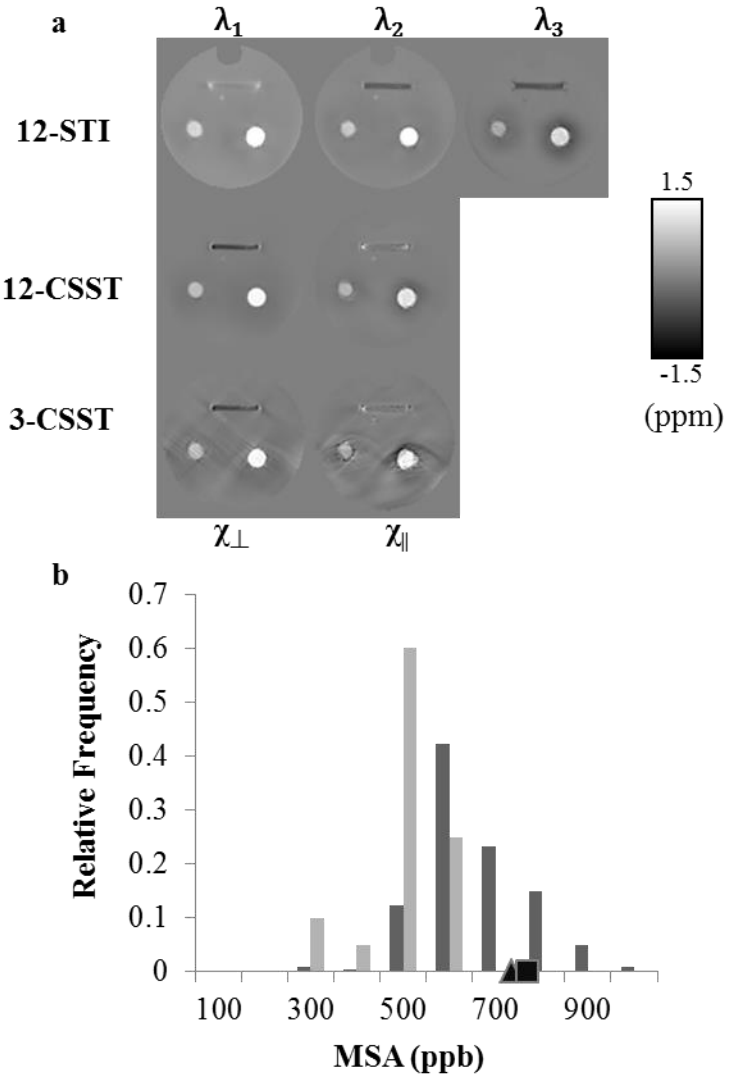

Figure 3.4: a, Eigenvalues of the STI and parallel and perpendicular components of the CSST reconstructions of the phantom consisting of both isotropic and anisotropic materials. b, Histograms of MSA detected in the carbon fiber over all 3-CSST reconstructions of the phantom (dark gray bars) and the sets of 3-CSSTs that lie within a human feasible range (light gray bars). The black triangle and square indicate the location of the mean anisotropy detected in the 12-CSST and 12-STI reconstructions respectively.

In the gadolinium balloons of this phantom, regression analysis showed similar

fits of mean susceptibility in the gadolinium balloons with a slope of 0.86 (R^2 = 0.98) for 12-CSST, 0.86 (R^2 = 0.91) for one 3-CSST and 0.89 (R^2 = 0.97) for 12-STI; no statistical difference, P>0.05 between regressions.

3.3.5 Human Subject Study

For Subject 1 with all 12 orientations, 12-STI, 12-CSST and 3-CSST were successfully reconstructed. The traces of these reconstructions (in Fig. 3.6) demonstrated striking similarity with increased noise with fewer orientations. The MSA maps of 12-CSST and 3-CSST were similar, but this visual similarity was limited to the major white matter tracts when compared to the MSA map of 12-STI (Fig. 3.7).

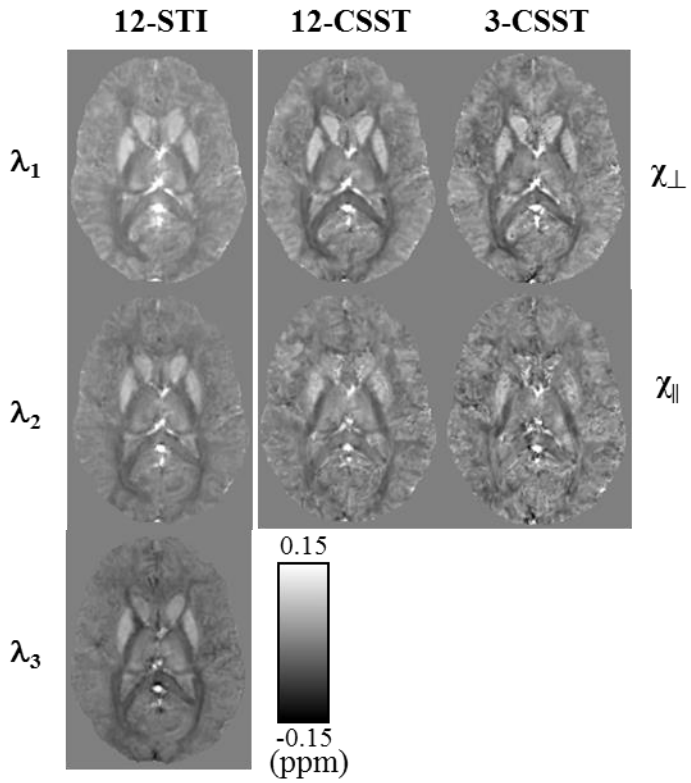

Figure 3.5: Diagonal components of the 12-CSST and 3-CSST reconstructions and the eigenvalues of the 12-STI reconstructions from Subject 1.

A comparison of the STI versus DTI principal eigenvector maps in Subject 1 showed high correspondence in some anatomical regions like the corpus callosum and optic radiations, but regions that were oriented along the SI direction showed poor alignment. It was found that the absolute value of the dot product resembled the pattern in the estimated anisotropy maps, particularly in the axial plane, Fig. 3.7 versus the middle row of Fig.3.8.

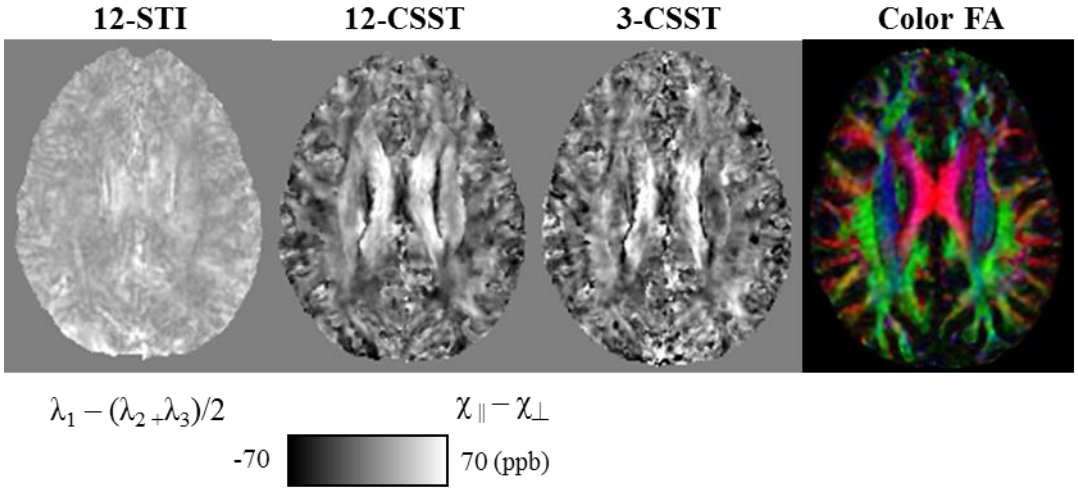

Figure 3.6: Comparison of MSA maps generated within Subject 1 compared to the color FA generated from the diffusion data.

The SCC ($|V_{1STI} \cdot V_{1DTI}|$: 0.44±0.30), BCC (0.69±0.29), GCC (0.68±0.28) and OR (0.56±0.27) were all regions that laid in planes mostly perpendicular to the SI direction and all showed significantly stronger alignment compared to the CS (0.38±0.25, $P < 0.05$ using a multiple comparison test), which was mostly oriented along the SI direction as determined by DTI. The mean susceptibility maps of all three reconstructions showed many similarities with the scalar reconstruction of the neutral orientation of the brain (Fig. 3.9). The 3-CSST MSA maps were largely consistent across volunteers for the axial, sagittal and coronal planes (Fig. 3.10).

Table 3.1: Mean MSA detected across 3-CSST reconstructions of all volunteers, in ppb

	SCC	**BCC**	**GCC**	**OR**
Subject 1	5 ± 21	20 ± 38	-24 ± 28	30 ± 24
Subject 2	14 ± 12	31 ± 24	-31 ± 14	30 ± 22
Subject 3	8 ± 16	22 ± 23	-35 ± 13	31 ± 22

Subject 4	-7 ± 18	37 ± 24	-1 ± 13	27 ± 23

The 3-CSST mean MSA values measured in 4 major white matter tracts were listed in Table 1 for all subjects. The MSA for reconstructions in Subject 1 are listed in Table 2.

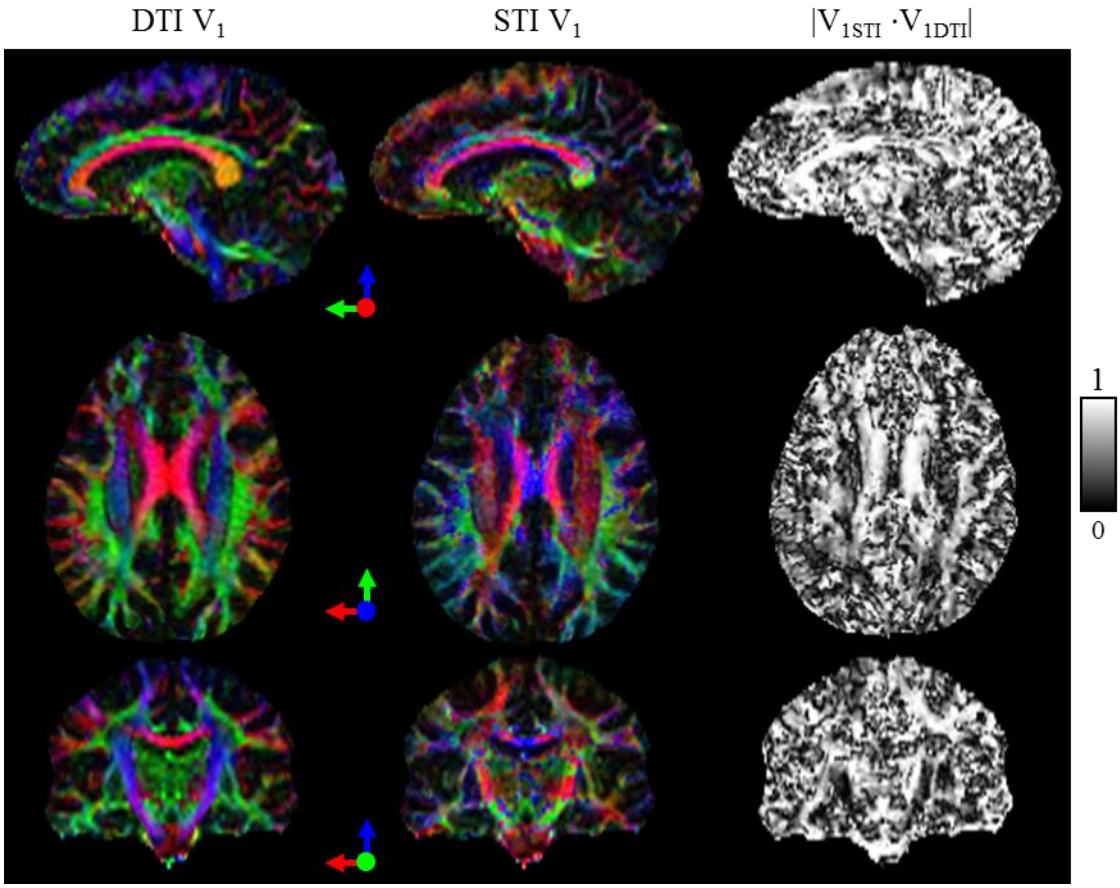

Figure 3.7: First and second columns: maps of the principal eigenvector direction as derived from DTI and STI (both weighted by the FA from DTI) in sagittal (top), axial (middle) and coronal (bottom) section. Directions are color coded according to the arrows. Third column: the absolute value of the dot product between the vectors.

Table 3.2: Mean MSA detected across reconstructions of 12 orientations in Subject 1, in ppb

	SCC	**BCC**	**GCC**	**OR**

12-STI	34 ± 13	37 ± 13	43 ± 14	37 ± 13
12-CSST	17 ± 14	30 ± 38	4 ± 20	7 ± 18
3-CSST	5 ± 21	20 ± 38	-24 ± 28	30 ± 24

There was reasonable consistency among the measured MSA values of the BCC across all subjects and among all reconstructions in Subject 1. There was also reasonable consistency among all subjects for 3-CSST MSA values of the OR. Compared to BCC, there were larger variations for MSA values of GCC and SCC. The MSA values for all 220 possible 3-CSST reconstructions were plotted for the 4 identified white matter tracts (Fig. 3.11), showed less spread in BCC and SCC than GCC and OR.

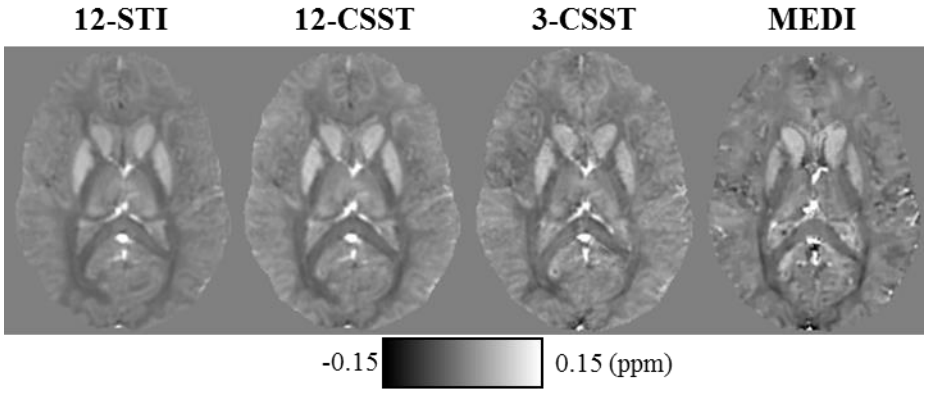

Figure 3.8: Mean magnetic susceptibility, from each of the susceptibility tensor reconstructions compared to a scalar susceptibility reconstruction of the neutral orientation.

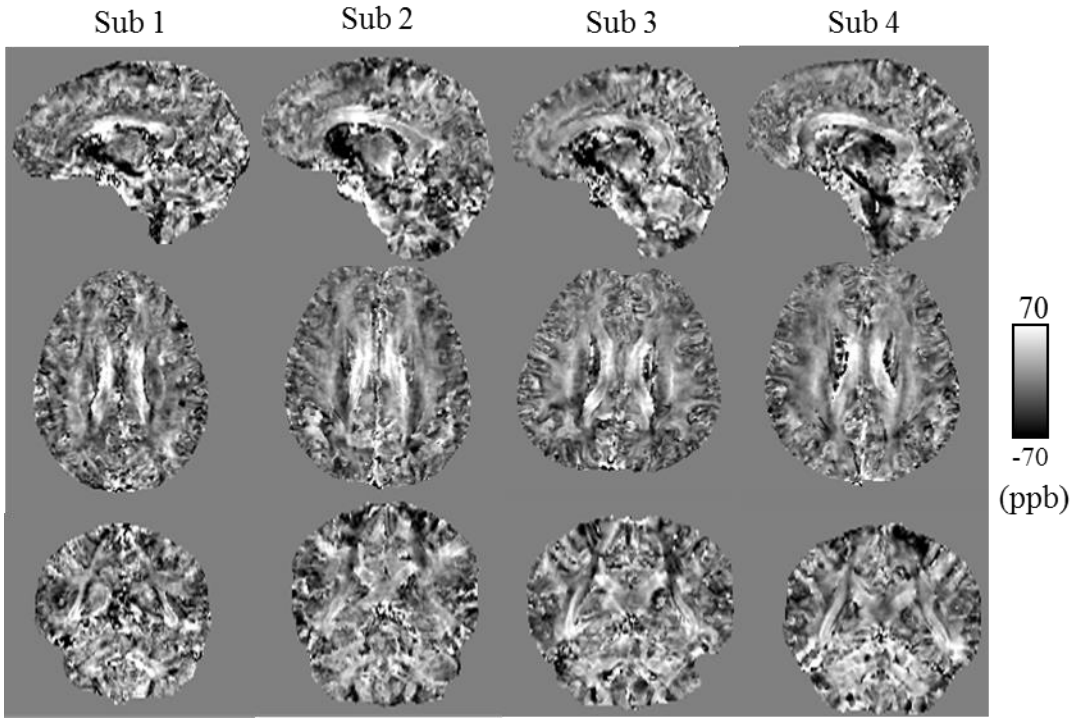

Figure 3.9: MSA maps generated from the 3-CSST of all of the volunteers, view in sagittal (top), axial (middle) and coronal (bottom) section.

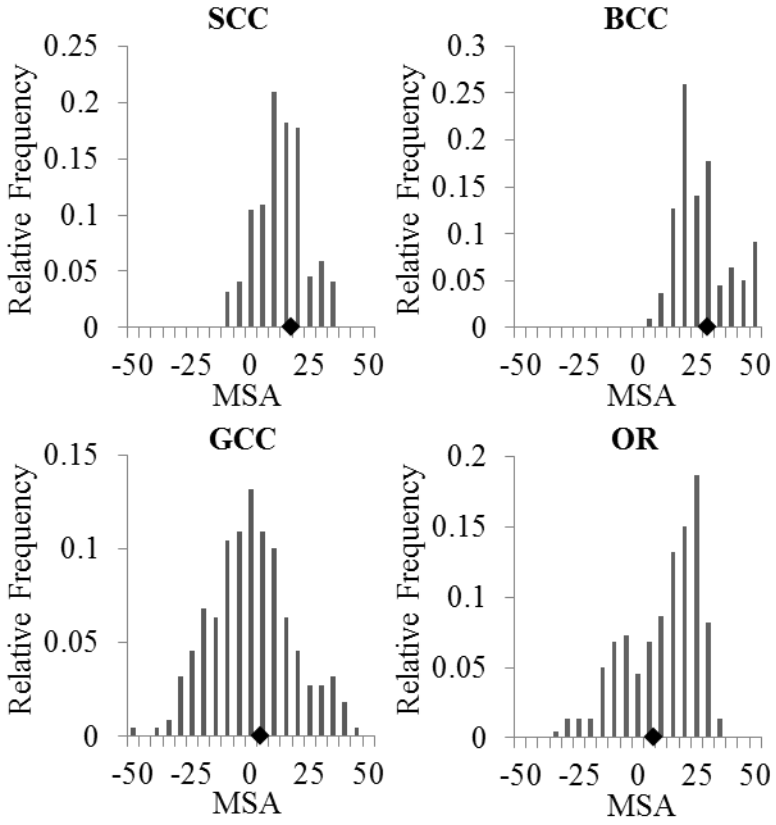

Figure 3.10: Histograms of the mean MSA (ppb) in white matter regions over all 220 combinations of 3-CSST from acquired orientations in Subject 1; the black diamonds mark the mean MSA estimated from the 12-CSST.

3.4 Discussion

Our analysis of decomposing macroscopic tissue magnetic susceptibility into a sum of microscopic molecular magnetic polarizabilities demonstrates that susceptibility anisotropy observed in MRI requires both intrinsic anisotropy in molecular polarizibility and macroscopic order in molecular arrangement. Order achieved by restricting a molecules' axis to lie in a plane or a line lead to cylindrical

symmetry in the susceptibility tensor. Myelin lipids are a major source of susceptibility anisotropy of the major white matter tracts in the human brain. These structures have a macroscopic arrangement observable at the resolution of MRI, allowing the cylindrical symmetry model to be used in susceptibility tensor imaging (STI).

Neurological diseases such as multiple sclerosis (51) or rare hereditary neuropathies can affect the formation of myelin and lipid metabolism, which can greatly affect the presence and appearance of myelin (52-54). The abnormal formation of myelin would undoubtedly affect the symmetry of the myelin sheath. These changes are very inconsistent on a microscopic scale and all such syndromes appear lead to eventual demyelination (52-54). As a consequence to the reduced macroscopic order in lipids, we may expect reduced anisotropy in macroscopic susceptibility in diseased myelin. It has been observed within Shiverer mice that demyelinated white matter showed significant loss in MSA (17). Further evidence may be obtained from other mouse models of demyelination or dysmyelination and from patients with demyelinating diseases. Conversely remyelinated axons appear to regain some of the function of normal neurons and some of the cylindrical symmetry in the organization of lipid layers. (55). This remyelination process could be monitored by measuring the increase in MSA.

The cylindrical symmetry of the susceptibility tensor (CSST) can be estimated from diffusion tensor imaging (DTI) and can then be used to obtain an estimation of MSA of the white matter tracts of the brain from a reduced number of subject orientations.

Our results in simulation, phantom and human studies show the reconstructed susceptibility tensor is very sensitive to the distribution of acquired subject orientations used in the reconstruction, which was not explored previously. With judiciously chosen 3 non-planar orientations in the human study, it was found that, the 3-CSST reconstruction had similar tensor anisotropy in main white matter regions compared to the 12-CSST and 12-STI reconstructions directly in this study, the in vivo anisotropy maps in earlier work with more orientations and/or higher field strength (17,25), and the anisotropy of white matter measured in vitro (10).

The reduction in the number of sampling orientations is highly desired in practice for STI. Acquiring all 12 orientations in a single volunteer required a total of 4 hours of scan time. In addition to the long scan time to acquire a single orientation (~10 min in this study without parallel imaging), repositioning and stably holding a human head at various orientations required particular care and time in preparing for each of the scans. Completing all 12 orientations demanded substantial cooperation from the subject and the subject had to take breaks between scan sessions. For this reason, we were only able to achieve 12 orientations in one subject. In contrast, the three orientations studies were easily acquired in every subject within 1 hour, which may be further shortened using parallel imaging. The three orientations (neutral, left and right leaning) performed by all volunteers in this study were tolerable. Additional orientations increase subject discomfort particularly when tilted forward or backward, which leads to decreased image quality due to motion and poorer field measurements. This reduction in time to within 1 hour and increase in subject tolerance are critical for

both exploring clinical possibilities and research investigations requiring larger numbers of subjects.

Characterization of tensor anisotropy in STI is not as easily defined as it is in DTI. The fractional anisotropy (FA) commonly used in DTI for the characterization of the anisotropy of a tensor no longer has a meaningful interpretation with FA=0 as isotropic and FA=1 as a line for the susceptibility tensor; because components can be negative resulting in values for FA greater than 1. We also found FA to be too sensitive to the noise in STI, which has much poorer SNR than DTI. One may achieve an anisotropy measurement robust against noise and sensitive to high susceptibility anisotropy by adding a regularizing constant to the tensor components (48). However, this may introduce a bias that varies with the regularization constant. With cylindrical symmetry each voxel is constrained to two principal susceptibility coefficients parallel and perpendicular to the fiber axis. Their difference, or MSA, is 0 for isotropic materials. Deviations away from 0 indicate anisotropy. This measure has been previously used to define susceptibility tensor anisotropy (25,50), and can be extended for a general susceptibility tensor using its eigenvalues in STI.

Fundamentally, STI is an extension of the inverse problem of quantitatively determining the scalar susceptibility map from MR field measurements (QSM), which has an intrinsic ill-posedness arising from the zero cone surfaces of the dipole kernel in the Fourier domain. STI requires additional susceptibility parameters, further exacerbating the ill-conditioned nature of the STI inversion problem. The CSST uses tensor frame orientation information to reduce the number of unknowns to two

parameters per voxel. This reduces but does not eliminate the ill-conditioning of determining the two tensor susceptibility parameters, perhaps due to the zeroes of coefficients (resembling dipole kernel coefficient in QSM) of the 2x2 linear system of equations (Eq.3.22). This ill-posedness can be characterized in a detailed analysis of the condition number for the CSST, similar to that for the COSMOS method of QSM (43,56). Examination of 3-CSST over a range of orientations showed poor condition numbers ranging from 104 to 1011. The choice of 3 human orientations limits how far the condition number can be brought down. The worst error propagation was observed when the 3 orientations were roughly planar, leading to erroneous estimation of MSA. Accordingly, co-planar 3 orientations have to be avoided in implementing 3-CSST. Further investigation to improve estimation of the susceptibility tensor may include identifying an optimal configuration of orientations that produces the best conditioned system, and formulating a Bayesian approach that allows use of prior information similar to QSM (3,31,33,35,56-58).

It was found that the simulated 3-CSST reconstruction of orientations uniformly spread over a sphere provided fairly accurate estimation of the true susceptibility anisotropy, most within 10%. However, the 3-CSST is sensitive to the sampling angles (Fig. 3.3). In addition to the sampling angle dependence $\left(\mathbf{k}\cdot\hat{\mathbf{b}}\right)$ shared with QSM, there is an additional susceptibility tensor angle dependence $\left(\mathbf{X}\cdot\hat{\mathbf{b}}\right)$ unique to tensor imaging. When the 3 orientations are nearly coplanar, tensor components perpendicular to the plane do not contribute significantly to the observed field shifts in any orientation (Eq. 3.12), which poorly conditions the inverse problem contributing

to large noise propagation in these components. Specifically, for the limited human range of orientations, the 3-CSST reconstruction may appear to be skewed, and the MSA detected may be erroneously high (Fig. 3.3).

Further simulations of realistic fiber directions and estimation of MSA show that within a particular set of three acquisitions, the MSA error maps (Fig. 3.4) show regions of consistent over- and under-estimation. The MSA error maps reflect the noise propagation into the reconstructed tensor components; the variance in the components was on the order of 0.01ppm in white matter and yielded possible errors of up to ± 50% for any particular fiber, Fig. 3.4. Less error is observed when more orientations are incorporated into the cylindrically symmetric reconstruction (such as the 12 orientations acquired in Subject 1), and when those orientations are more evenly distributed (such as the 12 uniformly distributed orientations). From these observations, high SNR and evenly distributed orientations were shown to be necessary for consistent estimation of susceptibility anisotropy with a realistic distribution of fiber orientations like those observed in the human brain even with the symmetry constraint.

A comparison of the MSA maps for the simulation and the volunteers, Fig. 3.4 vs. Fig. 3.10, showed similar regions of hyper- and hypo-intensity. In the simulation, this led to both under- and over-estimation of the anisotropy due to the distribution of acquisition directions unfavorable to those fibers. In the human data, there are many factors that are not accounted for in the simulation, such as the density of fibers and crossing fibers that exist in various regions in the human brain, which would also

affect the MSA of the white matter. The brain simulation demonstrates that the distribution of orientations is a contributing factor to errors in the MSA in the human brain, particularly in the BCC and CS, as shown in Fig. 3.4.

There is a high degree of alignment between principal eigenvectors of diffusion tensors (DT) and susceptibility tensors (ST) in the corpus callosum and optic radiations, but there is also poor alignment in the centrum semiovale (Fig. 3.8). The pattern of the observed errors in the estimated MSA in the brain simulation is consistent with that of misalignment of the DT and ST eigenvectors of major white matter tracts in the human study. MSA underestimation for fibers parallel to the SI direction in the simulated brain (ϕ=0 in Fig. 3. 4) corresponds to poor alignment between DTI and STI eigenvectors in the human data (Fig. 3.8). Differences in alignment could be due to errors in the STI reconstruction from limited human orientations or intrinsic differences between the ST and DT principal eigenvectors. The limited range of human orientations causes errors in the STI reconstruction, which may contribute to misalignment between the ST and DT. In the periphery of the brain, there are crossing fibers that may make it difficult to estimate DT eigenvectors and their alignment with ST eigenvectors. Our experimental data show that, for most major white matter tracts, the DTI derived prior information could be a reasonable estimate of the principal direction of the susceptibility tensor.

It is not straightforward to compare estimates of anisotropy between STI and CSST reconstructions. MSA from the STI reconstruction is always positive due to the ordering of the eigenvalues and there is no natural way to define parallel and

perpendicular components explicitly in this reconstruction. This leads to decreasing variability of the MSA estimates, which are now by definition positive. The error in susceptibility tensor reconstruction is determined in large part by the noise amplification of the poorly conditioned inverse problem. This suggests that the constrained reconstruction also has the added benefit of denoising in situations where the known tensor symmetry can be used to improve the condition of the inversion.

Susceptibility tensor imaging of the human brain is challenging due to the limited range of orientations available to sample the orientation dependence of the magnetization. The lack of ground truth adds to the challenge. The center of k-space for the susceptibility tensor map is not determined, making a reference for the absolute susceptibility of any particular region difficult to define in a human subject. The focus of this study, MSA, is based on a difference of components, which should not be sensitive to this issue. The genu of the corpus callosum is particularly difficult to reconstruct in both the scalar and tensor susceptibility cases due to reduced SNR near the air tissue interfaces of the frontal sinuses. Imperfect background field removal further complicates reconstructing susceptibility tensor in some regions of the brain. Consequently, the reliability in estimating MSA is low in some regions of the brain. This may explain the greater variability observed in the genu of the corpus callosum than in other regions of the brain Table 2 and Fig. 3.11. While it is relatively easy for healthy volunteers to perform three orientations in the MR scanner, patients may have difficulties performing three head orientations, and the acquisition time of three orientations may be too long to be part of a clinical protocol. Given the dependence of

MSA on the choice of the orientations for the 3-CSST (Fig. 3.11) the ability of a volunteer to follow instructions to perform the orientations may also affect the estimated anisotropy map.

STI shares many of the problems of DTI in estimating tensor components and anisotropy on a voxel level. For example, even with an ideal distribution of samples over a sphere, voxels containing crossing fibers pose a problem when reconstructing the tensor. A single MSA value as determined by the average tensor in the voxel may not reflect the different components present in that voxel. In the diffusion tensor case, this phenomenon effectively decreases the detected diffusion anisotropy erroneously (59). In these voxels, the principal diffusion direction may not be the parallel axis of the susceptibility tensor. Additionally, for the CSST reconstructions, DTI has a lower resolution when compared to the gradient echo data and thus the resolution with which DTI can determine the direction for thinner white matter tracts in the brain is reduced. This in turn lowers the confidence with which the assumption of symmetry can be applied in these voxels. This phenomenon may account for some of the differences in the susceptibility observed at the edges of anatomical structures or in the center of the corpus callosum at the gap between the hemispheres. However, increasing the resolution of the EPI based DTI acquisition also increases the noise in the images, which then reduces the reliability of the diffusion directions. As a result, the CSST constraint may only be appropriate for specific regions of the brain. Further investigations are needed to explore similarities and differences between diffusion and susceptibility tensor frames. For qualitative mapping of susceptibility anisotropy of

white matter tracts, our volunteer data suggest that the instructions for this 3-CSST may be robust enough in practice.

3.5 Conclusion

In this work we have explored theoretical and experimental aspects of estimating MSA in white matter tracts from human feasible data. We have shown cylindrical symmetry in susceptibility anisotropy from configurations of molecules with orientations similar to the non-rigid structure of the myelin sheath. Cylindrical symmetry can be used to improve the condition of estimating the susceptibility tensor, CSST, from MRI acquired with few subject orientations. Our analysis of noise propagation shows the error in the estimated MSA of the CSST is sensitive to the relative angle between the fiber direction and the acquired orientations of the subject, with substantial error observed when the subject orientations are coplanar. We find that DTI guided estimation of cylindrical MSA in major white matter tracts of the brain can be reasonable with as few as three non-coplanar orientations particularly in the corpus callosum and optic radiations.

CHAPTER 4

4 THE INFLUENCE OF MOLECULAR ORDER AND MICRO-STRUCTURE ON R2* RELAXATION AND MAGNETIC SUSCEPTIBILITY TENSORS

The study of the magnetization and relaxation properties of molecularly ordered materials is of particular interest in studying white matter fibers. In this work we present a study of the effect of composition and organization on the magnetic field within white matter as measured with both relaxation and susceptibility anisotropy. We demonstrate that voxels that contain both sub-voxel structure and molecular order can lead to relaxation and susceptibility anisotropy, whereas absence of intrinsic molecular order leads to anisotropy only in relaxation. We find a significant structural correspondence between diffusion, susceptibility and relaxation measurements in the white matter in vivo, providing evidence for the contribution of anatomical structural and molecular order to the MR signal. In this work phantom studies are used to investigate relaxation and susceptibility tensors of materials with and without intrinsic molecular order and micro-structure to demonstrate the effects of sub-voxel architecture. A wild bootstrap analysis of the relaxation and susceptibility reconstructions is performed to examine confidence in the estimated orientation of these tensors. R2* and STI thus reveal information about the structure of the tissue and molecular organization.

4.1 Motivation and Background

There has been substantial interest in measuring microstructure of the brain from the macroscopic MRI voxel signal. The R2* in white matter is dependent on fiber orientation with respect to the applied field and has been used to examine white matter fiber architecture (11,13,60,61). The orientation dependence of R2* arises from the field inhomogeneity induced by the composition and arrangement of susceptibility sources. The interpretation of R2* in MRI is non-trivial; consisting of both the rate of T2 relaxation and the effects of field inhomogeneity in that voxel. The latter often dominating R2*(2). Both local sources of magnetization within and outside can affect the field inhomogeneity within the measured voxel.

Recently, magnetic Susceptibility Tensor Imaging (STI) was introduced to provide a more direct way to examine the magnetization of tissues with molecular order, such as myelin (6,17,62). The highly organized structure of myelin (9) in white matter of the brain has been studied with susceptibility tensor reconstructions in vivo and in vitro (6,17,21,48,62). These studies demonstrate significant anisotropy in STI similar to that obtained with diffusion tensor imaging (DTI) (59).

		Micro-structural Properties	
		Organized	Disorganized
Molecular Properties	Anisotropic	**I** Carbon Fiber Bar/ Ring (white Matter) R2* and STI anisotropy	**II** Carbon Fiber Bits R2* and STI isotropy
	Isotropic	**III** Capillary Tubes (blood Vessels) R2* anisotropy only	**IV** Gadolinium Balloons R2* and STI isotropy

Figure 4.1: Molecular and micro-structural properties under examination, each case (I, II, III and IV) list the associated relaxation and susceptibility tensor properties.

We investigate both R2* and susceptibility tensors simultaneously for their dependence on microstructure and molecular properties using specifically designed phantoms. Examples of the effects observed in the phantom studies are then examined in human brain data; in white matter fiber tracts and deep periventricular veins. Because of the increased sensitivity to noise of the R2* and susceptibility tensor anisotropy (13,17), the tensor eigenvectors are compared instead, using a wild bootstrap analysis to measure the confidence in the measured eigenvectors. This allows us to quantify and compare the stability of the principal axes of the tensors. We find significant correlation of the eigenvectors in major white matter tracts between susceptibility and R2* measurements, but not in deep periventricular veins, consistent with the presence of molecular order and microstructure.

4.2 Theory

We recently demonstrated that the susceptibility anisotropy requires both microstructure and molecular anisotropy (62). We briefly review susceptibility tensor imaging and focus on R2* anisotropy caused by microstructural anisotropy regardless of molecular anisotropy.

4.2.1 Susceptibility Tensor Imaging (STI)

Susceptibility anisotropy arises from the presence of ordered anisotropic molecules within the voxel; as observed in vitro and in vivo (17,21,48). The magnetization of biomaterials under an applied field $\boldsymbol{B}_0$is proportional to the magnetic susceptibility of the source (26):

$$\boldsymbol{M} = \boldsymbol{\chi}\boldsymbol{B}_0/\mu_0, \qquad [4.1]$$

where $\boldsymbol{\chi}$ is an approximate summation of the polarizability tensors of all molecules in a voxel (62). The relationship between the applied field and the resulting field of material magnetization can be expressed in Fourier space (k-space)(6):

$$\Delta(\boldsymbol{k}) = \frac{\hat{\boldsymbol{b}}\cdot(\boldsymbol{X}\cdot\hat{\boldsymbol{b}})}{3} - \hat{\boldsymbol{b}}\cdot\boldsymbol{k}\,\frac{\boldsymbol{k}\cdot(\boldsymbol{X}\cdot\hat{\boldsymbol{b}})}{k^2}, \qquad [4.2]$$

where $\Delta(\mathbf{k})$is the field in k-space, $\hat{\boldsymbol{b}} = \boldsymbol{B}_0/|B_0|$, and $\mathbf{X}$ is the Fourier transform of susceptibility tensor $\boldsymbol{\chi}$. The solution for STI is computed as described previously, with a conjugate gradient solver (62),

$$\boldsymbol{X}(\boldsymbol{k}) = argmin_{\boldsymbol{X}(\boldsymbol{k})} \sum_p \left\| w_p \left(FT^{-1}\left(\Delta_p(\boldsymbol{k})\right) - FT^{-1}\left(\frac{\widehat{\boldsymbol{b}}_p \cdot (\boldsymbol{X} \cdot \widehat{\boldsymbol{b}}_p)}{3} - \widehat{\boldsymbol{b}}_p \cdot \boldsymbol{k}\, \frac{\boldsymbol{k} \cdot (\boldsymbol{X} \cdot \widehat{\boldsymbol{b}}_p)}{k^2}\right)\right)\right\|_2^2$$

[4.3]

4.2.2 R_2 Orientation Dependence*

The signal (*S*) at a voxel in a gradient echo image of echo time (TE) with a single species of protons can be modeled as:

$$S(v, TE) = e^{-TE\, R2} \int_v d^3\boldsymbol{r}\rho(\boldsymbol{r}) e^{-i\omega_0 \delta_b(\boldsymbol{r}) TE}, \quad [4.4]$$

where the integration is over the volume of the voxel (v), $\rho(\mathbf{r})$ is the spatial distribution of the proton density at position vector $\boldsymbol{r}$, ω_0 is the Larmor frequency and $\delta_b(\boldsymbol{r})$ is the field (scaled to $\boldsymbol{B}_0$) of magnetization in image space along the B_0 direction (63). The Fourier transform of Eq.4.2 is,

$$\delta_b(\boldsymbol{r}) = FT\left(\Delta(\boldsymbol{k})\right) = \widehat{\boldsymbol{b}}^t (\boldsymbol{d} *_m \boldsymbol{\chi})(\boldsymbol{r}) \widehat{\boldsymbol{b}}. \quad [4.5]$$

Here $\boldsymbol{d}$ and $\boldsymbol{\chi}$ are matrices for materials with anisotropic susceptibility and scalar for materials with isotropic materials and $*_m$ is the convolution of tensor fields, defined in the supplemental materials. The magnetic field at a location is the result of a convolution over all space; i.e. both nearby and distant sources. When the background field is sufficiently smooth, a Taylor expansion of Eq.4.4 to the second order shows (2)

$$S(v, \mathrm{TE}) = \rho(v) e^{-\mathrm{TE}\,(R2+R2')} e^{-i\omega_0 \delta_b(v)\mathrm{TE}}, \quad [4.6]$$

with an additional decay rate ($R2'$) dependent on the heterogeneity of the field $\delta_b(\mathbf{r})$ within the voxel:

$$R2' = \frac{1}{2} TE^2 \omega_0^2 (\langle \delta_b(\boldsymbol{r})^2 \rangle - \langle \delta_b(\boldsymbol{r}) \rangle^2)$$

$$= \tfrac{1}{2} TE \omega_0^2 \left(\tfrac{1}{\rho(v)} \int_v \, d^3\boldsymbol{r} \rho(\boldsymbol{r}) \delta_b^2(\boldsymbol{r}) - \left(\tfrac{1}{\rho(v)} \int_v \, d^3\boldsymbol{r} \rho(\boldsymbol{r}) \delta_b(\boldsymbol{r}) \right)^2 \right), \quad [4.7]$$

with $\rho(v) = \int_v \, d^3\boldsymbol{r} \rho(\boldsymbol{r})$

The variance of the field will follow the dependence of the field with orientation of the susceptibility material. This field depends on the orientation of the material if $\boldsymbol{\chi}$ is anisotropic or if $\boldsymbol{\chi}$ is isotropic but the geometry of the susceptibility distribution is anisotropic. This has been demonstrated in the case of infinite parallel cylinders of isotropic susceptibility (64).

The total rate of decay of the magnitude of the signal is expressed:

$$R2^* = R2 + R2' = \widehat{\boldsymbol{b}}^{\boldsymbol{t}} \cdot (R2 + \mathfrak{R}2') \cdot \widehat{\boldsymbol{b}} = \widehat{\boldsymbol{b}}^{\boldsymbol{t}} \cdot \mathfrak{R}2^* \cdot \widehat{\boldsymbol{b}} \quad [4.8]$$

The $\mathfrak{R}2'$ anisotropy corresponds to the $\mathfrak{R}2^*$ anisotropy, and the apparent decay rate depends on the orientation.

The elements of this $\mathfrak{R}2^*$ tensor (R2T) can be estimated from apparent decay rate, R2*, values measured at various orientations using a conjugate gradient solver:

$$\widehat{\mathfrak{R}}2^* = argmin_{\widehat{\mathfrak{R}}2^*} \sum_p \left\| w_p \left(R2^*{}_p - \widehat{\boldsymbol{b}}_{\boldsymbol{p}}^{\boldsymbol{t}} \cdot \left(\widehat{\mathfrak{R}}2^* \cdot \widehat{\boldsymbol{b}}_p \right) \right) \right\|_{\mathbf{2}}, \quad [4.9]$$

where w_p is the inverse of the magnitude of the T2*w image of the *p*-th orientation, which reflects differences in SNR in the subject as it is rotated within the coil through orientations.

4.3 Materials and Methods

4.3.1 Phantom Construction

*Geometric effects on R_2**

To examine the effects of the geometry of susceptibility sources within a voxel on R_2*, glass capillary tubes were used to construct a cylindrical sub-voxel structure of susceptibility sources placed within an agar phantom. The glass capillary tubes (category III, Fig. 4.1) contained a 5mM gadolinium solution (Magnevist, Berlex Laboratories) corresponding to a susceptibility of 1.62ppm(30). Waterproof silicone sealant was used to seal and bind the ends of the tubes. All sources were contained within a cylindrical phantom, 10cm in diameter.

Magnetic Susceptibility Anisotropy and Geometric Effects

A cylindrical phantom, 10cm in diameter, was constructed containing 1% agarose gel. Within this phantom, three susceptibility sources were placed: 1) a straight bar of 12K carbon fiber tow, which was bundle of 12,000 carbon fiber strands (ACP Composites, Livermore CA) (category I Fig. 4.1). 2) a ring of carbon fiber tow around a 50ml centrifuge tube (category I, Fig. 4.1), and 3) a mixture of finely cut, <1mm in length, but unaligned carbon fiber sections mixed with agar (category III, Fig. 4.1). Two balloons containing gadolinium solutions with concentrations, 2.5mM and 5 mM, corresponding to susceptibilities of 0.81ppm (Balloon 1) and 1.6ppm (Balloon 2) respectively, were placed within the phantom as isotropic susceptibility sources (Category IV, Fig. 4.1).

4.3.2 Data Acquisition

Phantom

All data were acquired on a General Electric (GE) 3T MRI scanner (HDx, GE Healthcare, Waukesha, WI, USA) using an eight channel head coil and a Styrofoam ball sample holder allowing reproducible rotations of the phantom. A total of 16 orientations uniformly spaced over a unit sphere were acquired for both phantoms. For the capillary tube phantom imaging parameters were as follows: multi echo gradient echo (MEGRE) acquisition, 12 echoes, TR 104.3ms, first TE 3.4ms, echo spacing 3.2 ms, flip angle 15°, bandwidth of 62.5kHz, field of view 13cm and at $1mm^3$ resolution. The carbon fiber phantom used the same imaging parameters, except for the number of echoes (10) and the TR (88.4 ms).

Volunteer

In this volunteer study, approved by our institutional review board, images were acquired with 11 echoes, first echo 2.66ms, with an echo spacing of 2.64ms, a TR of 46.9ms, flip angle 15°, field of view 24cm, band width 62.5kHz, acquisition matrix of 160x160 and isotropic resolution of $1.5mm^3$ with the MEGRE sequence used in the phantom studies. The transmit receive birdcage head coil was used in the volunteer study to allow for a greater degree of rotation. The head tilts performed by the volunteer included a combination of forward, backward, left and right leaning tilts in both supine and prone positions for a total of 12 acquired head orientations. Diffusion data was acquired with a product 2D EPI dual spin echo diffusion weighted

sequence, with resolution 2x2x2.4mm^3, parameters: 33 directions, b-value of 1000 s/mm^2, 22 cm field of view, acquisition matrix of 110x110 and 2.4 mm slice thickness, 85.3ms echo time, 17s TR and bandwidth per pixel of 1953.12Hz.

4.3.3 Tensor Reconstructions

Both R2T and STI reconstructions require registration of the magnitude and phase images to the neutral subject orientation. Affine rigid image registration was performed with FSL(65-67). A B_0 map was derived from the multiple echo data which allowed to correct for B_0 distortion of the diffusion weighted images using FUGUE (65,66). Diffusion tensor data was reconstructed using FSL. A conjugate gradient solver was used to fit the measured multiple orientation phase data against the model described in the theory, eq. 4.5 to estimate the STI.

The R2T reconstruction was constructed by first computing the apparent scalar relaxation $R2^*_{app}$ in each of the acquired orientations using a robust estimation of mono-exponential decay (68). Noise correction was performed to account for bias in the reconstructed exponential decay due to the presence of Rician noise in the magnitude signal implemented as a look up table (69). Next, a rank 2 tensor R2T was fitting to the obtained R2* values using a conjugate gradient solver. The solution for STI was computed as described previously, with a conjugate gradient solver (62).

4.3.4 Data Analysis

Singular value decomposition was performed to examine the reconstructed eigenvectors and eigenvalues from STI and R2T tensors. The tensor anisotropy (TA)

was defined as $TA = \lambda_1 - \lambda_3$, where the tensor eigenvalues λ_i i =1,2,3 are in descending order. Phantom eigenvectors are displayed weighted by the mean R2T to highlight regions with high susceptibility. In volunteer data tensor eigenvectors are presented weighted by the fractional anisotropy computed from DTI data to highlight white matter. White matter regions measured in the volunteer were: the splenium of the corpus callosum (SCC) and optic radiations (OR). Periventricular veins (PVVs) were also measured as they represent regions in the human body with cylindrical structure but without molecular order. Regions of interest (ROI) were defined manually on the magnitude images for phantoms and volunteer studies. Mean and standard deviation of ROI measurements were reported.

Alignment of eigenvectors of the various tensors was assessed through the correlation of eigenvectors defined as $C = |\mathbf{V}_a \cdot \mathbf{V}_b|$, where $\mathbf{V}_a$ and $\mathbf{V}_b$ are the normalized principal eigenvectors estimated from STI, DTI or R2T. When measuring the correlation in the alignment of the orientation of PVVs in the volunteer study, the orientation of veins was estimated manually from a straight segment of the vein visible on the magnitude of the MEGRE image. A wild bootstrap analysis was performed to compute 95% confidence intervals for the estimated tensor eigenvectors for both R2T and STI in phantom and human data 1000 iterations were computed for phantoms and human R2T and 350 iterations for human STI reconstruction. Fewer iterations for volunteer STI were computed due to time restrictions; approximately 30min.

Wild bootstrapping is a non-parametric statistical analysis method that permits inference on model parameters from data with multiple measurements; DTI studies

have used this to assess confidence in estimates of tensor parameters, anisotropy and reconstructed eigenvectors (70,71). This analysis was chosen for its ability to make inferences on systems with heteroscedastic noise (72), since the noise in phase and apparent R2* is not uniform across the imaged volume or the acquired orientations due to variations in signal sensitivity across the volume and orientations. The formulation of the bootstrap iteration is simple for the two systems under investigation in this work, Eq. 4.5 and 6 For STI and R2T respectively. In the R2T the observed relaxation rate from each orientation is considered to be an unbiased estimate of the R2* decay rate after the correction for Rician noise in the magnitude data. In the wild bootstrap analysis, the data is resampled by constructing *N* bootstrap samples $R_{2app,i}$ based on the fitted R2T, $\hat{\mathbf{R}}_2^*$:

$$R_{2app,i} = \hat{\mathbf{b}} \cdot (\hat{\mathbf{R}}_2^* \cdot \hat{\mathbf{b}}) + \boldsymbol{\varepsilon}_i . \qquad [4.10]$$

Here, ε_i is defined as $\boldsymbol{\varepsilon}_i = a\hat{\mathbf{u}}\mathbf{F}_i$, where a is the number of degrees of freedom (equal to $a = \sqrt{n/(n-k)}$, n is the number of observations and k is the number of parameters), $\mathbf{F}_i$ is a random vector defined as:

$$\mathbf{F}_i = \begin{cases} -1, \mathrm{p} < 0.5 \\ 1, \mathrm{p} \geq 0.5 \end{cases}, \qquad [4.11]$$

where p is drawn from a uniform distribution on the unit interval [0,1], and the vector $\hat{\mathbf{u}}$ is the residual of the fit of the system with the acquired data,

$$\hat{\mathbf{u}} = R_{2app} - \hat{\mathbf{b}} \cdot (\hat{\mathbf{R}}_2^* \cdot \hat{\mathbf{b}}). \quad [4.12]$$

For every bootstrap sample $R_{2app,i}$, a new tensor $\hat{\mathbf{R}}_{2,i}^*$ is estimated. Similarly, the definition of the STI bootstrap sample is:

$$\mathbf{b}_i = \mathbf{D}\hat{\mathbf{X}} + \boldsymbol{\varepsilon}_i \quad [4.13]$$

Here $\boldsymbol{\varepsilon}_i$ has the same formal definition as for the R2*T problem with $\hat{\mathbf{u}}$ now the residual of the fit of the local phase data with the susceptibility tensor model. **D** is the susceptibility tensor kernel defined in k-space (Eq. 4.5) in matrix notation.

Confidence intervals were constructed from the distribution of estimated parameters from the bootstrapped iterations, 95% confidence intervals were constructed from the 2.5 and 97.5 percentiles. Statistical evaluation of eigenvectors requires additional considerations due to the inherent ambiguity in the definition of the principal eigenvector, where both an eigenvector and its anti-parallel equivalent describes the axis of the tensor equally well and the arithmetic mean is not applicable. Robust statistics of the mean dyadic tensor of a region of interest have been demonstrated in analysis of diffusion tensor imaging previously and defined as follows (71,73). The 95th percentile of the angle between the principal eigenvector of the mean dyadic tensor and the eigenvector for each bootstrap iteration defines the half angle of the cone of the 95% confidence interval surrounding the mean principal direction of the tensor. The 95% confidence interval was calculated for both phantom and human data. The mean dyadic tensor is:

$$\left\langle \varepsilon_l^j \varepsilon_l^{jT} \right\rangle = \left\langle \begin{bmatrix} \left(\varepsilon_{lX}^j\right)^2 & \varepsilon_{lX}^j \varepsilon_{lY}^j & \varepsilon_{lX}^j \varepsilon_{lZ}^j \\ \varepsilon_{lX}^j \varepsilon_{lY}^j & \left(\varepsilon_{lY}^j\right)^2 & \varepsilon_{lY}^j \varepsilon_{lZ}^j \\ \varepsilon_{lX}^j \varepsilon_{lZ}^j & \varepsilon_{lY}^j \varepsilon_{lZ}^j & \left(\varepsilon_{lZ}^j\right)^2 \end{bmatrix} \right\rangle = \frac{1}{N} \sum_{j=1}^{N} \varepsilon_l^j \varepsilon_l^{jT} \qquad [4.14]$$

Where ε_l^j is the l^{th} eigenvector from the j^{th} iteration, from a total of N bootstrap iterations.

4.4 Results

4.4.1 Phantom experiments

The mean susceptibility of the capillary tube bundle was 0.15±0.10ppm (Table 1). The mean susceptibility of the glass tubes was paramagnetic, consistent with the susceptibility of the Gadolinium solution.

Table 4.1: Tensor properties and correlation of STI and R2T in phantom sources.

		STI		**R2T**	
	$\lvert V_{R2*} \cdot V_{STI} \rvert$	Mean (ppm)	Anisotropy (ppm)	Mean (Hz)	Anisotropy (Hz)
Bar	0.98±0.02	-0.26± 0.05	0.55±0.17	73±8	101±13
Ring	0.97±0.06	-0.12±0.05	0.34±0.08	50±15	85±29
Tubes	0.30±0.25	0.15±0.10	0.44±0.19	61±12	87±20
Bits	0.45±0.28	0.08±0.07	0.18±0.07	50±14	26±14
Balloon 1	0.46±0.27	0.71±0.03	0.22±0.08	13±0.40	2.71±1.4
Balloon 2	0.47±0.27	1.33±0.06	0.50±0.18	27±0.83	4.20±2.1

A higher correlation between R2T and STI was found for the molecularly ordered carbon fiber phantoms (Bar: 0.98 ±0.02, Ring: 0.97±0.06) than for the capillary tube (0.30±0.25), and low correlation was also found for the gadolinium balloons (Balloon 1: 0.46±0.27 Balloon 2: 0.47±0.27), Table 1. Fig. 4.2 shows this effect in row 5; there was high correlation in eigenvectors within the carbon fiber ring and the subsequent decrease in alignment in the remaining cases, capillary tubes (II), carbon fiber bits (III) and gadolinium balloons (IV). There is a consistent direction in capillary tubes only in R2T, fourth row Fig. 4.2. Lastly, there is no clear STI or R2T direction in the balloons, column IV Fig. 4.2.

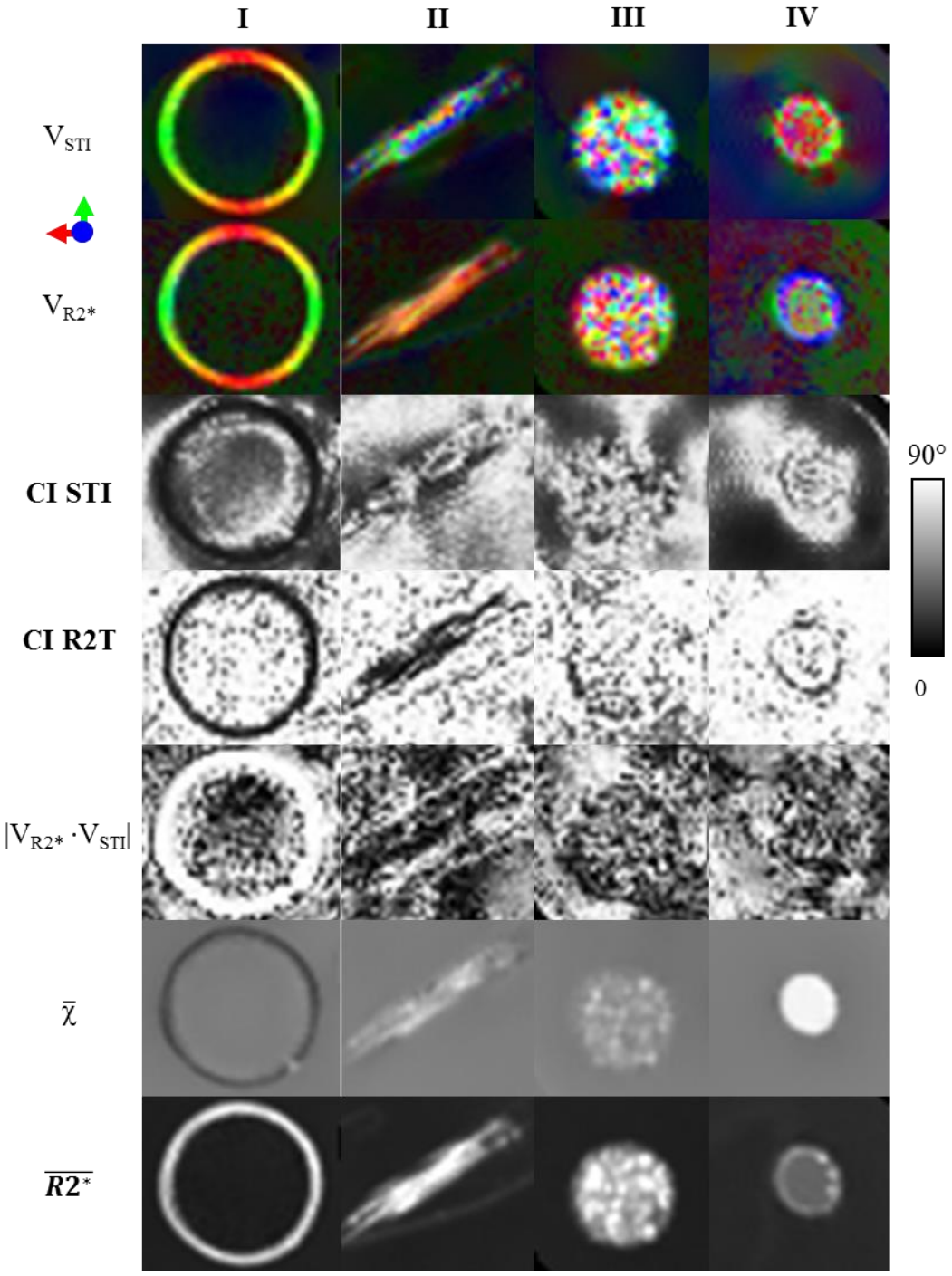

Figure 4.2: Phantom results demonstrating 4 categories listed in Fig. 4.1 in each column. Eigenvectors from STI and R2T weighted by the mean R2T (first two rows), the 95% confidence interval from STI and R2T (rows 3 and 4), the absolute value of the product between the two vectors VSTI and VR2T(row 5, W =0-1) and the mean STI and R2T (row 6 (W=-0.4-0.4ppm(columns I-III) and W=-1.5-1.5ppm

Fig. 4.3 shows the confidence for all eigenvectors for cases I - IV. For intact carbon fiber sources (Ring and Bar) the confidence in the direction of the fiber axis in R2T and STI is greater (narrower confidence interval) than the remaining eigenvectors, Fig 4.3; (Ring: STI EV1:15°±11° EV2: 41°±21°, EV3: 38°±22°, R2T EV1: 61°±26, EV2:62°±26°, EV3: 18°±3°; Bar STI EV1: 11°±5°, 29°±16°, 28°±16°, R2T 68°±23°, 68°±23° EV3: 9°±3°). Whereas the confidence of the vector direction is only consistently narrow for R2T in the capillary tubes, (R2T EV1: 65°±25°, EV2: 67°±24°, EV3: 20°±21° compared to STI: EV1 47°±22, EV2: 55°±21°, EV3 35°±22°). Only low confidence (wide confidence intervals) were observed for both STI and R2T in the gadolinium balloons (Balloon 1 STI: EV1 67°±16°, EV2 73°±12°, EV3 47°±21°; R2T: EV1: 81°±14°, EV2 88°±6°, EV3: 81°±15°).

\

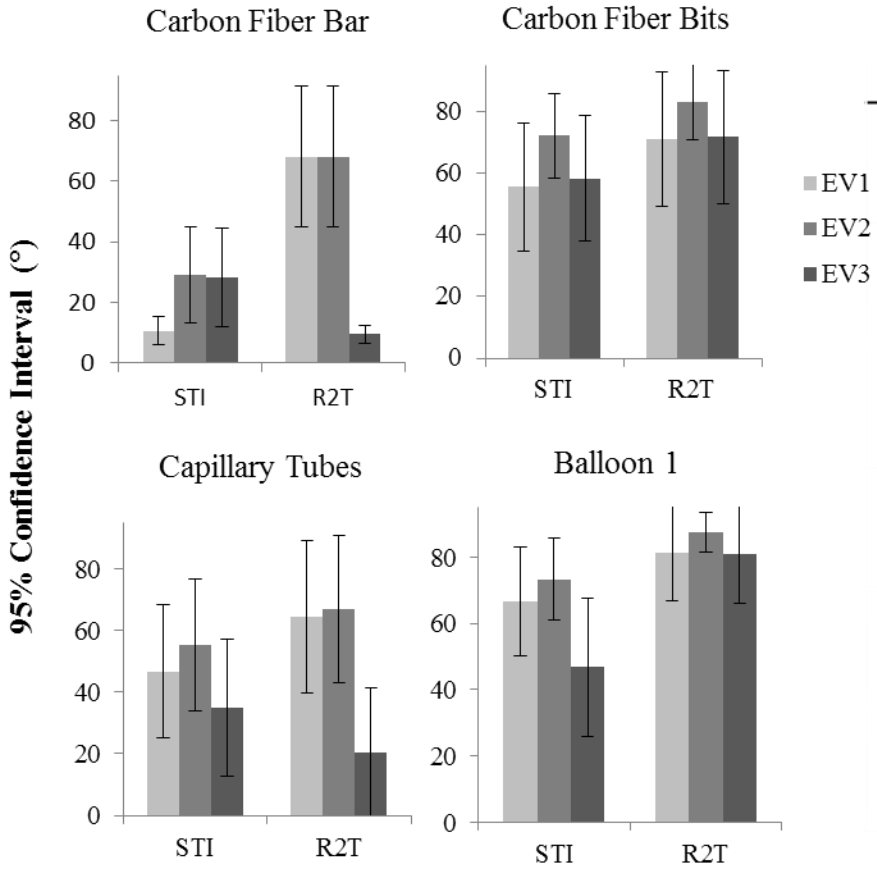

95% Confidence Interval (°)

		STI	R2T
Tubes	EV1	47±22	65±25
	EV2	55±21	67±24
	EV3	35±22	20±21
CF Bar	EV1	11±5	68±23
	EV2	29±16	68±23
	EV3	28±16	9±3
CF Ring	EV1	15±11	61±26
	EV2	41±21	62±26
	EV3	38±22	18±15
CF Bits	EV1	56±21	71±22
	EV2	72±14	83±12
	EV3	58±20	72±22
Balloon 1	EV1	67±16	81±14
	EV2	73±12	88±6
	EV3	47±21	81±15
Balloon 2	EV1	56±21	79±18
	EV2	64±18	85±12
	EV3	38±22	76±20

Figure 4.3 Confidence intervals of all eigenvectors for STI and R2T from the phantom data. Cylindrical symmetry is observed in the confidence intervals from the carbon fiber bar and ring sources and capillary tubes.

4.4.2 Human Study

Fig. 4.4 shows correlation between eigenvectors in vivo, areas of high correlation were found between R2T and STI particularly within the major white matter tracts (SCC: 0.72±0.27, OR: 0.69±0.27). High correlation was also found between R2T and DTI (SCC: 0.76±0.22, OR: 0.86±0.17) between STI and DTI (SCC:0.68±0.23, OR: 0.68±0.20).

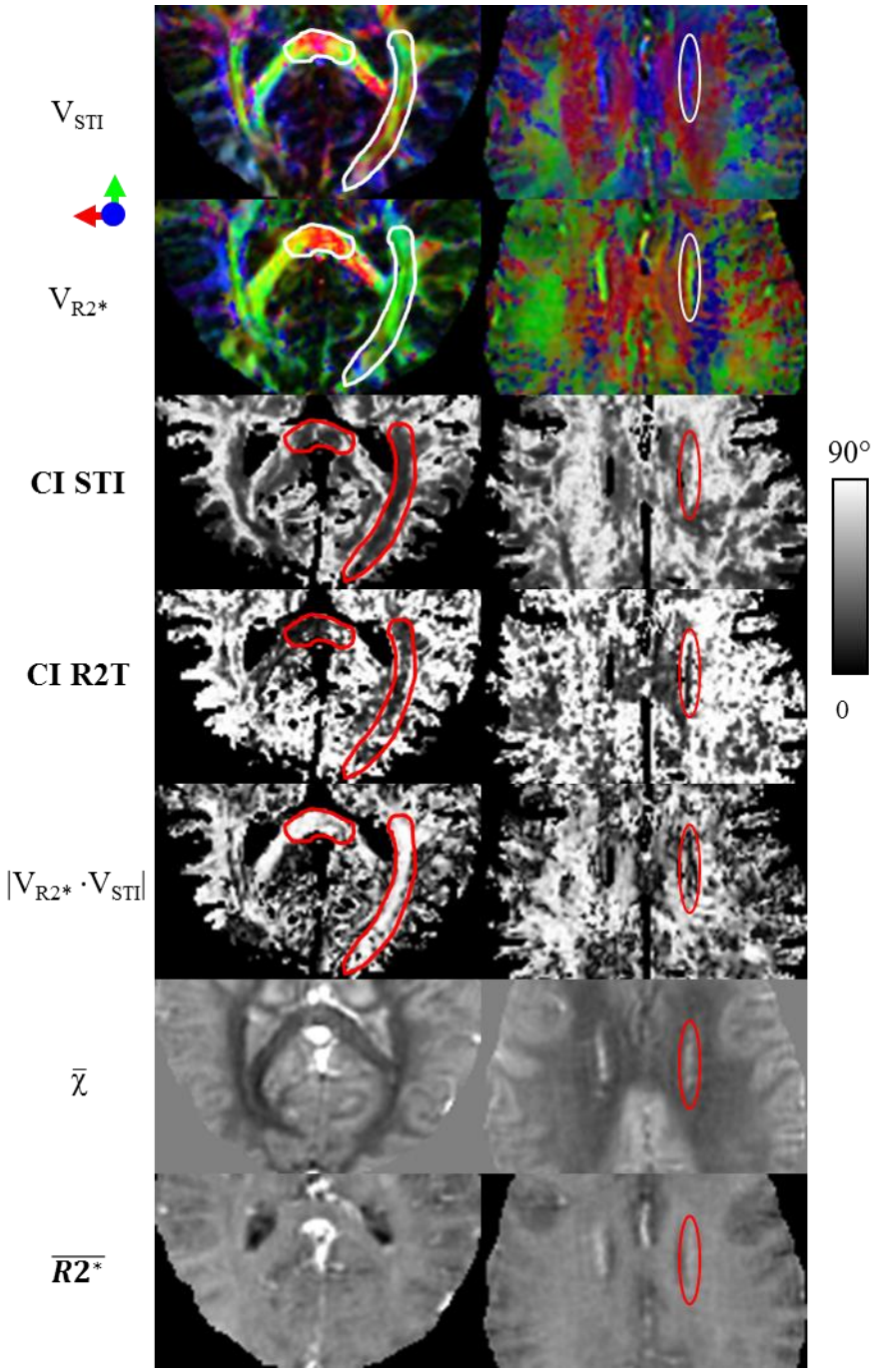

Figure 4.4: Principal eigenvectors V_{STI} and V_{R2T} within the SCC and OR (left column) and periventricular veins(right column) (rows 1 and 2),the confidence interval from STI and R2T (rows 3 and 4), correlation between V_{STI} and V_{R2*} (row 5 W=0-1) and the mean STI and R2T (rows 6 W = -70-70ppb and 7 W=0-40Hz).V_{STI} and V_{R2*} are weighted by DTI FA on the left to highlight white matter and by R2* from a single orientation to highlight veins on the right.

In Fig. 4.4 the confidence intervals for the principal STI and R2T eigenvectors for a slice through the corpus callosum are narrower in the fiber direction, but there is less confidence overall in the periphery of the brain where fibers cross and tracts meet. Values for anisotropy were consistent with previous literature were observed in R2T : SCC: 14±5.5 Hz; OR: 16±5.5 Hz and STI : SCC: 52±23ppb, OR: 54±17ppb.

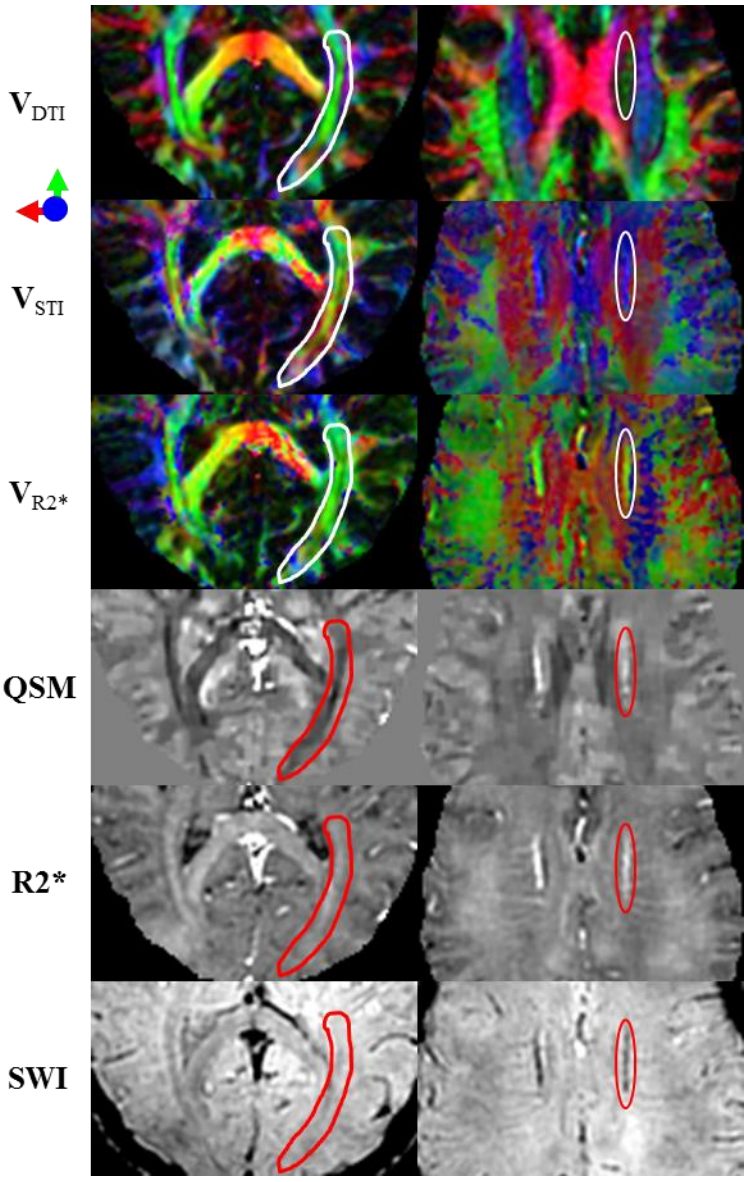

Figure 4.5: V_{DTI}, V_{STI} and V_{R2T} weighted by DTI FA rows are weighted by DTI FA on the left to highlight white matter and by R2* from a single orientation to highlight veins on the right, QSM from a single orientation (row 4; W -70-70ppb), R2* from a single orientation (row 5; W =0-40Hz) and SWI (row 6). The white matter displays orientation dependence within a single orientation, V_{R2T} display contrast between periventricular veins with surrounding white matter (circled is a large vein) consistent with the presence of veins on single orientation measurements. V_{STI} and V_{R2*}.

Fig. 4.5 demonstrates the sensitivity of relaxation and susceptibility measurements to white matter fiber architecture and the presence of periventricular

veins, the box in the left column shows orientation dependent relaxation and susceptibility from a single orientation reflective of white matter fiber orientation.

4.4.3 Tensor Properties of Veins

The vector maps in right column of Fig. 4.5 shows contrast in V_{R2*} present between the veins and surrounding white matter, the presence of these veins are demonstrated with QSM, R2* and SWI from a single orientation. The correlation between eigenvectors of 21 measured veins was 0.67 ± 0.12 between R2T and manual measurements of the vessel direction. In the larger A-P oriented veins, outlined on Fig.4.4 and Fig. 4.5, the correlation was higher, R2T versus the measured direction (V_M): left vein: 0.87±0.1, right: 0.83±0.24. Similarly there was generally greater confidence in V_{R2*} than in V_{STI}, left vein R2T EV1: 67°±19°, EV2: 68°±19°, EV3: 23°±14° vs STI: EV1: 41°±11°, EV2: 47°±13°, EV3: 35°±12°; right vein R2T: EV1: 73°±24°, EV2: 77°±21°, EV3: 48°±19° vs STI: EV1:64°±16°, EV2: 69°±16°, EV3: 47°±24°.

4.5 Discussion

In this work, we investigate orientation dependent R2* and susceptibility measurements in the brain reflective of tissue microstructure and molecular organization. R2* is related to dependence of field inhomogeneity primarily from tissue microstructure, and susceptibility is influenced by the presence of both tissue microstructure and molecular organization. Phantom experiments demonstrate that

both molecular anisotropy and microstructure results in R2* and susceptibility tensor anisotropy, while microstructure alone without molecular anisotropy leads to R2* anisotropy only. This was demonstrated in vivo by examining the structure of major white matter tracts and periventricular veins.

The carbon fiber phantom represented where both sub-voxel structure and intrinsic molecular organization is present. R2T and STI eigenvectors were highly correlated (Fig. 2 (I) and Table 1). The reported measures of anisotropy are within the range of previous measurements of properties of carbon fiber (50). In capillary tubes the R2T and STI eigenvectors were much less correlated, Fig. 2 (II) and Table 1; microstructure is present without molecular order. In both categories III and IV in the carbon fiber bits and gadolinium balloons, wider confidence intervals were observed for both STI and R2T, Fig. 2. Correlation between eigenvectors clearly demonstrated the presence R2T and STI in carbon fiber and R2T but not STI anisotropy in capillary tubes.

Estimated confidence intervals corroborated the measurements of correlation in the estimated fiber directions in phantom studies. The axis of the fiber was reconstructed with greater confidence compared to the remaining eigenvectors, Fig. 3; whereas wider confidence intervals were observed for the minor tensor axes. This symmetry is consistent with the known cylindrical architecture of carbon fiber and the capillary tubes. The STI reconstruction in the capillary tubes showed no clear symmetry, evidenced in the large overlap of the confidence intervals Fig, 3. In contrast, R2T showed a clear symmetry in the capillary tubes.

Applying the same analysis to the in vivo data, white matter shows increased correlation between R2T and STI, similar to the correlation observed for STI or R2T with DTI; consistent with both microstructure and molecular order. The appearance of PVVs is most obvious on V_{R2*}, Fig. 4, whereas there is very little contrast between the PVVs and the surrounding white matter in V_{STI}. More importantly, R2T had much higher confidence than STI in the PVVs, which also correlated with the measured venous direction. Similar to what was observed in the phantom for structured materials, the confidence intervals in the major fiber tracts in STI and R2T had the greatest confidence in the principal eigenvectors, but only in R2T for the PVVs, Fig. 3.

There are a number of challenges in computing the R2T and STI maps. First, only a limited number of orientations can be performed in vivo in a very motivated subject with a long scan time. Limited orientations induced error in the reconstructed tensors, as demonstrated by the wide confidence interval in the wild bootstrap method for certain fiber tracts such as the centrum semiovale (CS) along the superior inferior axis as previously observed (62). A second challenge is the potential for mis-registration between volumes at different orientations. Changes in partial volume effects between different orientations can lead to artificial increases in the anisotropy at tissue borders in R2T. Finally, large variations in the background field can lead to increases in the measured R2* independent of the local tissue structure. However, in this work, the areas of interest were limited to white matter tracts near the center of the brain where the background field is more homogeneous.

4.6 Conclusion

Here voxels containing micro-structure and molecular organization (category I) were observed in carbon fiber and white matter in the alignment of R2T and STI reconstructions. A lack of susceptibility anisotropy was observed sources without molecular order (category III); such as the capillary tubes. Wild Bootstrapping analysis showed the stability in the reconstructed fiber directions from R2T and STI in vivo in major white matter tracts. Confidence interval corroborated our observations of overlap between measured eigenvectors in R2T and STI and provided insight on the influence of noise on the reconstructed tensors. This critical evaluation of the structure of the orientation dependent R2T and STI were reflective of voxel architecture and organization in the brain.

CHAPTER 5

5 QUANTITATIVE SUSCEPTIBILITY MAPPING (QSM) OF WHITE MATTER MULTIPLE SCLEROSIS LESIONS: INTERPRETING POSITIVE SUSCEPTIBILITY AND THE PRESENCE OF IRON

Within multiple sclerosis (MS) lesions iron is present in chronically activated microglia. Thus, iron detection with MRI might provide a biomarker for chronic inflammation within lesions. Here, we examine contributions of iron and myelin to magnetic susceptibility of lesions on quantitative susceptibility mapping (QSM). Fixed MS brain tissue was assessed with MRI including gradient echo data, which was processed to generate field (phase), R2* and QSM. Five lesions were sectioned and evaluated by immunohistochemistry for presence of myelin, iron and microglia/macrophages. Two of the lesions had an elemental analysis for iron concentration mapping, and their phospholipid content was estimated from the difference in the iron and QSM data. Three of the five lesions had substantial iron deposition that was associated with microglia and positive susceptibility values. For the two lesions with elemental analysis, the QSM derived phospholipid content maps were consistent with myelin labeled histology. Positive susceptibility values with respect to water indicate the presence of iron in MS lesions, though both demyelination and iron deposition contribute to QSM.

5.1 Introduction

Recent work on multiple sclerosis (MS) with MRI has detected dynamic

changes in magnetic susceptibility (74) and MRI phase (75) that reflect active demyelination and iron deposition in lesions. Iron retained by activated microglia/macrophages in MS lesions (76-78) may serve as a marker of innate immune system activation. Activated microglia are typically present at the vicinity of chronic active MS lesions and are the predominant source of iron within lesions(77,79,80). MRI and histological studies of iron report significant changes of iron content during lesion development from active demyelination to chronic inflammation and chronic inactivity (76,77,80,81).

Phase imaging and R2* mapping in MRI have been explored to assess lesion iron content qualitatively (76,77,79) and quantitatively (82,83). However, there are many confounding factors associated with R2* and phase imaging including dependence on orientation, field strength and distribution of susceptibility sources (60,84). These factors influence the heterogeneity of the field and subsequently the R2*(2,64). Particularly for MS lesion studies, magnetic susceptibility sources outside a lesion can also generate fields inside the lesion and hence contribute to R2* and phase of the lesion. These effects must be considered as well when interpreting the R2* or phase in order to investigate iron specific to MS lesions.

The tissue field derived from phase data can be deconvolved to generate quantitative susceptibility mapping (QSM) that reflects local tissue property (33,43,85), offering an alternative means to process gradient echo data. QSM can measure magnetic sources in tissue including iron, myelin and calcification that are present in normal and diseased brain tissue (58,74,86-89). A susceptibility tensor

(6,90) can be used to model susceptibility anisotropy observed in ordered myelin that induces orientation dependence of R2*(13), phase (91,92) and apparent susceptibility(6,17,48,62,93). Both myelin and iron contribute significantly to the QSM value in white matter. The connection between QSM and iron content remains to be established for MS lesions.

The susceptibility of myelin is negative with respect to water. Therefore, severe or complete demyelination can increase susceptibility up to zero; when water is the reference. Positive susceptibility values must include contributions from paramagnetic material, which is iron in MS lesion. Here we propose to use an elemental measurement, laser ablation inductively coupled plasma mass spectrometry (LA-ICP-MS), to quantify the iron content of MS lesions in brain specimens. Histology and standard T2 weighted imaging (T2w) are compared with QSM to inform the interpretation of iron content within MS lesions.

5.2 Theory

5.2.1 Mean Susceptibility Estimation from COSMOS and the Susceptibility Tensor Trace

COSMOS estimates the orientation independent component of the magnetic susceptibility; the mean magnetic susceptibility, MMS. Here we discuss how the COSMOS problem is equivalent to the estimation of the trace of the susceptibility tensor, $\bar{\chi} = Tr(\chi)/3$, and *Tr* is the tensor trace, under the condition of uniform sampling of orientations over a unit sphere. For a single voxel image, for simplicity, the elements of the vector $\mathbf{b}_{cosmos}$, describing the vector of field shifts for all

orientations in the COSMOS problem is described as:

$$b_{cosmos,i} = D_i \bar{X}\,, \qquad [5.1]$$

where D_i is the scalar dipole kernel in k-space and $b_{cosmos,i}$ is the measured field at orientation *i* and $\bar{X}$ is the Fourier transform of $\bar{\chi}$. Similarly the field shifts from the susceptibility tensor problem are:

$$b_{sti,i} = \mathbf{T} \cdot \mathbf{R}_i^T \mathbf{X} \mathbf{R}_i \qquad [5.2]$$

Where **T** is the susceptibility tensor kernel, **X** is the general susceptibility tensor and $\cdot$ is the scalar product and $\mathbf{R}_i$ is the rotation of the object to a new orientation, *i*. Though typically estimated in the subject frame the tensor kernel with respect to the laboratory frame; the scanner coordinate system is the frame of reference and the subject rotates in the field,

$$\mathbf{T} = \left[\frac{\hat{\mathbf{H}}_0 \times \hat{\mathbf{H}}_0}{3} - \mathbf{k} \cdot \hat{\mathbf{H}}_0 \frac{\hat{\mathbf{H}}_0 \times \mathbf{k}}{k^2} \right] \qquad [5.3]$$

comes from the definition of the susceptibility tensor problem(6), $\hat{\mathbf{H}}_0$ is the main magnetic field direction, **k** is the k-space vector and $\times$ is the cross product. The general susceptibility tensor can be written as a sum of two tensors, $\boldsymbol{\chi} = \mathbf{I}\bar{\chi} + \boldsymbol{\chi}_a$, $\bar{\chi}$ is defined as the sum of the susceptibility tensor trace, $\bar{\chi} = Tr(\boldsymbol{\chi})/3$, and tensor anisotropy, $\boldsymbol{\chi}_a = \boldsymbol{\chi} - \mathbf{I}\bar{\chi}$, such that $Tr(\boldsymbol{\chi}_a) = 0$ and the isotropic susceptibility, $\mathbf{I}\bar{\chi}$, is independent of the anisotropic component, $\mathbf{I}\bar{\chi} \cdot \boldsymbol{\chi}_a = 0$. The tensor problem can be

rewritten:

$$\mathbf{b}_{sti,i} = \mathbf{T}_i \cdot \mathbf{R}_i^T \mathbf{X} \mathbf{R}_i = \mathbf{T}_i \cdot \mathbf{R}_i^T \mathbf{I}\overline{X} \mathbf{R}_i + \mathbf{T}_i \cdot \mathbf{R}_i^T \mathbf{X}_a \mathbf{R}_i \quad [5.4]$$

The $\mathbf{I}\overline{X}$ term can be shown to reduce to the COSMOS problem. As long as the fields from $\mathbf{X}_a$, $\mathbf{b}_{\mathbf{X}_a}$, are orthogonal to the fields from $\mathbf{I}\overline{X}$, $\mathbf{b}_{\overline{X}}$, the COSMOS solution from the field generated by an arbitrary tensor will contain only the isotropic component of the susceptibility tensor; field from the anisotropy of the tensor will not fit the isotropic model. The solution of the tensor problem is the sum of the two fields, $\mathbf{b}_{\overline{X}}$ and $\mathbf{b}_{\mathbf{X}_a}$, the scalar product of which is $\mathbf{b}_{\overline{X}} \cdot \mathbf{b}_{\mathbf{X}_a} = \sum_i (\mathbf{T} \cdot (\mathbf{R}_i^T \mathbf{I}\overline{X} \mathbf{R}_i))(\mathbf{T} \cdot (\mathbf{R}_i^T \mathbf{X}_a \mathbf{R}_i))$.

The $\mathbf{I}\overline{X}$ term is constant over any $\mathbf{R}_i$, $\mathbf{R}_i^T \mathbf{I}\overline{X} \mathbf{R}_i = \mathbf{I}\overline{X}$ and $\mathbf{T}$ is constant over orientation, which can be removed from the sum as, $\mathbf{b}_{\overline{X}} \cdot \mathbf{b}_{\mathbf{X}_a} = \mathbf{T} \cdot (\mathbf{R}_i^T \mathbf{I}\overline{X} \mathbf{R}_i) \mathbf{T} \cdot \sum_i \mathbf{R}_i^T \mathbf{X}_a \mathbf{R}_i$. As long as $\mathbf{R}_i$ spans all rotations in 3D space, it follows from Schur's lemma in group theory(94) that this term $\mathbf{R}_i^T \mathbf{X}_a \mathbf{R}_i$ is a scalar, where

$\mathbf{R}_i^T \boldsymbol{\chi}_a \mathbf{R}_i = \mathbf{I} Tr(\mathbf{R}_i^T \boldsymbol{\chi}_a \mathbf{R}_i) = \mathbf{I} Tr(\boldsymbol{\chi}_a) = 0$ and so $\mathbf{b}_{\overline{X}} \cdot \mathbf{b}_{\mathbf{X}_a} = (\mathbf{T} \cdot \mathbf{I}\overline{X}) \mathbf{T} \cdot \sum_i (\mathbf{R}_i^T \mathbf{X}_a \mathbf{R}_i) = 0$.

Here the vector spaces spanned by $\overline{X}$ and $\mathbf{X}_a$ are orthogonal. The COSMOS solution is $Tr(\boldsymbol{\chi})/3$ as long as the orientations are sampled uniformly over a sphere. This condition is necessary in order to achieve a non-biased estimate of all susceptibility tensor components and achievable in phantom data (6,62).

Here we propose to use an elemental measurement, laser ablation inductively

coupled mass spectrometry (LA-ICP-MS), to quantify the iron content of MS lesion in brain specimens. The susceptibility contribution from the measured iron content and QSM were used to quantify myelin content. Histology and standard T2 weighted imaging (T2w) are compared with QSM to inform the interpretation of iron content within MS lesions.

5.3 Methods and Materials

5.3.1 MS brain section preparation

Human CNS tissue was obtained at autopsy of 1 MS subject (male, age 68, chronic MS, not treated with any disease-modifying treatment; cause of death: cardiac arrhythmia) according to an institutional Review Board-approved protocol. Seven 1 cm thick formalin fixed coronal MS brain specimens were imbedded in 1% agar for stabilization during MRI imaging.

5.3.2 Histology and LA-ICP-MS

Fixed tissue was transferred through sucrose, frozen in dry ice and *N*-methylbutane, and cut at 10 and 50μm thicknesses (79). For immunohistochemical labeling, 10 um sections were incubated with primary antibody against myelin basic protein (polyclonal rabbit) and CD68 (monoclonal mouse IgG; both Dako) and processed with the appropriate biotinylated secondary antibody and avidin-biotin staining kit with diaminobenzidine as chromogen (Vector Laboratories Inc., CA) , for Perl's stain sections, were treated in 10% formalin and then hydrated in distilled water, incubated in 5%potassium ferrocyanide with 10%Hydrochloric Acid solution in room temperature for 1.5hr and then microwaved. Sections were counterstained with

hematoxylin.

Iron concentration, [Fe], maps were generated from LA-ICP-MS data with 106x250x50um^3 resolution for lesion 1 and 106x110x50um^3 resolution for lesion 2 across 50-micron sections. Lesion 1 was measured with a New Wave UP193HE laser ablation system (193 nm excimer laser), fired at 10 Hz with a 250 μm ablation spot diameter with a fluence of 0.3 J/cm^2 and a stage movement rate of 100 μm/s for each line. Lesion 2 was measured with a New Wave NWR 213 laser ablation system (213 nm frequency quintupled Nd:YAG laser, fired at 20 Hz using a 110 μm ablation spot diameter with a fluence of 0.4 J/cm^2 and a stage movement rate of 200 μm/s for each line. Ablated material carried to a ThermoFinnigan Element 2 Inductively Coupled Plasma Sector Field Mass Spectrometer (flow of He (0.8 L/min)) with a resolving power (m/Δm) of 4000. Gelatin, with known concentrations of Fe, was measured before and after each line.

5.3.3 MRI Data

Sixteen orientations evenly distributed over a sphere on a GE 3T scanner were acquired using a 3D gradient echo (GRE) sequence in oblique planes with the following imaging parameters: 53.8ms TR, first echo 4.05ms, 4.15ms echo spacing, 12 acquired echoes at a resolution of 0.7x0.7x0.7mm^3, flip angle of 20° and bandwidth of 62.5kHz. A 32 channel receive coil was used to image the slab containing Lesion 1 and a 12 channel head coil was used to image all other slabs. For Lesion 1, T2w images were acquired with a 3D fast spin echo sequence with parameters: resolution, 0.332x0.332x2mm^3, TE 84.34ms, TR 1.067s, echo train length 48, field of view 17cm,

acceleration factor 2 and a bandwidth of 100kHz. For all other lesions, T2w images were acquired with the same sequence, but parameters; acquired resolution $0.75x0.75x1.2mm^3$, Echo time 103.3ms, Echo train length 140, repetition time 2.5s, field of view 24cm, bandwidth 125kHz.

5.3.4 Data Analysis

MRI to Histology Registration

2D LA-ICP-MS [Fe] maps and histological images were manually aligned to form a 3D volume; slices were distributed in the volume according to their relative location cut from the surface of the slab. A non-rigid 3D affine registration of the histology and QSM images was calculated from corresponding fiducial markers placed within and around the lesion. MRI images were linearly interpolated to the resolution of the LA-ICP-MS [Fe] maps.

MRI Data Analysis

The total field was estimated from a fit of the complex signal evolution (57). Background field subtraction was performed using projection of dipole fields, PDF(95). Mono-exponential R2* was estimated with linear least squares estimation of the logarithm transformed multi-echo GRE data. Rigid linear registration of GRE orientations was performed with FLIRT and tri-linear interpolation (65-67). Multiple orientation reconstruction of QSM (COSMOS-QSM) from the tissue fields was calculated with COSMOS (43), Single-orientation morphology enabled dipole inversion QSM, (MEDI-QSM) (57) was reconstructed for each of the 16 orientations.

The reference susceptibility in all the QSMs was set to agar. Susceptibility tensor imaging, STI, reconstruction was performed with a conjugate gradient solver of the tissue field to source inverse problem (6). The fractional anisotropy, FA, of the STI of the slabs was estimated from a least squares fit of the definition of FA from diffusion tensor imaging(7),

$$\sqrt{\sum_i \lambda_i^{\,2}}\, FA = \sqrt{3/2}\sqrt{\sum_i (\lambda_i - \bar{\lambda})^2}\ . \qquad [5.5]$$

Where λ_i, i =1,2,3, are the eigenvalues of the tensor ordered from greatest to least in signed value and $\bar{\lambda} = (\lambda_1 + \lambda_2 + \lambda_3)/3$ is the normalized tensor trace, STI-Trace. R2* was estimated from a linear fit of the signal evolution in log space.

Segmentations of lesions were generated with a grayscale threshold chosen by selecting the half-maximum of the lesion edge along 20 profiles radially through the lesion edge on QSM and T2w images interpolated to eight times the GRE resolution to better define the edge; the mean volume detected from all of the half maximum thresholds is reported.

5.3.5 Susceptibility Contribution from Iron

Perl's staining is sensitive to Fe3+ in ferritin. LA-ICP-MS measures all iron forms including those in ferritin, oxyhemoglobin and deoxyhemoglobin. QSM is predominantly affected by paramagnetic iron, Fe3+ in ferritin and Fe2+ in deoxyhemoglobin. In the MS lesions, in vitro experiments show mostly ferritin in microglia (77). Therefore, [Fe] maps were converted to susceptibility with an estimate

of the molar susceptibility of iron at room temperature like ferritin; 3.78 effective Bohr magnetons (96,97) and a brain tissue density of 1.04g/cm^3(98). Using the Langevin equation, iron contributes, $\chi_{[Fe]}$=1.4ppb*[Fe], where [Fe] is in mg/kg. The myelin related susceptibility was calculated as χ_{Myelin} = QSM – 1.4ppb *[Fe], considering that myelin is a major susceptibility component in white matter (40,87,99).

5.3.6 Myelin Quantification from χ_{Myelin}

The susceptibility contribution from myelin was estimated using the magnetic properties of phospholipids. First the magnetic anisotropy was used to estimate the myelin content of NAWM and the mean molar susceptibility of myelin. The mean molar susceptibility was needed to assess myelin content independent of the tissue microstructure from the STI trace. In the brain, phospholipids are organized within myelin sheaths and the anisotropy observed in MRI is from the ensemble average(17,48,62,90). Lounila measured volume susceptibility anisotropy of phospholipids of -0.223ppm (28). Assuming the commonly used average molecular mass of 775g/mol (100) for phospholipids and a density of 0.25g/cm^3(101), yields a molar susceptibility anisotropy, $\Delta\chi_{PL}$, contribution of -690ppb(L/mol) for a mole of organized lipids.

The average anisotropy observed with cylindrical symmetry expected in NAWM will have susceptibility anisotropy related to the molecular anisotropy of $\Delta\chi_{fiber} = -\Delta\chi_{PL}/2$, which gives a contribution of 346ppb(L/mol) for a mole of

organized phospholipids. Preliminary analysis of this data shows average susceptibility anisotropy, $SA = \lambda_1 - (\lambda_2 + \lambda_3)/2$, of 27ppb within the NAWM surrounding Lesion 1, which is also a typical observation in literature(17,25,40,62), corresponding to ordered myelin sheaths. This yields a phospholipid concentration, [PL], of 0.078mol/L, which translates to a volume fraction of 0.24 for the white matter of the corpus callosum, similar to observed values of signal related to myelin and macromolecular components (102,103). The mean susceptibility observed, $\bar{\chi}_{obs}$, is related to the phospholipid concentration, [PL] , $\bar{\chi}_{obs} = \bar{\chi}_{PL}$ [PL], $\bar{\chi}_{PL}$ is the mean molar susceptibility contribution of phospholipids. The normalized trace of ordered cylindrical fibers and disordered phospholipids tensors shows the same mean susceptibility, $\bar{\chi} = (2\chi_{\perp} + \chi_{\parallel})/3$, where $\chi_{\perp}$ and $\chi_{\parallel}$ are the magnetic polarizabilities of the phospholipid molecules. Preliminary χ_{Myelin} results shows the susceptibility of tissue components excluding iron in NAWM of -34.9ppb, which gives a mean molar contribution of -449ppb(L/mol) for phospholipid molecules. Phospholipid fraction, PF, from the χ_{Myelin} was calculated using the mean molecular weight(100) and density of phospholipids(101) from the estimated molar contribution of phospholipids, PF =(χ_{Myelin} 775(g/mol)1000/ ($\bar{\chi}_{PL}$ 0.25(g/cm^3)).

The mean molar susceptibility contribution of phospholipids, a major tissue component of myelin(104), was estimated to be $\bar{\chi}_{PL}$ =-449ppb (L/mol) (see supplementary materials for details). The mean susceptibility was used to assess the myelin content independent of molecular order and thus applicable in both the lesion

and NAWM. The mean susceptibility observed, $\overline{\chi}_{obs}$, is related to the phospholipid concentration [PL] , $\overline{\chi}_{obs} = \overline{\chi}_{PL}$ [PL]. The commonly used average molecular weight, 775g/mol (100), density, 0.25g/cm^3(101), and $\overline{\chi}_{PL}$ was used to estimate the phospholipid fraction, PF, within a voxel from the observed χ_{Myelin}. Regions of interest, the center and border of the lesions, were drawn on the T2*w image of the lesions registered to the histological data; the border was the hyper-intense rim surrounding the center of the lesion and normal appearing white matter (NAWM) was identified nearby within the [Fe] map. Susceptibility from iron and χ_{Myelin} were observed along profiles through the border of the lesion.

5.4 Results

5.4.1 MRI signal Properties of MS Lesions

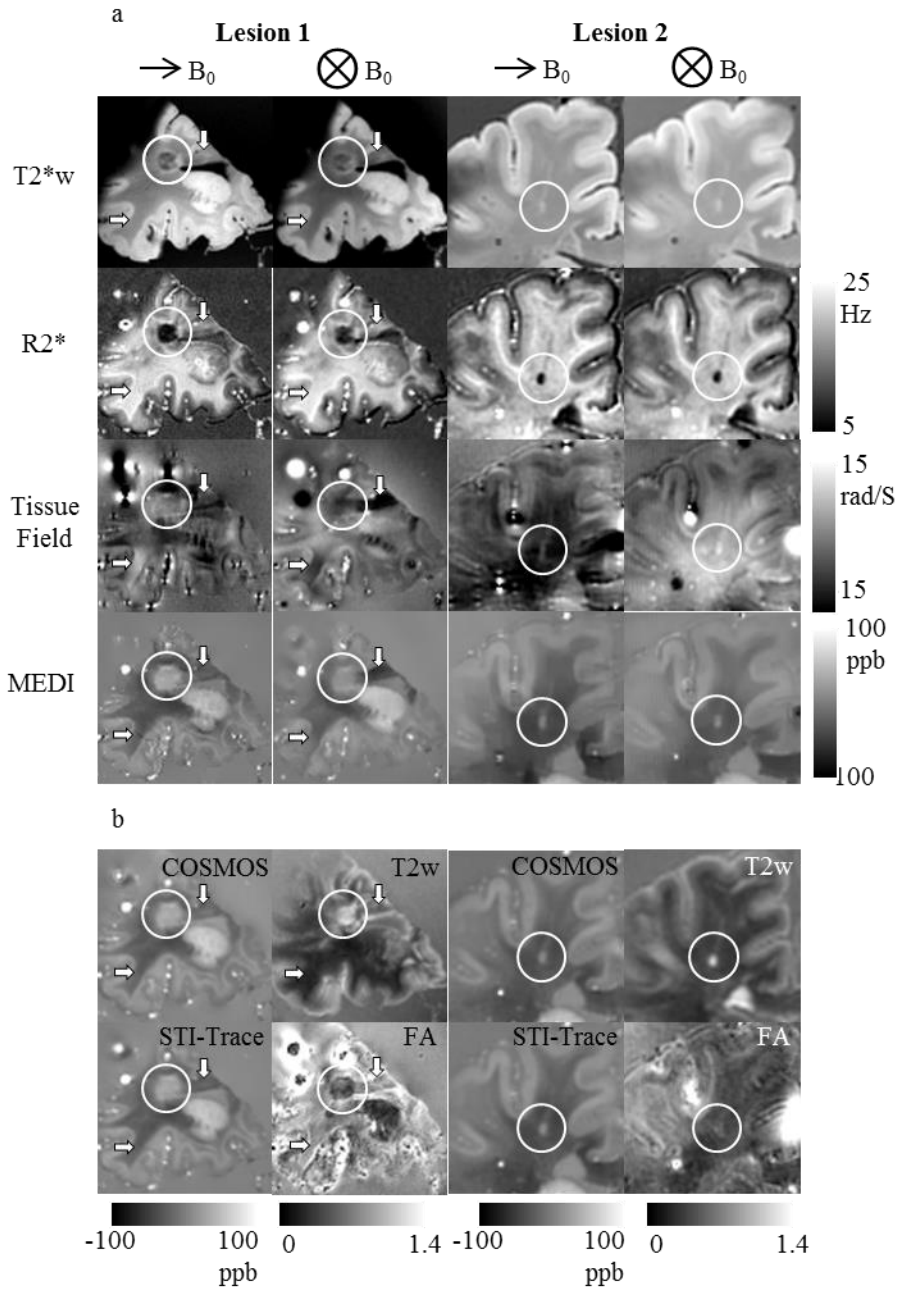

Figure 5.1: a, shows measurements of the GRE images within Lesion 1 and 2 between two different B_0 directions. From top to bottom, T2* weighted image, R2*, the tissue field (phase), single orientation MEDI-QSMs. b, displays the COSMOS-QSM and the normalized STI-Trace , the second column shows a T2w image and the FA estimated from the STI for the lesions. The circle corresponds to the lesion, and the arrows point to NAWM.

Orientation dependence of the MEDI-QSM and R2* is apparent in the NAWM, Fig. 5.1 row 2 and 4, particularly in the corpus callosum (fig. 5.1 row 4, arrows). The images in the right column for the lesions, Fig. 5.1, were registered to the orientation in the left column, there was slight blurring of bright susceptibility values within the lesion apparent in the left column after registration. Less dependence with orientation was observed within the lesions in MEDI-QSM. The nonlocal field extended from the lesion and changed in appearance between orientations in phase images (Fig. 5.1a row 3, circle). The COSMOS-QSM is very similar to the normalized tensor trace, STI-Trace, which is expected to estimate the same mean susceptibility under uniform measurements of the sample.

The measured phase switched sign when the tissue slab orientation changed in the magnet (Fig. 5.1a row 3, white arrows). The 2nd row of fig. 5.1b also shows changes in the estimated FA from STI showing a decrease in anisotropy within the lesion compared to NAWM particularly for lesion 1. The trace of the STI and COSMOS-QSM appeared the same with only small noise differences (Fig. 5.1b Column 1 for lesions 1 and 2), which was also confirmed theoretically in the supplemental materials.

5.4.2 Iron and Myelin Quantification

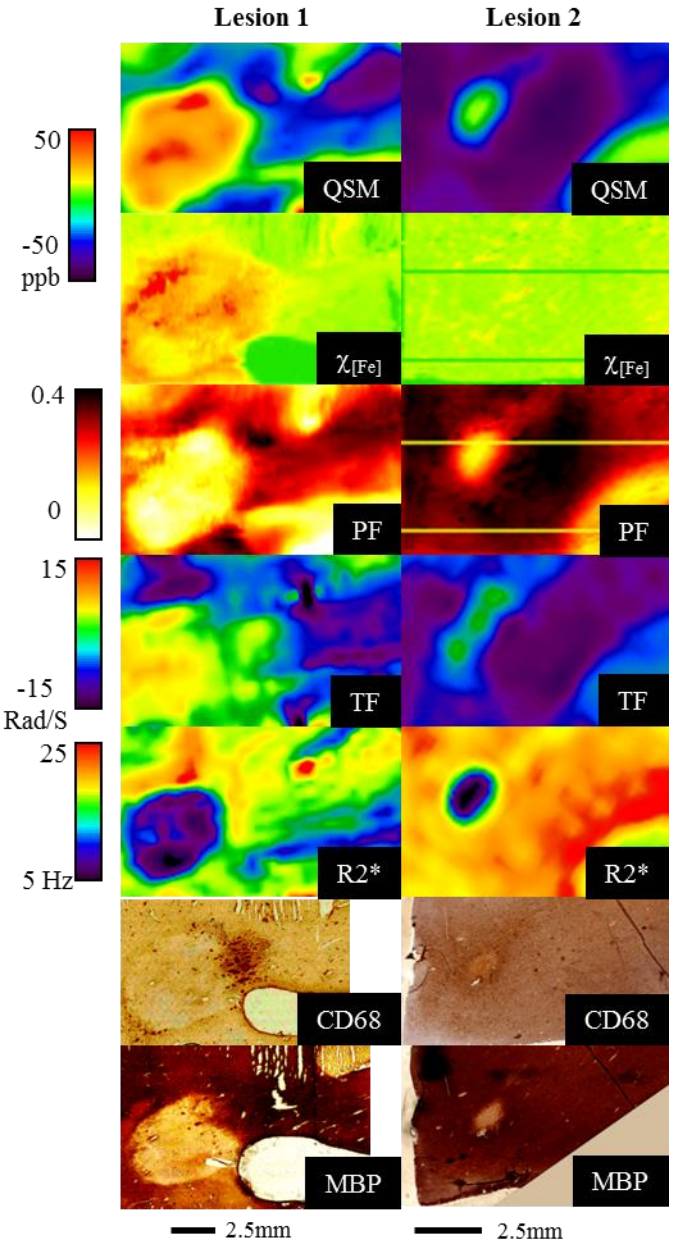

Figure 5.2: MRI and histology data on Lesion 1 (left) and 2 (right) the top row shows the QSM of the lesion registered with the histological sections, the next the $\chi_{[Fe]}$ map, the phospholipid fraction (PF), the tissue field (TF), R2*, the CD68 and MBP labeled sections. Lesion 1 contains a significant amount of iron within the lesion in LA-ICP-MS which is nearly all accounted for in the QSM, consistent with the demyelination observed in the MBP labeled section and PF. Lesion 2 shows little iron deposition.

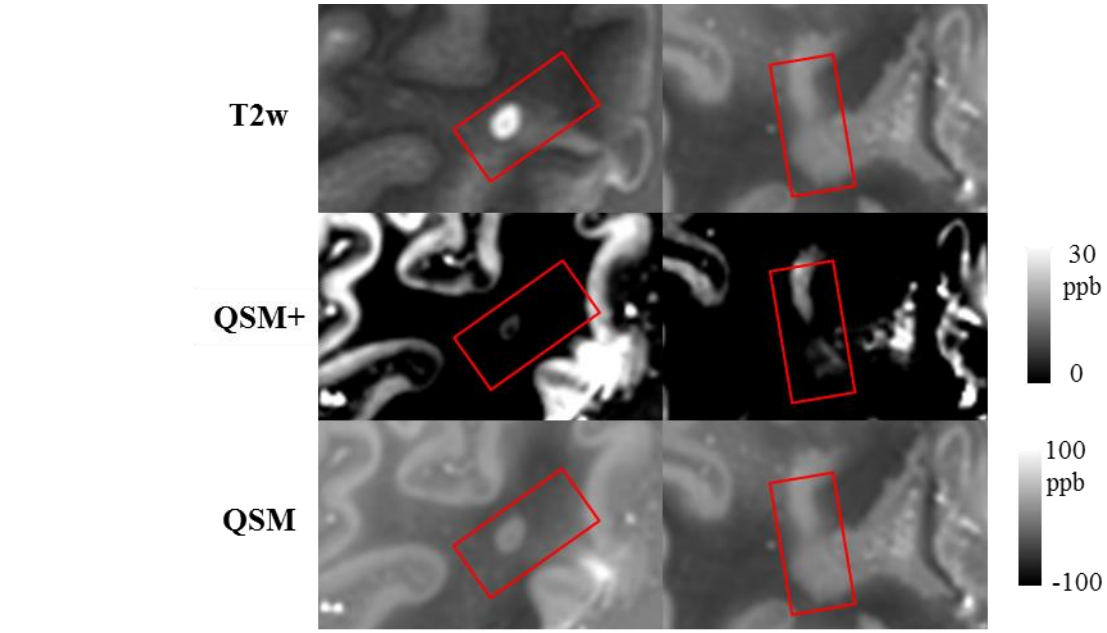
T2w
QSM+
QSM
30
ppb
0
100
ppb
-100

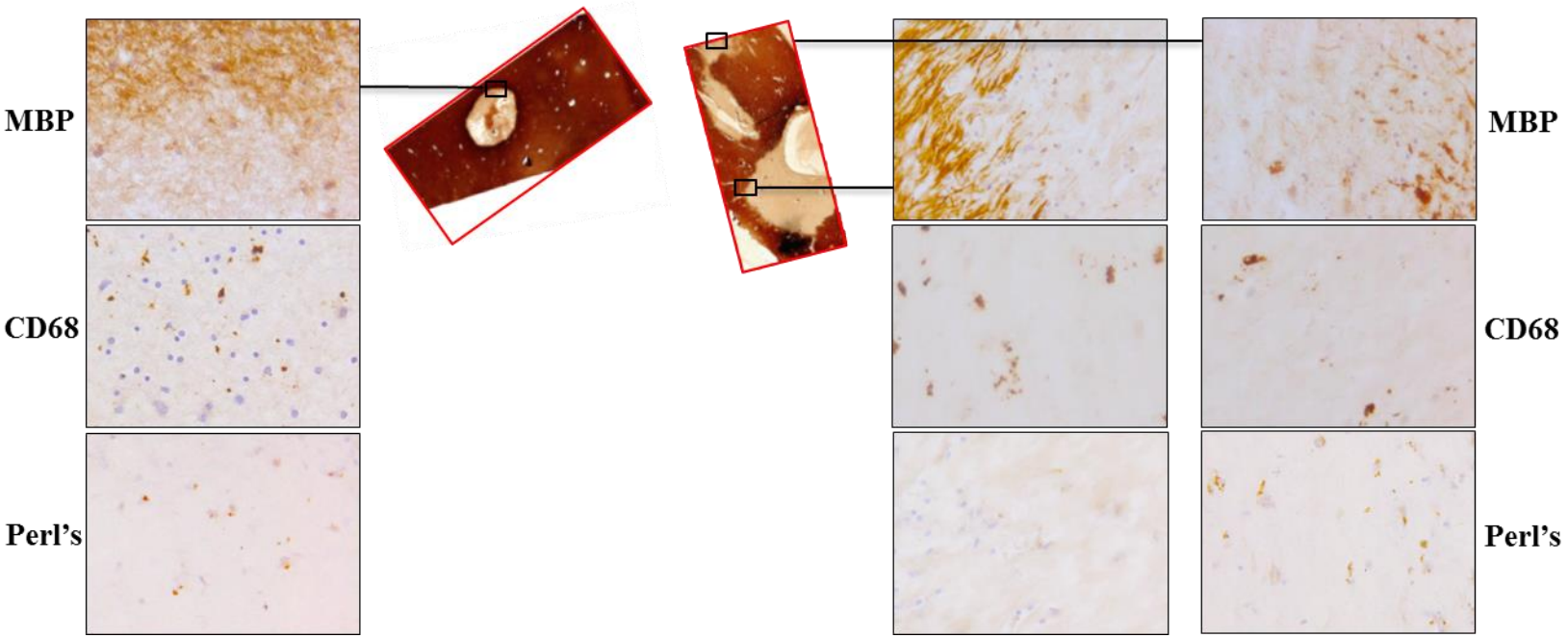
MBP
CD68
Perl's
MBP
CD68
Perl's

Figure 5.3: MRI and histology data on three additional lesions, the lesion on the left column shows little iron on Perl's and two lesions on the right with varying iron staining. The 1st row (1) shows T2w, (2), only positive susceptibility w.r.t. agar, (3) QSM, (4) MBP, (5) CD68 and (6) Perls.

In Fig. 5.3, Perls stain shows varying degrees of iron deposition with the lesions in the right column and relatively little in the lesion in the left column. The QSM+ row shows locations of positive susceptibility where the lesion is completely demyelinated on MBP, which correlates to the centers of the lesion. In the lesions on the right both Perls and CD68 slides showed the most staining at the rim of the lesions.

QSM correlated with the iron deposition [Fe] at the centers of Lesion 1 and Lesion 2 in Fig. 5.2. Lesion 1 had substantial iron content and correspondingly high paramagnetic susceptibility 29.6±5.5ppb (Table 1), but Lesion 2 had little iron and nearly zero diamagnetic susceptibility -1.6±4.8ppb (Table 1). There was no significant staining of iron containing CD68 labeled cells within Lesion 2. The PFs in Figs. 2 depicted loss of myelin in the lesion centers, consistent with the MBP labeled slides where PFs were close to 0 (Table 1). Row 5 shows decreased in R2* in both lesions correlating spatially with demyelinaiton observed on MBP labeled slides, Fig. 5.2. CD68 labeling showed evidence of microglia associated with the iron detected on LA-ICP-MS at the border of Lesion 1. Fig. 5.2 showed iron uniformly distributed within and surrounding lesion 2, with few punctate iron sources, two lines were skipped in the LA-ICP-MS data acquisition (two green lines in $\chi_{[Fe]}$, Fig. 5.2). The lesion borders showed differing amounts of iron and myelin contributing to the total susceptibility; lesion 1 had a high iron contribution, 25.1±6.1ppb and a small myelin contribution -

10.3±12.5ppb, whereas lesion 2 had a small iron contribution, 7.5±2.1ppb and a large myelin contribution -25.8±6.9ppb, table 1. Lesions with perl's staining only, Fig. 5.3, show mean susceptibilities of -4.4±8.7ppb(left column), -1.2±10.7ppb and -2.8 ±7.7ppb (top and bottom lesion in the right column of Fig. 5.4). The lesions in the right column showed highest peak susceptibility, 24.4 and 14.2ppb compared to 13.3ppb.

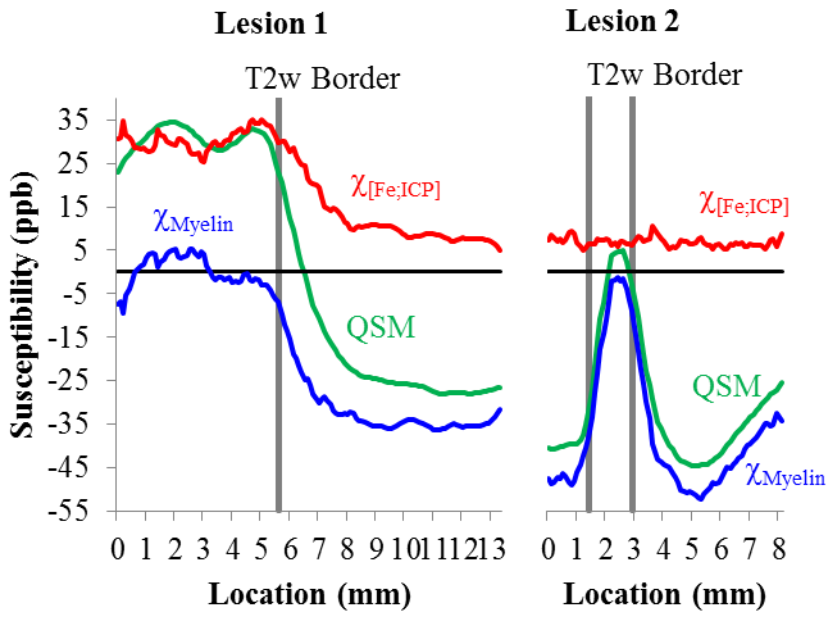

Figure 5.4: $\chi_{[Fe:ICP]}$, QSM and χ_{Myelin} across a profile through the lesions into NAWM; in lesions 1 the profile extents from within the lesion (location 0) to a location in NAWM. The gray bar indicates the location of the edge of the lesion as displayed on the registered T2w image.

In Lesion 1 the contribution to the susceptibility near the border came from both iron and myelin, while the main contribution to the susceptibility at the edge of

Lesion 2 came from myelin, Table 1. Fig. 5.4 shows a rapid increase in the myelin content at the immediate edge of Lesion 1 observed on T2w imaging. In this region, the iron content was high at the border and decreased to baseline NAWM within 2mm.

Table 5.5.1: Measurements of [Fe], total susceptibility from QSM, [Fe] susceptibility contribution, RSM and phospholipid fraction within the lesions and surrounding NAWM.

		[Fe] (ug/mL)	χ_{QSM} (ppb)	$\chi_{[Fe]}$ (ppb)	χ_{RSM} (ppb)	Phospholipid Fraction (PF)
Lesion 1	Lesion	19.7±5.6	29.6±5.5	27.6±7.8	2.0±8.5	-0.01±0.06
	Border	18.6±4.5	14.8±12.9	26.1±6.3	-11.3±12.6	0.08±0.09
	NAWM	7.9±1.1	-23.2±1.4	11.2±1.6	-34.4±2.6	0.24±0.02
Lesion 2	Lesion	4.5±0.5	-1.6±4.8	6.3±0.7	-7.9±4.6	0.05±0.03
	Border	5.6±1.5	-18.3±6.6	7.8±2.1	-26.1±7.0	0.18±0.05
	NAWM	5.3±0.9	-42.5±1.2	7.4±1.3	-49.9±1.9	0.34±0.01

The volumes of Lesion 1 were: COSMOS-QSM 312mm^3 and T2w 245.4mm^3, for Lesion 2: COSMOS-QSM 7.0mm^3 and T2w 6.6mm^3. In Lesion 1 where there is significant iron at the edge, the volume observed on QSM is 27% larger than the volume of the lesion on T2w, while in Lesion 2 there was only 5.6% difference in the volume of the lesion between T2w and QSM.

5.5 Discussion

While both iron and myelin can contribute to QSM, our results suggest the following two observations on interpreting iron from QSM of MS lesions in white matter. 1) When susceptibility values are above zero (relative to water), there is iron in lesion. This was corroborated on lesions with iron staining and can be explained by the physical limit that complete demyelination can only increase susceptibility values to

zero. 2) Susceptibility values permit iron quantification in fully demyelinated locations, which was corroborated on lesions with iron quantification and myelin staining.

In general, the mixture of iron and myelin makes it difficult to identify iron specifically from gradient echo (GRE) MRI data using the three quantitative processing methods: tissue field (or phase), R2* and QSM. Deconvolution of the tissue field to generate QSM only removes contributions outside a voxel that affect both tissue field and R2*, but does not separate diamagnetic myelin from paramagnetic iron within that voxel. It may be possible to identify myelin based on the anisotropy of its magnetic susceptibility, which makes tissue field, R2* and QSM dependent on orientation as observed in Fig.5.1. Susceptibility tensor imaging fractional anisotropy (STI FA) decreases in a lesion compared to NAWM, but STI FA is very difficult to quantify and prone to noise and other artifacts and may be impossible to perform in routine clinical practice (17,62).

Previous results have been promising relating tissue iron content to measured R2* and QSM. In this data, iron deposition and myelin loss content effect QSM and R2* in opposite ways; R2* decreased within the center of both lesions though Lesion 1 showed significant iron deposition and correspondingly high susceptibility, Fig. 5.2. This decrease in R2* is consistent with an increase in the homogeneity of the tissue that occurs within MS lesions (105). Though R2* may not be directly related to iron content observed this data, together QSM and R2* reflect differences in the total magnetization and organization between NAWM and the lesion.

Most white matter lesions in MS brain specimens seem to be completely demyelinated (106), as observed in this study. For completely demyelinated lesion center, iron may be regarded as the main source for paramagnetic susceptibility, which was corroborated in Fig.5.4. Iron deposition is associated predominantly with activated microglia/macrophages in the rim of demyelinating lesions (77), as observed in Fig. 5.3; iron is observed infrequently in the lesion center, as in Fig. 5.2 for lesion 1. The non-zero iron concentration varied in space in all lesions (Fig.5.2&3). The huge difference in slice thickness between QSM and LA-ICP-MS makes it difficult to generate meaningful linear voxel-based linear regression, which would require multiple LA-ICP-MS samples through a QSM slice.

Interestingly, the lesion volume on QSM was observed to be bigger than that on T2w for lesions with iron (Fig.5.4). QSM is sensitive to iron present outside lesion border and T2w is mostly sensitive to reduced cellular contents in lesion interior (107,108) , resulting a larger volume on QSM. This QSM-T2w lesion volume difference could help identify the presence iron at the border of the lesion, where QSM alone cannot identify iron as both iron and myelin contribute to the measured magnetic susceptibility. Additional in vivo measurement of tissue composition, such as myelin water fraction data (5), may help to define the region of demyelination. It has been observed in vivo that T2w is highly sensitive to tissue inflammation increasing the observed lesion volume (74). Our T2w results support that MRI measurements of specific tissue content may potentially identify the spatial distribution of myelin and iron within MS lesions.

While this study focused on MS lesions, NAWM iron content was also measured. These NAWM iron values are ~4-5x smaller than previously observed in normal white matter within non-neurological controls (58). However, this iron content is consistent with observations of NAWM in autopsied MS brains where densitometric measurements showed NAWM 0.03 and normal white matter 0.13 (80).

One disadvantage of our study is that we examined MS lesions from one individual. Similar comparative work is usually also restricted to a small number of autopsy cases (76,77). Registration between MRI and histology sections is not trivial and may result in registration errors from differences in resolution and image contrast between techniques. The best registration results were found when using all histological data in the formation of a volume that was used to match multiple anatomical features present in both MR and histology. The focus of this work is in the assessment of sources of susceptibility in the lesions that contribute to the measured susceptibility observed with QSM. More pathology will be assessed in future work.

5.6 Conclusion

In this work, spatial resolution of iron distributed within and surrounding MS lesions identified iron contributions to the measured susceptibility with QSM across the anatomy of MS lesions. Positive susceptibility values in MS lesion are associated with iron presence in histology. In completely demyelinated lesion centers, susceptibility values are consistent with susceptibility contributions from ferritin

measured by laser ablation inductively coupled plasma mass spectrometry.

CHAPTER 6

6 CONCLUSIONS AND FUTURE WORK

The focus of this work is the content and structure of tissue in the central nervous system from MRI field measurements particularly in the assessment of orientation dependent magnetic susceptibility and relaxation in white matter. This work has (1) examined aspects of the reconstruction of these orientation dependent properties from multiple orientation acquisitions in the analysis of error propagation of various susceptibility tensor reconstructions. Similarly (2) the stability and structure of susceptibility and relaxation reconstructions from acquired data were assessed statistically to demonstrate the presence of molecularly ordered versus disordered sub-voxel structures in the brain. (3) Origins of susceptibility within white matter lesions were assessed with an in vitro analysis of white matter lesions quantitatively assessing the myelin and iron content with histological and MRI data. This work has demonstrated the acquisition and assessment of white matter tissue content and structure from MRI field measurements, which will guide future work in building robust tensor reconstructions and interpreting orientation dependent MRI data.

6.1 Future Work

6.1.1 Assessment of sub-voxel tissue microstructure

Gradient echo data has been a rich source of information in measuring the content and organization of tissue in this work. Post processing methods remain a challenge in better utilizing the available data and reduce noise in the reconstructed tensor properties. Prior information can not only better utilize gradient echo data, but also use complementary contrast mechanisms

available with MRI to gain information on tissue content and architecture.

As demonstrated in chapters 3 and 4 of this work magnetic susceptibility tensor properties are difficult to construct due to the condition of the inverse problem and limited data available in vivo. As also examined in chapter 4 there is significant structural similarity between susceptibility and relaxation properties of white matter. Maintaining structural similarity between tensors in the construction would be a strong prior that could utilize the similarity in structural information in both magnitude and phase data in reconstructing magnetic susceptibility and relaxation tensor properties of white matter simultaneously. The challenge here is maintaining the structural similarity between tensors while allowing the eigenvalues of the tensors to reflect the susceptibility and relaxation properties of the material.

6.1.2 Applications of microstructural measurements

Single orientation MRI measurements of tissue properties from a multi parametric analysis may also aid in the assessment of MS lesion content in vivo. This work has assessed major contributions to the MR signal from orientation dependent properties arising from the tissue magnetization, which required significant time and effort on the part of the subjects in acquiring the data. This poses a challenge in translating tensor measurements to clinical applications. Components of the tensors can be assessed with single orientations; through the apparent tensor properties related to the structure and content of the tissue. Relating single orientation properties of the subject to the magnetic and relaxation properties explored in this work would greatly help in applying tensor properties of the tissue into clinical practice. Relaxation and susceptibility present a unique opportunity to explore tissue heterogeneity and

molecular organization respectively. The challenge here is in interpreting partial information about the underlying tensor properties from limited measurements from gradient echo imaging.

MRI is a versatile imaging paradigm that has been used to quantitatively probe various aspects of tissue properties from their influence of the MR signal. Examples of mechanisms exploited in MRI are diffusion tensor imaging(59), T2 relaxometry(109) and QSM(31), which probe water mobility, multiple water compartments and magnetization respectively with MRI data. Data from measurements like DTI and T2 relaxometry, could be utilized in a multi-parametric analysis in assessing both the content and structure of voxels. Diffusion data can help account for data that is dependent on the orientation of fibers within the tissue and indirectly measure the fiber orientation. Additional T2 and spectroscopy data may potentially help differentiate between tissue components, such as the influence of myelin. These single orientation measurements are sensitized to different aspects of the content and architecture of the voxel which is a potential source of interpreting the relative influence of each component. As investigated in chapter 5 QSM is sensitive to both iron and myelin content of the tissue in general. The challenge in separating myelin and water content, for example, will likely require an estimate of the influence of myelin content on T2 relaxometry to estimate the influence of myelin on QSM given the behavior of myelin in both T2 and QSM.

REFERENCES

1. Liang Z-P, Lauterbur PC. Principles of Magnetic Resonance Imaging. Akay M, editor. Piscataway NJ: IEEE Press; 2000.
2. Wang Y. Principles of Magnetic Resonance Imaging: Physics Concepts, Pulse Sequences, & Biomedical Applications: CreateSpace Independent Publishing; 2012.
3. de Rochefort L, Brown R, Prince M, Wang Y. Quantitative MR Susceptibility Mapping using piece-wise contast regularized inversion of the magnetic field. Magnetic Resonance in Medicine 2008;60:1003-1009.
4. Waxman S, Kocsis J, Stys P. The Axon: Structure Function and Pathophysiology: Oxford University Press; 1995.
5. Laule C, Vavasour IM, Kolind SH, Li DK, Traboulsee TL, Moore GR, MacKay AL. Magnetic resonance imaging of myelin. Neurotherapeutics 2007;4(3):460-484.
6. Liu C. Susceptibility tensor imaging. Magn Reson Med 2010;63(6):1471-1477.
7. Weickert J, Hagen H, SpringerLink (Online service). Visualization and processing of tensor fields. Mathematics + visualization. Berlin: Springer,; 2006. p xv, 481 p.
8. Koenig E. Cell Biology of the Axon. Richter D, Tiedge H, editors: Springer; 2009.
9. Waxman SG, D. KJ, Stys PK. The Axon: Structure, Function and Pathophysiology. New York: Oxford University Press; 1995.
10. Lee J, Shmueli K, Fukunaga M, Van Gelderen P, Merkle H, Silva A, Duyn JH. Sensitivity of MRI resonance frequency to the orientation of brain tissue microstructure. PNAS 2010;107(11):5130-5135.
11. Denk C, Torres EH, MacKay A, Rauscher A. The Influence of White Matter Fiber Orientation on MR Signal Phase and Decay. NMR in Biomedicine 2011;24:246-252.
12. Bender B, Klose, U. The in vivo influence of white matter fiber orientation towards B0 on T2* in the human brain. NMR in Biomedicine 2010;23:1071-1076.
13. Lee J, van Gelderen P, Kuo LW, Merkle H, Silva AC, Duyn JH. T2*-based fiber orientation mapping. Neuroimage 2011;57(1):225-234.
14. Kimura T, Yamato M, Aoki H, Yamamoto I, Ishikawa F, Yamaguchi M, Tobita M. Determination of anisotropic diamagnetic susceptibility of polymeric fibers suspended in liquid. Jpn J Appl Phys 1 2001;40(4A):2237-2240.
15. Hrouda F, Schulmann K. Conversion of the Magnetic-Susceptibility Tensor into the Orientation Tensor in Some Rocks. Phys Earth Planet In 1990;63(1-2):71-77.
16. Prosser RS, Hwang JS, Vold RR. Magnetically aligned phospholipid bilayers with positive ordering: a new model membrane system. Biophys J 1998;74(5):2405-2418.
17. Li W, Wu B, Avram AV, Liu C. Magnetic susceptibility anisotropy of human brain in vivo and its molecular underpinnings. NeuroImage 2012;59(3):2088-2097.
18. Wisnieff C, Liu T, Spincemaille P, Wang Y. Feasible 3-Orientation Acquisition for Detecting Susceptibility Anisotropy in the Human Brain Using Prior Structural Information. 2012; Melbourne. p 3444.
19. Wisnieff C, Liu T, Wang Y. Anatomic Prior and Cylindrical Symmetry Constraints for Reconstructing Susceptibility Tensor. 2012; Melbourne. p 3445.
20. Prosser RS, Volkov VB, Shiyanovskaya IV. Solid-state NMR studies of magnetically aligned phospholipid membranes: taming lanthanides for membrane protein studies. Biochem Cell Biol 1998;76(2-3):443-451.

21. Li W, Wu B, Liu C. In Vivo Evidence of Susceptibility Anisotropy and Susceptibility Tensor Imaging of Human Brain. Proc Intl Soc Mag Reson Med 2011;19:121.
22. Hext G. The Estimation of Second-Order Tensors, with Related Tests and designs. Biometrika 1963;50.
23. Wharton S, Bowtell R. A Simplified Approach for Anisotropic Susceptibility Map Calculation. Proc Intl Soc Mag Reson Med 2011;19:4515.
24. Clark CA, Werring DJ, Miller DH. Diffusion imaging of the spinal cord in vivo: estimation of the principal diffusivities and application to multiple sclerosis. Magn Reson Med 2000;43(1):133-138.
25. Li X, Vikram DS, Lim IA, Jones CK, Farrell JA, van Zijl PC. Mapping magnetic susceptibility anisotropies of white matter in vivo in the human brain at 7T. NeuroImage 2012;62(1):314-330.
26. Schenck JF. The role of magnetic susceptibility in magnetic resonance imaging: MRI magnetic compatibility of the first and second kinds. Medical Physics 1996;23(6):815-850.
27. Bertini I, Luchinat C, Parigi G. Magnetic susceptibility in paramagnetic NMR. Prog Nucl Mag Res Sp 2002;40(3):249-273.
28. Lounila J, Ala-Korpela M, Jokisaari J, Savolainen MJ, Kesaniemi YA. Effects of orientational order and particle size on the NMR line positions of lipoproteins. Physical Review Letters 1994;72(25):4049-4052.
29. Haacke EM, Cheng NYC, House MJ, Liu Q, Neelavalli J, Ogg RJ, Khan A, Ayaz M, Kirsch W, Obenaus A. Imaging iron stores in the brain using magnetic resonance imaging. Magnetic Resonance in Medicine 2005;23:1-25.
30. de Rochefort L, Nguyen T, Brown R, Spincemaille P, Choi G, Weinsaft J, Prince MR, Wang Y. In vivo quantification of contrast agent concentration using the induced magnetic field for time resolved arterial input function measurement with MRI. Medical Physics 2008;35(12).
31. Liu J, Liu T, de Rochefort L, Ledoux J, Khalidov I, Chen W, Tsiouris AJ, Wisnieff C, Spincemaille P, Prince MR, Wang Y. Morphology enabled dipole inversion for quantitative susceptibility mapping using structural consistency between the magnitude image and the susceptibility map. Neuroimage 2012;59(3):2560-2568.
32. Schweser F, Deistung A, Sommer K, Reichenbach JR. Toward online reconstruction of quantitative susceptibility maps: Superfast dipole inversion. Magn Reson Med 2012.
33. de Rochefort L, Liu T, Kressler B, Liu J, Spincemaille P, Lebon V, Wu J, Wang Y. Quantitative Susceptibility Map Reconstruction from MR Phase Data Using Bayesian Regularization: Validation and Applications to Brain Imaging. Magnetic Resonance in Medicine 2010;63:194-206.
34. Li W, Wu B, Liu C. Quantitative susceptibility mapping of human brain reflects spatial variation in tissue composition. NeuroImage 2011;55(4):1645-1656.
35. Bilgic B, Pfefferbaum A, Rohlfing T, Sullivan EV, Adalsteinsson E. MRI estimates of brain iron concentration in normal aging using quantitative susceptibility mapping. Neuroimage 2012;59(3):2625-2635.
36. Hammermesh M. Group Theory and Its Application to Physical Problems. New York: Dover Publications, Inc.; 1962.
37. Kusumi A, Fujiwara TK, Chadda R, Xie M, Tsunoyama TA, Kalay Z, Kasai RS, Suzuki KG. Dynamic Organizing Principles of the Plasma Membrane that Regulate Signal

Transduction: Commemorating the Fortieth Anniversary of Singer and Nicolson's Fluid-Mosaic Model. Annu Rev Cell Dev Biol 2012;28:215-250.
38. Bagatolli LA, Ipsen JH, Simonsen AC, Mouritsen OG. An outlook on organization of lipids in membranes: searching for a realistic connection with the organization of biological membranes. Prog Lipid Res 2010;49(4):378-389.
39. Roberts PH, Winch DE. On Random Rotations. Adv Appl Probab 1984;16(3):638-655.
40. Liu C, Li W, Johnson GA, Wu B. High-field (9.4 T) MRI of brain dysmyelination by quantitative mapping of magnetic susceptibility. Neuroimage 2011;56(3):930-938.
41. Schaub H, Junkins JL. Analytical Mechanics of Space Systems. American Institute if Areonautics and Astronautics; 2003.
42. Demmel JW. Applied Numerical Linear Algebra. Philadelphia: SIAM; 1997.
43. Liu T, Spincemaille P, de Rochefort L, Kressler B, Wang Y. Calculation of Susceptibility Through Multiple Orientation Sampling (COSMOS): A Method for Conditioning the Inverse Problem From Measured Field Map to Susceptibility Source Image in MRI. Magnetic Resonance in Medicine 2009;61:196-204.
44. Zhang YY, Brady M, Smith S. Segmentation of brain MR images through a hidden Markov random field model and the expectation-maximization algorithm. IEEE Transactions on Medical Imaging 2001;20(1):45-57.
45. Liu T, Liu J, de Rochefort L, Spincemaille P, Khalidov I, Ledoux JR, Wang Y. Morphology enabled dipole inversion (MEDI) from a single-angle acquisition: Comparison with COSMOS in human brain imaging. Magn Reson Med 2011.
46. Kressler B, de Rochefort L, Liu T, Spincemaille P, Jiang Q, Wang Y. Nonlinear regularization for per voxel estimation of magnetic susceptibility distributions from MRI field maps. IEEE Transactions on Medical Imaging 2010;29.
47. Cusack R, Papadakis N. New robust 3-D phase unwrapping algorithms: application to magnetic field mapping and undistorting echoplanar images. NeuroImage 2002;16(3 Pt 1):754-764.
48. Liu C, Li W, Wu B, Jiang Y, Johnson GA. 3D fiber tractography with susceptibility tensor imaging. NeuroImage 2012;59(2):1290-1298.
49. Crum WR, Rueckert D, Jenkinson M, Kennedy D, Smith SM. A framework for detailed objective comparison of non-rigid registration algorithms in neuroimaging. Lect Notes Comput Sc 2004;3216:679-686.
50. Kimura T, Yamato M, Koshimizu W, Koike M, Kawai T. Magnetic orientation of polymer fibers in suspension. Langmuir 2000;16(2):858-861.
51. Stys PK, Zamponi GW, van Minnen J, Geurts JJG. Will the real multiple sclerosis please stand up? Nat Rev Neurosci 2012;13(7):507-514.
52. Sander S, Ouvrier RA, McLeod JG, Nicholson GA, Pollard JD. Clinical syndromes associated with tomacula or myelin swellings in sural nerve biopsies. J Neurol Neurosur Ps 2000;68(4):483-488.
53. Cai Z, Cash K, Swift J, Sutton-Smith P, Robinson M, Thompson PD, Blumbergs PC. Focal myelin swellings and tomacula in anti-MAG IgM paraproteinaemic neuropathy: novel teased nerve fiber studies. J Peripher Nerv Syst 2001;6(2):95-101.
54. Perlman SJ, Mar S. Leukodystrophies. Adv Exp Med Biol 2012;724:154-171.
55. Keough MB, Yong VW. Remyelination Therapy for Multiple Sclerosis. Neurotherapeutics 2012.

56. Wharton S, Bowtell R. Whole-Brain Susceptibility Mapping at High Field: A Comparison of Multiple- and Single-Orientation Methods. NeuroImage 2010;53:515-525.
57. Liu T, Wisnieff C, Lou M, Chen W, Spincemaille P, Wang Y. Nonlinear formulation of the magnetic field to source relationship for robust quantitative susceptibility mapping. Magn Reson Med 2013;69(2):467-476.
58. Langkammer C, Schweser F, Krebs N, Deistung A, Goessler W, Scheurer E, Sommer K, Reishofer G, Yen K, Fazekas F, Ropele S, Reichenbach JR. Quantitative susceptibility mapping (QSM) as a means to measure brain iron? A post mortem validation study. Neuroimage 2012;62(3):1593-1599.
59. Basser PJ, Jones DK. Diffusion-tensor MRI: theory, experimental design and data analysis - a technical review. NMR Biomed 2002;15(7-8):456-467.
60. Wharton S, Bowtell R. Fiber orientation-dependent white matter contrast in gradient echo MRI. Proc Natl Acad Sci U S A 2012;109(45):18559-18564.
61. Rudko DA, Klassen LM, de Chickera SN, Gati JS, Dekaban GA, Menon RS. Origins of Formula orientation dependence in gray and white matter. Proc Natl Acad Sci U S A 2013.
62. Wisnieff C, Liu T, Spincemaille P, Wang S, Zhou D, Wang Y. Magnetic susceptibility anisotropy: Cylindrical symmetry from macroscopically ordered anisotropic molecules and accuracy of MRI measurements using few orientations. Neuroimage 2013;70:363-376.
63. Jackson JD. Classical electrodynamics, third edition: John Wiley and Sons, inc.; 1999.
64. Yablonskiy DA, Haacke EM. Theory of NMR signal behavior in magnetically inhomogeneous tissues: the static dephasing regime. Magn Reson Med 1994;32(6):749-763.
65. Jenkinson M, Smith S. A global optimisation method for robust affine registration of brain images. Med Image Anal 2001;5(2):143-156.
66. Jenkinson M, Bannister P, Brady M, Smith S. Improved optimization for the robust and accurate linear registration and motion correction of brain images. Neuroimage 2002;17(2):825-841.
67. Jenkinson M, Beckmann CF, Behrens TE, Woolrich MW, Smith SM. FSL. Neuroimage 2012;62(2):782-790.
68. Pei M, Nguyen TD, Thimmappa ND, Salustri C, Dong F, Cooper MA, Li J, Prince MR, Wang Y. Algorithm for fast monoexponential fitting based on Auto-Regression on Linear Operations (ARLO) of data. Magn Reson Med 2014.
69. Constantinides C, Atalar E, McVeigh E. Signal-to-noise measurements in magnitude images from NMR phased arrays. Magnetic Resonance in Medicine 1997;38(5):852-857.
70. Whitcher B, Tuch DS, Wisco JJ, Sorensen AG, Wang L. Using the wild bootstrap to quantify uncertainty in diffusion tensor imaging. Hum Brain Mapp 2008;29(3):346-362.
71. Jones DK. Determining and visualizing uncertainty in estimates of fiber orientation from diffusion tensor MRI. Magn Reson Med 2003;49(1):7-12.
72. Liu R. BOOTSTRAP PROCEDURES UNDER SOME NON-IID MODELS. Annals of Statistics 1988;16(4):1696-1708.
73. Basser PJ, Pajevic S. Statistical artifacts in diffusion tensor MRI (DT-MRI) caused by background noise. Magn Reson Med 2000;44(1):41-50.

74. Chen W, Gauthier S, Gupta A, Comunale J, Liu T, Wang S, Pei M, Pitt D, Wang Y. Dynamic magnetic property of multiple sclerosis lesions at various ages measured by quantitative susceptibility mapping. 2013 Salt Lake City, USA. p 0692
75. Wiggermann V, Hernández Torres E, Vavasour IM, Moore GR, Laule C, MacKay AL, Li DK, Traboulsee A, Rauscher A. Magnetic resonance frequency shifts during acute MS lesion formation. Neurology 2013;81(3):211-218.
76. Bagnato F, Hametner S, Yao B, van Gelderen P, Merkle H, Cantor FK, Lassmann H, Duyn JH. Tracking iron in multiple sclerosis: a combined imaging and histopathological study at 7 Tesla. Brain 2011;134(Pt 12):3602-3615.
77. Mehta V, Pei W, Yang G, Li S, Swamy E, Boster A, Schmalbrock P, Pitt D. Iron is a sensitive biomarker for inflammation in multiple sclerosis lesions. PLoS One 2013;8(3):e57573.
78. LeVine SM, Chakrabarty A. The role of iron in the pathogenesis of experimental allergic encephalomyelitis and multiple sclerosis. Ann N Y Acad Sci 2004;1012:252-266.
79. Pitt D, Boster A, Pei W, Wohleb E, Jasne A, Zachariah CR, Rammohan K, Knopp MV, Schmalbrock P. Imaging cortical lesions in multiple sclerosis with ultra-high-field magnetic resonance imaging. Arch Neurol 2010;67(7):812-818.
80. Hametner S, Wimmer I, Haider L, Pfeifenbring S, Brück W, Lassmann H. Iron and neurodegeneration in the multiple sclerosis brain. Ann Neurol 2013;74(6):848-861.
81. Al-Radaideh AM, Wharton SJ, Lim SY, Tench CR, Morgan PS, Bowtell RW, Constantinescu CS, Gowland PA. Increased iron accumulation occurs in the earliest stages of demyelinating disease: an ultra-high field susceptibility mapping study in Clinically Isolated Syndrome. Mult Scler 2013;19(7):896-903.
82. Langkammer C, Krebs N, Goessler W, Scheurer E, Ebner F, Yen K, Fazekas F, Ropele S. Quantitative MR imaging of brain iron: a postmortem validation study. Radiology 2010;257(2):455-462.
83. Walsh AJ, Lebel RM, Eissa A, Blevins G, Catz I, Lu JQ, Resch L, Johnson ES, Emery DJ, Warren KG, Wilman AH. Multiple sclerosis: validation of MR imaging for quantification and detection of iron. Radiology 2013;267(2):531-542.
84. Li J, Chang S, Liu T, Wang Q, Cui D, Chen X, Jin M, Wang B, Pei M, Wisnieff C, Spincemaille P, Zhang M, Wang Y. Reducing the object orientation dependence of susceptibility effects in gradient echo MRI through quantitative susceptibility mapping. Magn Reson Med 2012;68(5):1563-1569.
85. Shmueli K, de Zwart JA, van Gelderen P, Li TQ, Dodd SJ, Duyn JH. Magnetic susceptibility mapping of brain tissue in vivo using MRI phase data. Magn Reson Med 2009;62(6):1510-1522.
86. Wang S, Lou M, Liu T, Cui D, Chen X, Wang Y. Hematoma volume measurement in gradient echo MRI using quantitative susceptibility mapping. Stroke; a journal of cerebral circulation 2013;44(8):2315-2317.
87. Stüber C, Morawski M, Schäfer A, Labadie C, Wähnert M, Leuze C, Streicher M, Barapatre N, Reimann K, Geyer S, Spemann D, Turner R. Myelin and iron concentration in the human brain: A quantitative study of MRI contrast. Neuroimage 2014.
88. Chen W, Zhu W, Kovanlikaya I, Kovanlikaya A, Liu T, Wang S, Salustri C, Wang Y. Intracranial calcifications and hemorrhages: characterization with quantitative susceptibility mapping. Radiology 2014;270(2):496-505.

89. Zheng W, Nichol H, Liu S, Cheng YC, Haacke EM. Measuring iron in the brain using quantitative susceptibility mapping and X-ray fluorescence imaging. Neuroimage 2013;78:68-74.
90. Xie L, Dibb R, Cofer GP, Li W, Nicholls PJ, Johnson GA, Liu C. Susceptibility tensor imaging of the kidney and its microstructural underpinnings. Magn Reson Med 2014.
91. He X, Yablonskiy DA. Biophysical mechanisms of phase contrast in gradient echo MRI. PNAS 2009;106(32):13558-13563.
92. Luo J, He X, Yablonskiy D. Magnetic Susceptibility Induced White Matter MR Signal Frequency Shifts-Experimental Comparison Between Lorentzian Sphere and Generalized Lorentzian Approaches. Magnetic Resonance in Medicine 2014;71(3):1251-1263.
93. Wharton S, Bowtell R. Effects of white matter microstructure on phase and susceptibility maps. Magn Reson Med 2014.
94. Hamermesh M. Group Theory and Its Application to Physical Problems. New York: Dover Publications; 1962.
95. Liu T, Khalidov I, de Rochefort L, Spincemaille P, Liu J, Tsiouris AJ, Wang Y. A novel background field removal method for MRI using projection onto dipole fields (PDF). NMR Biomed 2011;24(9):1129-1136.
96. Schenk JF. Health and Physiological Effects of Human Exposure to Whole-Body Four-Tesla Magnetic Fields during MRI. ANNALS NEW YORK ACADEMY OF SCIENCES 1992;649:285-301.
97. Hilty S, Webb B, Frankel R, Watt G. Iron Core Formation in Horse Spleen Ferritin - Magnetic-Susceptibility, PH, and Compositional Studies. Journal of Inorganic Biochemistry 1994;56(3):173-185.
98. Barber TW, Brockway JA, Higgins LS. The density of tissues in and about the head. Acta Neurol Scand 1970;46(1):85-92.
99. Lee J, Shmueli K, Kang BT, Yao B, Fukunaga M, van Gelderen P, Palumbo S, Bosetti F, Silva AC, Duyn JH. The contribution of myelin to magnetic susceptibility-weighted contrasts in high-field MRI of the brain. Neuroimage 2012;59(4):3967-3975.
100. Young-Sik P, No-Soo P, Jun-Bong S, Soo-Kyoung B, Ki-Soo S, Young-Jun K, Ju-Won P, Joung-Moung S, Young-Chan J, In-Kyo C. The effect of dimiristoylphosphatidylethanol on the rotational mobility of n-(9-Anthroyloxy) stearic acid in neuronal and model membranes. Journal of Biophysical Chemistry 2010;2010.
101. Azanza M, Blott B, Delmoral A, Peg M. Measurement of the Red-Blood-Cell Membrane Magnetic-Susceptibility. Bioelectrochemistry and Bioenergetics 1993;30(1-3):43-53.
102. Mezer A, Yeatman J, Stikov N, Kay K, Cho N, Dougherty R, Perry M, Parvizi J, Hua L, Butts-Pauly K, Wandell B. Quantifying the local tissue volume and composition in individual brains with magnetic resonance imaging. Nature Medicine 2013;19(12):1667-1672.
103. Wilhelm MJ, Ong HH, Wehrli SL, Li C, Tsai PH, Hackney DB, Wehrli FW. Direct magnetic resonance detection of myelin and prospects for quantitative imaging of myelin density. Proc Natl Acad Sci U S A 2012;109(24):9605-9610.
104. Guidotti G. Membrane proteins. Annu Rev Biochem 1972;41:731-752.
105. van Walderveen MA, Kamphorst W, Scheltens P, van Waesberghe JH, Ravid R, Valk J, Polman CH, Barkhof F. Histopathologic correlate of hypointense lesions on T1-weighted spin-echo MRI in multiple sclerosis. Neurology 1998;50(5):1282-1288.

106. Lucchinetti C, Brück W, Parisi J, Scheithauer B, Rodriguez M, Lassmann H. Heterogeneity of multiple sclerosis lesions: implications for the pathogenesis of demyelination. Ann Neurol 2000;47(6):707-717.
107. Bottomley PA, Foster TH, Argersinger RE, Pfeifer LM. A review of normal tissue hydrogen NMR relaxation times and relaxation mechanisms from 1-100 MHz: dependence on tissue type, NMR frequency, temperature, species, excision, and age. Med Phys 1984;11(4):425-448.
108. Fullerton GD, Potter JL, Dornbluth NC. NMR relaxation of protons in tissues and other macromolecular water solutions. Magn Reson Imaging 1982;1(4):209-226.
109. Laule C, Vavasour IM, Moore GR, Oger J, Li DK, Paty DW, MacKay AL. Water content and myelin water fraction in multiple sclerosis. A T2 relaxation study. J Neurol 2004;251(3):284-293.